AIX-MARSEILLE UNIVERSITÉ
UNIVERSIDAD SAN FRANCISCO DE QUITO
ED 352 - PHYSIQUE ET SCIENCES DE LA MATIÈRE
IM2NP - INSTITUT MATERIAUX MICROELECTRONIQUE NANOSCIENCES DE PROVENCE

Thèse présentée pour obtenir le grade universitaire de docteur

Discipline : PHYSIQUE ET SCIENCES DE LA MATIÈRE
Spécialité : MATIÈRE CONDENSÉE ET NANOSCIENCES

Silvana GUITARRA

Titre de la thèse : Modélisation multi-échelles des mémoires de type résistives

Soutenue le 10/12/2018 devant le jury :

Damien DELERUYELLE	INSA Lyon	Rapporteur
Ludovic GOUX	IMEC	Rapporteur
Alberto VERGA	Aix-Marseille Université	Examinateur
Melissa INFUSINO	Universidad San Francisco de Quito	Examinateur
Laurent RAYMOND	Aix-Marseille Université	Directeur de thèse
Lionel TROJMAN	Universidad San Francisco de Quito	Co-Directeur de thèse

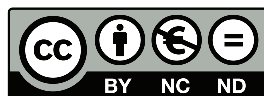

Cette oeuvre est mise à disposition selon les termes de la Licence Creative Commons Attribution - Pas d'Utilisation Commerciale - Pas de Modification 4.0 International.

Résumé

Dans ce manuscrit, un modèle de commutation de mémoires résistives (ReRAM) est présenté. Celui-ci est basé sur deux hypothèses : (1) la commutation résistive est causée par des changements qui se produisent dans la zone étroite (région active) du filament conducteur sous l'influence du champ électrique et (2) la commutation résistive est un processus stochastique, donc régi par une probabilité. La région active est représentée par un réseau de connexions verticales, chacune composée de trois éléments électriques : deux d'entre eux sont de faibles résistances faibles tandis que le troisième agit comme un disjoncteur et peut être soit de résistance faible (LR) ou élevée (HR). Dans ce modèle, le changement d'état du disjoncteur est régi par une probabilité de commutation (P_s) qui est comparée à un nombre aléatoire « p ». P_s dépend de la chute de tension le long du disjoncteur et de la tension de seuil, V_{set} ou V_{reset}, pour définir les processus de « set » (HR à LR) et « reset » (LR à HR). Deux mécanismes de conduction ont été envisagés : ohmique pour un état LR et pour un état de résistance élevée l'effet tunnel facilité par un piège, aussi connu comme « Trap Assisted Tunneling (TAT) » . Le modèle a été implémenté avec le langage de programmation Python et fonctionne avec une bibliothèque C externe qui optimise les calculs et le temps de traitement. Les résultats de la simulation ont été validés avec succès en les comparant avec des courbes courant-tension (IV) mesurées sur dispositifs ReRAM réels dont l'oxyde était fait de HfO_2 et pour neuf aires différentes. Il est important de noter que la flexibilité et la facilité de mise en œuvre de ce modèle de commutation résistive en font un outil puissant pour la conception et l'étude des ReRAM.

Mots clés : mémoires résistives (ReRAM), commutation résistive, caractérisation électrique, set, reset, conduction ohmique, conduction à effet tunnel assisté par piège, TAT, HRS, LRS, probabilité de commutation.

Abstract

A model for the switching of resistive random-access memories (ReRAM) is presented. This model is based on two hypotheses: (1) the resistive switching is caused by changes that occur in the narrow zone (active region) of the conductive filament under the influence of the electric field and (2) the resistive switching is a stochastic process governed by a switching probability. The active region is represented by a net of vertical connections, each one composed of three electrical elements: two of them are always low resistive (LR) while the third one acts as a breaker and can be low or high resistive (HR). In the model, the change of the breaker's state is governed by a switching probability (P_s) that is compared with a random number p. P_s depend on the voltage drop along the breaker and the threshold voltage, V_{set} or V_{reset} for set (HR to LR) or reset (LR to HR) processes. Two conduction mechanism has been proposed: ohmic for the low resistive state and trap-assisted tunneling (TAT) for the high resistive state. The model has been implemented in Python and works with an external C-library that optimizes calculations and processing time. The simulation results have been successfully validated by comparing measured and modeled IV curves of HfO_2-based ReRAM devices of nine different areas. It is important to note that the flexibility and easy implementation of this resistive switching model allow it to be a powerful tool for the design and study of ReRAM memories.

Keywords: Resistive Random Access memories (ReRAM), resistive switching, electrical characterization, set process, reset process, ohmic conduction, trap assisted tunneling conduction, TAT, HRS, LRS, switching probability.

Acknowledgements

Without the support and constant encouragement from many people, this project would not have been possible.

First, I would like to express my deepest gratitude to my tutors, Laurent Raymond and Lionel Trojman, for his invaluable guidance and insightful direction throughout the course of my work. Despite the distance and the conditions, the things that I have learned from you, personally and professionally, are innumerable.

I would like to thank to the USFQ for giving me this opportunity and for providing the financial support that permitted me to do my thesis. Thanks to all the members of this community, my dear friends, my colleagues and my students. Specially, I would like to express my gratitude to Andrea for her friendship, support and patient throughout these years.

My sincere thanks goes to my parents, Anita y Fidel, because they have been the source of motivation during all my life. I will never be able to repay all your sacrifices and help. Thanks for always being there for me during the good and the bad. Thanks for supporting and encouraging me to do my best.

Also, I would like to thank my parents in law, Marianita y Fausto, for their generous support on my family, especially when I was out of my country.

I've also had an amazing group of friends who have been with me through this entire process : Gise, Anita, Gaby, Xavy, Freddy, and Lenin. Thank you for listening, offering me advice, and supporting me over this thesis journey.

Last and more important, my heartfelt gratitude goes to my husband, David, and my kids, Sebastián and Isabela, for encouraged me to pursue this degree. A ginormous acknowledgment to David for your patience and unending support, and to my kids because they always brought a smile to my face after the long days. Thank you for your unconditional love.

Summary

Les mémoires à accès aléatoire de type résistive (ReRAM) pourraient faire partie de la prochaine génération de technologies de mémoire non volatile, et en particulier pour remplacer les mémoires flash qui, aujourd'hui, se trouvent confrontées à leur limite physique en raison de la réduction des dimensions requise des appareils électroniques. ReRAM mémoires a été étudié au cours des dernières années en raison de ses caractéristiques prometteuses : haute densité, haute endurance, haute vitesse, fonctionnement à basse tension et, en particulier, sa compatibilité avec les processus industriels CMOS.

La ReRAM est un dispositif capacitif de type MIM (Métal-Isolant-Métal) dont la couche centrale peut basculer ou commuter d'un état hautement résistif a un état faiblement résistif (cf. Fig. 0.5a). L'état de haute résistance (HRS) et l'état de faible résistance (LRS), représentent les valeurs logiques 1 et 0 que peut stocker une mémoire. La transition de HRS à LRS est appelée «SET », alors que la transition de LRS à HRS est appelée « RESET » (cf. Fig. 0.5b).

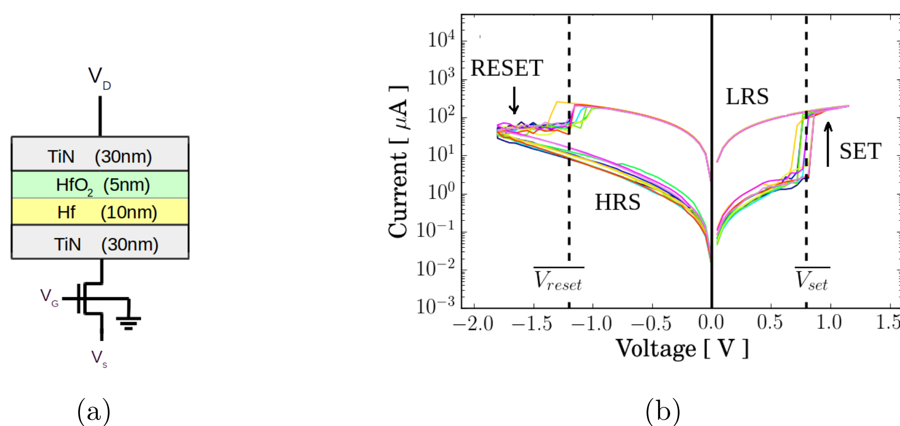

(a) (b)

FIGURE 0.1. – (a) Schéma d'une architecture "1T1R" intégrant la mémoire ReRAM à base d'oxyde d'hafnium. (b) Caractéristiques courant-tension de la ReRAM.

Dans cette étude, nous travaillons avec des ReRAM de type bipolaire, c'est-à-dire qu'il faut appliquer un champ électrique de polarité opposée pour produire une commutation de l'état HRS à LRS y de l'état LRS à HRS.

En pratique, l'étude des ReRAM nécessite des techniques pour analyser et comprendre ses mécanismes de commutation résistif. Ces techniques (caractérisation physique) se basent sur la détermination de la microstructure, la composition et

l'état chimique de l'isolant et des électrodes. Cependant, cette approche peut se révéler très coûteuse et peu pratique pour l'industrie. Par ailleurs une approche physique nécessite aussi l'implication d'un modèle que les ingénieurs peuvent utiliser (modèle compact) pour définir la meilleure technologie à utiliser pour développer des ReRAM à l'échelle industrielle. Bien que certains modèles aient été proposés pour expliquer la commutation résistive dans les mémoires ReRAM, il subsiste une question non résolue concernant la transition de l'état et les mécanismes de conduction. De plus il existe que peu voire pas du tout de modèle proposant une approche simple et universelle sur ces questions ; i.e. indépendante de la technologie et des matériaux utilisés.

Ces antécédents nous ont motivé à proposer un modèle physique pour comprendre et prédire la commutation résistive des dispositifs ReRAM bipolaires. Pour ce faire, nous avons d'abord étudié la réponse électrique courant-tension (IV) des mémoires ReRAM à base d'HfO_2, et puis nous avons proposé un modèle pour reproduire sa commutation résistive.

Parmi tous les matériaux isolants possibles, nous avons utilisé l'oxyde d'hafnium (HfO_2). Le HfO_2 est un des oxydes de métal les plus étudiés dans l'industrie des semi-conducteurs. Il est largement admis que les ReRAM à base d'HfO_2 ont une conduction filamentaire. Par conséquent ils nécessitent un processus d'activation, appelé électroformage, dans lequel la migration des lacunes d'oxygènes crée un filament conducteur (CF) entre les électrodes qui permettent la conduction électrique. Les processus de RESET et SET sont dus respectivement à la rupture locale et à la reformation du CF entraînée par le champ électrique.

D'abord, une analyse complète de la réponse électrique des dispositifs a été effectuée afin de déterminer les paramètres électriques qui décrivent le processus de commutation. La structure des ReRAM que nous étudions ici correspond à l'empilement de couches de matériaux suivant : TiN(30nm)/ HfO_2(5nm)/ Hf(10nm)/ TiN(30nm) (Fig. 0.5a). Ces dispositifs ont neuf aires différentes : 55x55 nm^2, 65x65 nm^2, 75x75 nm^2, 85x85 nm^2, 105x105 nm^2, 135x135 nm^2, 1x1 um^2, 3x3 um^2 et 5x5 nm^2. Les six premiers ont été dénommés « échantillons de taille nm » tandis que les autres « échantillons de taille μm ». La nécessité de limiter le courant durant le mesures électriques induit souvent l'intégration conjointe d'un transistor (cf. Fig. 0.5a)). Cette architecture est nommée "1T1R".

Pour décrire la caractéristique courant-tension observées lors de la commutation, nous avons déterminé cinq paramètres électriques : deux d'entre eux sont les potentiels de transition, V_{set} et V_{reset}, tandis que les trois autres caractérisent les mécanismes de conduction électrique.

Tout d'abord, le V_{reset} correspond au basculement du dispositif depuis l'état de LRS vers l'état de HRS. Cette tension est relevée lorsque le courant de reset (I_{reset}) atteint son maximum. Ensuite, le V_{set} correspond à la commutation du dispositif de l'état de HRS à l'état de LRS. Cette tension est relevée lorsque le courant dans le dispositif augmente de façon abrupte (cf. Fig. 0.5b).

Selon le caractéristique courant-tension, deux mécanismes de conduction prin-

cipaux ont été proposés : la conduction ohmique en LRS et l'effet tunnel de type TAT en HRS. Lorsque le système est en LRS, la relation linéaire entre courant et tension, donnée par $I = GV$, permet de trouver la valeur de conductance, G. Par contre, lorsque le système est en HRS, la dépendance exponentielle de courant-tension a été analysée comme suit : $I = I_o \sinh(\alpha V)$, où I_o et α sont des paramètres électriques d'ajustement. Le sinus hyperbolique (sinh) permet de décrire la réponse du système sous des potentiels négatifs et positifs, comme cela se produit avec la réponse électrique réelle.

Ces paramètres : V_{set}, V_{reset}, G, I_o et α, , permettent de décrire la commutation résistive et ils peuvent être obtenus à partir de la caractérisation électrique IV.

Pour évaluer l'effet du courant d'auto adaptation ou « Current Compliance » (I_c) sur la réponse courant-tension (IV), nous avons choisi deux valeurs : I_c = 5mA et I_c = 10mA. Les résultats montrent que la tension de formation (V_{form}) requise pour l'activation (electroformage) de la ReRAM est presque indépendante de I_c. Cependant, V_{form} présente une tendance à la hausse dans les petits échantillons quelle que soit la valeur I_c. En ce qui concerne l'effet du courant de compliance sur la réponse IV lors de la commutation résistive (après électroformage), aucune différence significative n'a été constatée.

Après la formation du filament conducteur, nous avons étudié la distribution statistique des paramètres de commutation. Il est important de noter que la commutation résistive se produit par le mouvement stochastique des lacunes d'oxygènes, sous l'influence d'un champ électrique. En conséquence, sa caractérisation précise devrait être effectuée par une analyse statistique. Pour évaluer le comportement de V_{set}, V_{reset}, G, I_o et α au cours des cycles, ces informations ont été présentées par le biais d'histogrammes, valeurs moyennes et valeurs d'écart-type. De plus, le test de normalité a été appliqué à tous les ensembles de données pour prouver qu'ils peuvent être bien représentés par une distribution gaussienne.

Nous avons identifié que V_{set} suit une distribution gaussienne pour tous les échantillons avec une valeur moyenne similaire dans le même groupe d'échantillons : V_{set} = 0,673 $\pm$ 0,046V pour les échantillons de taille nm et V_{set} = 0,480 $\pm$ 0,007 pour les échantillons de taille μm. D'autre part, V_{reset} a une valeur moyenne similaire pour tous les échantillons, V_{reset} = -1,117 $\pm$ 0,126, mais il suit une distribution gaussienne uniquement chez ceux avec une taille en nm. Avec ce résultat, on pourrait supposer que le processus de reset est davantage affecté par la nature stochastique du mouvement et de la recombinaison des lacunes en oxygène dans la couche d'HfO_2.

En ce qui concerne le mécanisme de conduction, dans l'état de LRS, la conduction est ohmique car les lacunes en oxygène sont suffisamment proches pour créer le FC. La valeur de la conductance(G) nous permet d'évaluer comment le courant électrique circule dans l'isolant dans ces conditions. Après l'ajustement avec une équation linéaire, deux tendances claires ont été déterminées, une pour les échantillons de taille en nm, G = 176 μS et l'autre pour les échantillons de taille en μm, G = 960 μS. Lorsque le système est en HRS, le FC est partiellement

détruit dans sa régin la plus étroite en raison de la recombinaison entre les lacunes d'O_2 dans l'HfO_2 et les ions oxygène. Dans ce cas, les site vacants restants sont situés au hasard et ils se comporteraient comme des pièges permettant une conduction par effet tunnel. Les valeurs de I_o et α, utilisées pour décrire ce phénomène de conduction, sont fortement liées pour tous les échantillons. En outre, ces paramètres présentent une grande dispersion de valeurs et ont également une relation avec l'aire du dispositif (A). Nous avons aussi constaté que α a une relation linéaire avec A, tandis que I_o a une relation potentielle.

Ces sur la base de ces résultats obtenus par caractérisation électrique du dispositif que nous avons été amené à proposer un modèle de commutation résistive sur ReRAM bipolaire. Ce modèle repose sur deux hypothèses : (1) la commutation résistive est provoquée par le champ électrique qui affecte principalement la région étroite du CF et (2) la commutation résistive est un processus stochastique régi par une probabilité de commutation.

Dans ce modèle nous décrivons le CF comme un circuit électrique (cf. Fig 0.2). La région la plus étroite du CF, appelée région active, est représentée par une combinaison de chaînes verticales (N_x), chacune composée de trois éléments électriques. Deux d'entre eux sont des résistances de faible valeurs (LR), tandis que le troisième agit comme un disjoncteur et peut être à résistance faible ou élevée (HR).

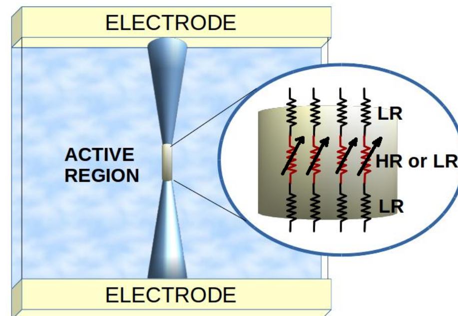

FIGURE 0.2. – Schéma du filament conducteur décrit comme un circuit électrique.

Le changement d'état du disjoncteur est régi par une probabilité de commutation (P_s) qui, dans le modèle, est comparée à un nombre aléatoire p. Cette probabilité est calculée par la formule suivante :

$$P_S = \frac{1}{2}\left\{1 + \tanh\left[C_s\left(V_{link} - V_{ref}\right)\right]\right\} \tag{0.1}$$

qui dépend de la tension passant par la liaison (V_{link}) et de la tension de seuil (V_{ref}) qui correspond à V_{set} ou V_{reset}, pour les processus de set ou reset.

Pour calibrer la fonction de probabilité de commutation, la valeur de la pente de cette fonction (C_s) est requise. Après l'analyse statistique de V_{set} et V_{reset},

nous avons réalisé que la fonction de distribution cumulative de ces données correspond à la forme de notre probabilité de commutation proposée lorsque C_s est l'inverse de l'écart standard. En conséquence, la probabilité de commutation a été calibrée par la variabilité observée dans les données expérimentales. En d'autres termes, pour le processus de set la pente sera positive et ouverte à droite, et pour le reset, il sera négatif et ouvert à gauche.

Dans le modèle, pour chaque tension appliquée (V_{ext}), la valeur de V_{link} et le courant I sont calculés en résolvant les équations de Kirchhoff à chaque noeud. Ces equation doivent être réécrits en fonction de l'état du disjoncteur. Cela signifie que le courant au noeud est une combinaison de conduction ohmique et TAT si le disjoncteur est en HRS (eq. 0.2), alors que c'est une somme de deux contributions de conduction ohmique si le disjoncteur est LR (eq. 0.3).

$$I_i = \sigma_{im}(V_i - V_m) + I_0 \sinh(\alpha(V_i - V_j))) \tag{0.2}$$

$$I_i = \sigma_{im}(V_i - V_m) + \sigma_{ij}(V_i - V_j) \tag{0.3}$$

Dans le modèle de plusieurs chaines en parallèle, les équations de Kirchhoff donnent un système d'équations non linéaire qui est résolu par la méthode de Newton-Raphson.

Dans la simulation, pour le processus de set, les disjoncteurs sont initialement en HRS quand tension externe (V_{ext}) est appliquée. Ensuite, le courant (I) et les tensions à chaque noeud sont calculés. Si le courant est inférieur à I_c, la tension à travers le disjoncteur (V_{link}) est calculée. Ensuite, la probabilité de set (P_{set}) est calculée et le nombre aléatoire (p) est généré. Seulement si P_{set} est plus grand que p, l'état du disjoncteur passe à l'état LR. Sinon, la valeur V_{ext} est augmentée et le processus est répété. Le mémoire ReRAM passe à l'état LRS quand tous les disjoncteurs sont LR. Le diagramme de flux pour le processus de set est présenté dans la figure suivante :

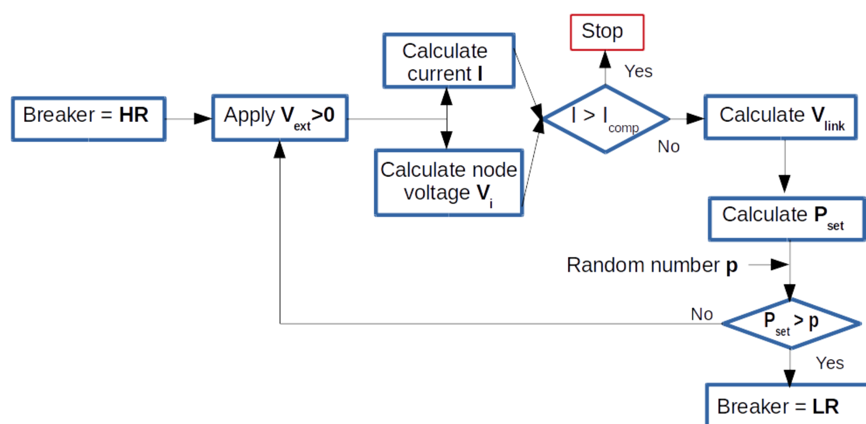

FIGURE 0.3. – Diagramme de flux pour le processus de set

Pour le processus de reset, les disjoncteurs sont dans l'état LR, la tension néga-

tive est appliquée et le processus est similaire à celui déjà expliqué.

Le modèle a été implémenté en Python et fonctionne avec une bibliothèque C externe qui optimise les calculs et le temps de traitement. Les résultats de la simulation ont été validés avec succès en comparant les caractéristiques courant tension mesurées et modélisées dans tous les appareils (cf. Fig. 0.4).

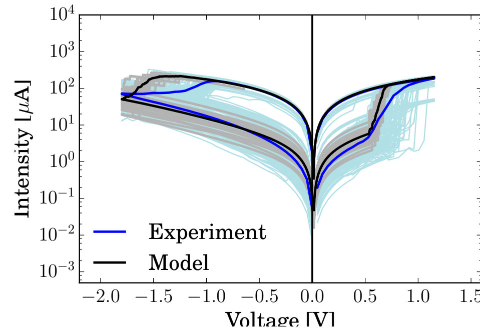

FIGURE 0.4. – Caractéristiques électriques et simulations de ReRAM à base d'oxyde d'hafnium

En outre, dans un deuxième temps, la présence d'une résistance en série a également été incluse dans le modèle pour prendre en compte les effet parasite de la ReRAM réelle. La Figure 0.5 présente le modèle et le résultats des simulations pour un dispositif.

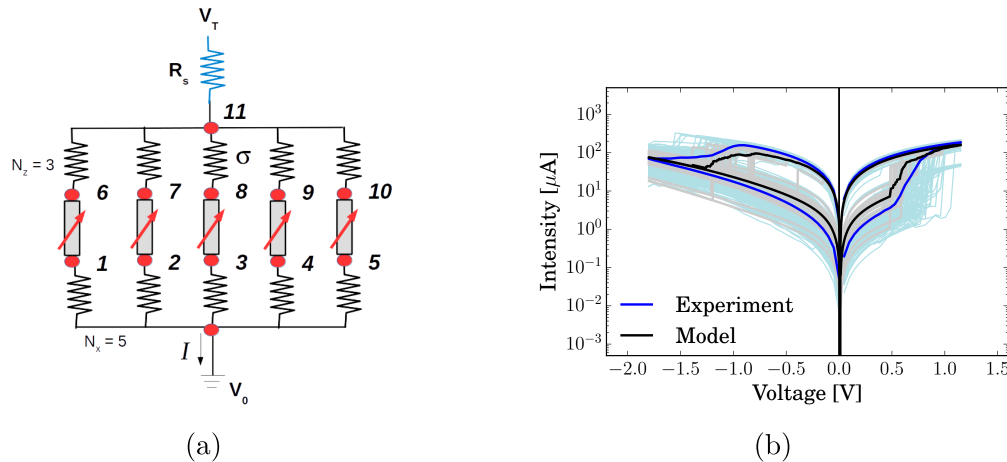

FIGURE 0.5. – Caractéristiques électriques et simulations avec le 1T1R model pour la ReRAM à base d'oxyde d'hafnium

Certains avantages peuvent être mentionnés à propos de ce modèle. Premièrement, ce modèle est basé sur quelques équations corrélées au comportement expérimental des ReRAM. Deuxièmement, il est efficace et rapide car, contrairement à d'autres modèles, il est axé sur une petite partie des FC, et, troisièmement, il tient compte de la nature stochastique de la commutation résistive.

Ce modèle pourrait être appliquer à d'autres dispositifs ReRAM bipolaires. En effet une fois obtenue les données expérimentales, on pourrait trouver les valeurs appropriées des paramètres en suivant la méthode statistique proposée dans ce travail. En outre, ce modèle pourrait être adapté pour inclure d'autres types de mécanismes de conduction (notament en HRS) en fonction de la technologie et des matériaux, mais aussi des conditions d'opération d'un dispositif ReRAM bien spécifique. Il est important de noter que la flexibilité et la facilité de mise en œuvre de ce modèle de commutation résistive en font un outil puissant pour la conception et l'optimisation des ReRAM.

Table des matières

Résumé 3

Abstract 4

Remerciements 5

Summary 12

Table des matières 13

Table des figures 15

Liste des tableaux 20

Nomenclature 21

Introduction 25

1 Fundamentals of resistive random access memories 26

1.1 Overview of memory technologies 26
1.2 From resistive change materials to ReRAM 30
1.3 ReRAM operation 31
1.3.1 Activation step : electroforming process 31
1.3.2 Switching modes 32
1.3.3 Conduction mechanism of ReRAM 34
1.3.4 Preliminary studies of HfO_2-based ReRAM 37

2 HfO_2-based ReRAM fabrication, activation and electrical characterization 39

2.1 Device fabrication 39
2.2 Device structure 40
2.3 Electrical characterization 41
2.4 Electroforming : cell activation 42
2.5 Electrical characterization of HfO_2-based ReRAM 46
2.5.1 Set and reset voltage study 47
2.5.2 ON/OFF ratio 53
2.5.3 Analysis of the conduction mechanism 54

2.5.4 Different electrical response of the samples electroformed with I_c=5mA and I_c=10mA . . . 64
2.6 Stochastic Nature of ReRAM . . . 66

3 Phenomenological model for resistive switching of bipolar ReRAM devices 68
3.1 One-Chain model . . . 69
3.1.1 Switching probability . . . 70
3.1.2 Set and reset switching simulation . . . 71
3.2 N-Chain model . . . 73
3.3 Conduction mechanisms in the model . . . 74
3.4 Model implementation . . . 75
3.5 Model calibration . . . 79
3.6 Simulation results and discussion . . . 81

4 A model for 1T1R measurement configuration 84
4.1 Intrinsic IV switching characteristics . . . 85
4.2 Intrinsic resistive switching parameters . . . 87
4.2.1 Number of conduction channels in LRS . . . 88
4.3 Model for the resistive switching of 1T1R ReRAM cell structure . . . 89

Conclusion 95

Bibliographie 96

Index 115

Notes 117

ANNEXES 118
A Articles . . . 118
B Fabrication techniques used in HfO_2-based ReRAM's . . . 119
B.1 Atomic layer deposition (ALD) . . . 119
B.2 Physical vapor deposition (PVD) . . . 119
B.3 Chemical vapor deposition (CVD) . . . 120
B.4 Lithography and dry etch . . . 121
B.5 Chemical mechanical planarization (CMP) . . . 122
B.6 Passivation process . . . 123
C Normality test for electrical parameters . . . 124
D Models for resistive switching in ReRAM devices . . . 126
D.1 Quantum Point-Contact model . . . 128

Table des figures

0.1 (a) Schéma d'une architecture "1T1R" intégrant la mémoire ReRAM à base d'oxyde d'hafnium. (b) Caractéristiques courant-tension de la ReRAM. 6
0.2 Schéma du filament conducteur décrit comme un circuit électrique. 9
0.3 Diagramme de flux pour le processus de set 10
0.4 Caractéristiques électriques et simulations de ReRAM à base d'oxyde d'hafnium 11
0.5 Caractéristiques électriques et simulations avec le 1T1R model pour la ReRAM à base d'oxyde d'hafnium 11

1.1 Basic scheme of a flash memory cell. It consists of one metal-oxide-semiconductor with an additional floating gate. The logic state is 0 when electrons are presented in the floating gate, otherwise the state is 1 [18]. 27
1.2 (a) Schema of a typical ferroelectric random access memory (FRAM) cell [23]. (b) Schema of a phase change random access memory (PCRAM) cell (c) Schema of a magnetoresistive random access memory (MRAM) structure. 28
1.3 (a) Schematic diagram metal-insulator-metal structure (MIM) of ReRAM. (b) Diagram of a cross-point memory architecture where word and bit lines allow to select a memory cell for writing and reading data [24] 29
1.4 Proposed models for resistive switching can be classified according to either (a) a filamentary conducting path, or (b) an interface-type conducting path [66]. 31
1.5 Typical unipolar-type resistive switching I–V characteristics of a metal-binary oxide-metal device 33
1.6 Typical bipolar-type resistive switching I–V characteristics of a metal-binary oxide-metal device 33
1.7 Schematic energy band diagram of interface-type conduction mechanisms : Schottky emission, Fowler-Nordheim tunneling and direct tunneling [87] 35
1.8 Schematic of trap assisted tunneling conduction mechanisms : Poole-Frenkel emission, tunneling from cathode to traps, tunneling from traps to anode, and trap to trap tunneling. 36

2.1 (a) HfO_2-based integrated 1T1R ReRAM devices structure, consisting of Ti/HfO_2/Hf/TiN stacks. (b) IMEC's device fabrication process flow. 40
2.2 Electrical characterization process of HfO_2-based ReRAM devices. . 41
2.3 Electrical characterization of the ReRAM device on a wafer probe station 42
2.4 Current-voltage characteristics of the HfO_2-based ReRAM devices of nm^2-cell area during electroforming at a positive applied bias with I_c=5mA in black and I_c=10mA in blue. 43
2.5 Current-voltage characteristics of the HfO_2-based ReRAM devices of μm^2-cell area during electroforming at a positive applied bias with I_c=5mA in black and I_c=10mA in blue. 44
2.6 Area scaling trends for (a) forming voltage (V_{form}) and (b) forming forming current (I_{form}). One can compare the effect of I_c in these values during electroforming. 45
2.7 Forming conductance as a function of the device-area 45
2.8 Current–voltage characteristics of HfO_2-based ReRAM devices of nm^2-cell area, during one experiment of ten cycles. The devices show bipolar resistive switching behavior. 47
2.9 Current–voltage characteristics of HfO_2-based ReRAM devices of μm^2-cell area, during one experiment of ten cycles. The devices show bipolar resistive switching behavior. 48
2.10 Current–voltage characteristics during set and reset process of the HfO_2-based ReRAM of 85x85nm^2. One can identify the cycle to cycle variability. As example, two cycles in color are presented. . . . 49
2.11 Distribution of V_{set} and V_{reset} values, obtained from experimental data, for two samples, 65x65nm^2 (green dots) and 5x5μm^2 (blue dots) 49
2.12 Statistical distribution of set voltage (V_{set}) of HfO_2-based ReRAM devices. 50
2.13 Statistical distribution of reset voltage (V_{reset}) of HfO_2-based ReRAM devices. 51
2.14 V_{set} and V_{reset} as a function of the area of HfO_2-based ReRAM devices. 52
2.15 IV response for a ReRAM device. At a critical voltage (V_{set}), the current abruptly increases. The relationship between currents gives the ON/OFF ratio 53
2.16 On/off ratio for set (blue) and reset (red) regions. 53
2.17 Conductance-voltage curve for the HfO_2-based ReRAM device of 55x55nm^2. 54
2.18 Conductance-voltage curve for the HfO_2-based ReRAM device of 1x1μm^2. 54
2.19 Comparison of the I-V curves during set and reset processes for the HfO_2-based ReRAM device of (a) 55x55nm^2 and (b) 3x3μm^2. . . . 55

2.20 Fitting of I-V curves by a function of the form $I = GV$ to obtain the value of the conductance G. The fitting is done in the region where the system is in low resistive state and follows ohmic conduction. . 56
2.21 Conductance for set and reset process as a function of area device. . 57
2.22 Fitting of I-V curves under negative voltages by a function of the form $I = I_0 \sinh[\alpha(\Delta V)]$ to obtain I_0 and α. The fitting is done in the region where the system is in high resistive state and has tunneling conduction. 58
2.23 Statistical distribution of I_o 59
2.24 Statistical distribution of α 60
2.25 I_o and α as a function of area device 61
2.26 Relative standard deviation (RDS) as a function of the area for I_o and α 61
2.27 Relationship between I_o and α through 2D histograms. 62
2.28 I_o as a function of α for nm-size samples. 63
2.29 Current-voltage characteristics of HfO_2-based ReRAM devices electroformed with two values of compliance current, I_c=5mA in black and I_c=10mA in blue. 64
2.30 V_{set} and V_{reset} as a function of the device area for samples electroformed with I_c=5mA in black and I_c=10mA in blue. 65
2.31 Conductance G, used to describe ohmic conduction in LRS, as a function of the device area for samples electroformed with I_c=5mA in black and I_c=10mA in blue. 65
2.32 I_o and α, used to describe TAT conduction in HRS, as a function of the device area for samples electroformed with I_c=5mA in black and I_c=10mA in blue. 66

3.1 Model 69
3.2 Switching probability P_s of set and reset processes. 71
3.3 Flowchart for set and reset processes used in computer simulation. . 72
3.4 (a) Simulation result of a bipolar ReRAM-device modeled with an active region composed of one vertical chain and (b) Experimental I-V response of a bipolar HfO_2-based ReRAM of 85x85nm^2. 72
3.5 I-V characteristics of the HfO_2-based ReRAM of 85x85nm^2 where some jumps in set and reset switching can be identified. 73
3.6 Scheme of the active region composed by four chains, each one with of three elements with low resistance (LR) or high resistance (HR) . 73
3.7 I-V simulation results of 5 cycles of a bipolar ReRAM device modeled with an active region composed of four vertical chains 74
3.8 I-V experimental data. Linear relationship in LRS shows an ohmic conduction while the exponential dependency in HRS implies a tunneling mechanism. 75
3.9 Scheme of the active region composed by five chains 76

3.10 Section of the Python script used for resistive switching simulation. 77
3.11 I_o and α as a function of the area for HfO_2-based ReRAM of nm-size, along with the fitting used to calibrate the model. 80
3.12 Cumulative distribution of set voltage (V_{set}) along with the probability function. 81
3.13 Relationship between active region of the model and the sub-stoichiometric region the $TiN/HfO_2/Hf/TiN$ ReRAM devices. . . . 81
3.14 Model and experimental current–voltage response of HfO_2ReRAM devices. Grey lines correspond to the model and light blue lines correspond to experimetal curves. 82

4.1 1T1R test structures during forming, set and reset electrical characterization of HfO_2-based ReRAM. 84
4.2 IV characteristic of the HfO_2-based ReRAM with area 135x135nm^2, where one can observe the linear relationship related to series resistance generated by the transistor. 85
4.3 Experimental IV curves (black) and the intrinsic electrical response for the HfO_2-based ReRAM (red). 86
4.4 Instrinsic V_{set} and V_{reset} as a function of the area. 87
4.5 Instrinsic I_o and α as a function of the area. 88
4.6 Distribution of the number of active channels in LRS 89
4.7 5 chain model with a series resistance R_s 90
4.8 Model and experimental current–voltage response of HfO_2ReRAM devices. Grey lines correspond to the model and light blue lines correspond to experimetal curves. 91

.1 Schematic of the Atomic Layer Deposition (ALD) process. (a) Substrate surface is prepared (b) Precursor A is pulse and reacts with surface (c) Excess precursors and reactions are purged with inert gas (d) Counter-reactant (H_2O) precursor is applied and reacts with surface (e) Second purge (f) The process is repeated until the desired material thickness is achieved [142] 120
.2 Schematic of the Physical Vapor Deposition (PVD) process[148] . . 120
.3 Schematic of the Chemical Vapor Deposition (CVD) 121
.4 Schematic of lithography and etch 121
.5 The plasma hits the silicon wafer with high energy to knock-off the Si atoms on the surface. (a) The plasma atoms hitting the surface (b) The silicon atoms being evaporated off from the surface [152] . . 122
.6 A schematic of CMP process [155] 122
.7 The schematic of the ReRAM cell with a narrow zone inside the conductive filament (CF) considered as a quantum point contact (QPC). 128

.8 Schematic representation of the energy barrier profile along the constriction where V is the applied external voltage, I is the filament current, R is an external series resistance, E_F is the Fermi level, Φ is the potential height in relation to Fermi level, t_B is the potential thickness at E_F and e is the elementary electron charge. For the HRS, the potential barrier is above the energy window and for LRS, is below. The shaded region is the energy window for the injected electrons [48]. 129

Liste des tableaux

1.1 Comparison between the properties of non-volatile memory devices (2017) [3] . . . 30
1.2 Expressions for interface-type conduction mechanisms . . . 35
1.3 Expressions for bulk-type conduction mechanisms . . . 37

2.1 Forming voltage (V_{form}) and current (I_{form}) for HfO_2-based ReRAM devices of nm^2-cell area and μm^2-cell area. . . . 46
2.2 Conductance for set and reset processes . . . 56
2.3 Mean value and standard deviation of I_o and α determined by the fitting of IV curves when the system is in HRS with the function $I = I_0 \sinh[\alpha(V)]$ . . . 61

3.1 Kirchhoff's equations for the 5-chain model (Fig. 3.9) when all breakers are HR. . . . 78
3.2 Parameters used to calibrate the model. . . . 80

4.1 Intrinsic conductance . . . 87
4.2 Kirchhoff's equations for an active region of five vertical chains with an access series resistance R_s. . . . 90

.1 Normality test results for V_{set} [V] . . . 124
.2 Normality test results for V_{reset} [V] . . . 125
.3 Normality test results for I_o [A] . . . 125
.4 Normality test results for α [1/V] . . . 125
.5 Published works with Monte Carlo simulation in HfO_2-based ReRAM 126
.6 Macroscopic models for simulation in HfO_2-based ReRAM . . . 127
.7 Compact models simulation in HfO_2-based ReRAM . . . 127

Nomenclature

1T1R
One-transistor and one-resistor. 40

CBRAM
Conductive Bridge Random Access Memory. 30

CF
Conductive filament. 30, 33, 37, 52, 127

CMOS
Complementary metal-oxide-semiconductor. 27, 29

DFT
Density Functional Theory. 126

DRAM
Dinamic Random Access Memory. 26

DT
Direct Tunneling. 34

ECM
Electrochemical metallization. 30

FeRAM
Ferroelectric Random Access Memory. 27

F-N
Fowler Nordheim tunneling. 34, 35

HDB
Hard Dielectric Breakdown. 31

HRS
High resistive state. 29, 32, 33, 41

I_c
Compliance current. 31, 33, 41

IMEC
Inter University Micro Electronics Centre. 39

LRS
Low resistive state. 29, 32, 33, 41

MC
Monte Carlo. 126

MD
Molecular dynamics. 126

MIM
Metal-insulator-metal. 15, 28–31, 40

MJT
Magnetic Tunnel Junction. 28

MOS
Metal-oxide semiconductor. 27

MOSFET
Metal-oxide Semiconductor Field Effect Transistor. 29, 41

MRAM
Magnetoresistive Random Access Memory. 27, 28

NVM
Non-volatile memory. 26

PCRAM
Phase change Random Access Memory. 27, 28

QPC
Quantum point contact. 38

RAM
Random Access Memories. 26

RCB
Random Circuit Breaker. 127

ReRAM
Resistive Random Access Memories. 26–28

RS
Resistance Switching. 53

SDB
Soft Dielectric Breakdown. 31

SRAM
Static Random Access Memory. 26

TAT
Trap Assisted Tunneling. 46, 71

TCM
Thermochemical Memory. 30

TE
Top electrode. 41

TMO
Transition Metal Oxides. 30

V_{form}
Forming Voltage. 31

V_{reset}
Reset voltage. 33, 46

V_{set}
Set voltage. 33, 46

VCM
Valence Change Memory. 30

VM
Volatile memory. 26

Introduction

Smart phones, tablets, computers, and solid-state disks are some examples of the accelerated advances of technology. However, the large amount of information generated by the different tasks that they can do needs to be stored, and consequently, these devices require non-volatile memories (NVM) to do it. The most common NVM option is the flash memory that nowadays is facing its physical limit due to the scalability of the electronic devices. However, there are some emerging NVM technologies to replace flash. The most promising option is the group of non-charge-based memories that includes magnetic random-access memory (MRAM), ferroelectric random-access memory (FeRAM), phase-change memory (PCM) and resistive random-access memory (ReRAM) [1].

This study is focused on ReRAM memories. They have been extensively investigated during the last years due to their promising characteristics : high density, high speed, low cost, low voltage operation [2] and its compatibility with CMOS technology and manufacturing process [3, 4]. Further, ReRAM is also being studied for the use in neuromorphic systems [5–7].

ReRAM devices have a simple metal-insulator-metal (MIM) structure. Its memory concept is based on the resistive switching of the insulator layer by applying an external voltage. The insulator can change between two states : high resistive state (HRS) and low resistive state (LRS). These two state variables correspond to the logical 1 and 0. Nowadays, the most studied cells are those based on binary metal-oxides, particularly TiO_x [8], TaO_x [9], HfO_x [10]. Our work is focused on HfO_2-based ReRAM devices.

Many research projects have been developed around ReRAM technology. The experimental techniques used for determining the microstructure, composition and chemical state during resistive switching have limitations and the experimental results are often not so clear. These problems get worse with the scalability of the devices. On the other hand, some models have been proposed in the literature to understand and predict ReRAM behavior. They have different degrees of accuracy, different features and mixed results [11]. Regarding to models proposed for HfO_2-based systems, one can mention the Stanford Model [12], the Compact Model proposed by Huang [13], the model for resistive switching by voltage-driven ion migration [14], among others.

In this work, we propose a physics-based model to understand and predict the resistive switching of bipolar ReRAM cells. First, we analyze the electrical response of HfO_2-based devices of different areas, and after, we build a model for the resistive switching of ReRAM.

This manuscript is organized as follow :

1. In chapter 1, concepts related to the operation principles of ReRAM are discussed. The types of resistive switching (filamentary-type or interface-type), the operation modes (unipolar, bipolar or nonpolar), the electroforming process and the conduction mechanism of ReRAM are explained. Previous studies of HfO_2-based ReRAM devices are also introduced.
2. In chapter 2, the electrical behavior of HfO_2-based ReRAM devices of nine different areas (nm^2 and μm^2 range) is analyzed. We define five parameters to describe the resistive switching that can be extracted from experimental data.
3. In chapter 3, a model to reproduce resistive switching of HfO_2-based ReRAM is presented. This model works with a circuit representation of the conductive filament (CF) and it is based on two hypotheses : (1) the resistive switching is caused by the electric field that affects the thinnest zone of the CF, and (2) the resistive switching is a stochastic process that can be represented by a switching probability.
4. In chapter 4, a new novel model that considers the electrical response of the measurement element (1T) is proposed. We consider that the current, controlled by the transistor, is limited by an external parasitic effect that can be represented by a series resistance R_s. First, the intrinsic response of the devices is extracted from experimental IV curves and, after, the model proposed in chapter 3 is modified to include this R_s.

1. Fundamentals of resistive random access memories

Summary

1.1 Overview of memory technologies 26
1.2 From resistive change materials to ReRAM 30
1.3 ReRAM operation 31
1.3.1 Activation step : electroforming process 31
1.3.2 Switching modes 32
1.3.2.1 Unipolar switching 32
1.3.2.2 Bipolar switching 33
1.3.2.3 Nonpolar switching 34
1.3.3 Conduction mechanism of ReRAM 34
1.3.3.1 Interface-type conduction mechanism 34
1.3.3.2 Bulk-type conduction mechanism 36
1.3.4 Preliminary studies of HfO_2-based ReRAM 37

1.1. Overview of memory technologies

It is necessary to provide an overview of memory technologies to understand the advantages of ReRAM devices. In general, memories can be categorized into two types : volatile and nonvolatile. In volatile memories (VM), the information is lost when the power is turned off, whereas in nonvolatile (NVM), the data is retained even if the power is removed.

Inside the group of volatile memory, there are two types of Random Access Memories (RAM) : Static Random Access Memory (SRAM) and Dynamic Random Access Memory (DRAM). SRAM is usually used as cache in computer systems, and it has good performance in terms of fast read/write times (1ns/ 1ns) [15]. On the other hand, DRAM is used as main memory in computer (colloquially called the "RAM") and consists of one transistor and one capacitor. It stores information assigned the logic 1 when the capacitor is charged and the logic 0 when it is discharged, whereby the capacitor needs to be continually refreshed. SRAM and DRAM memories hold data as long as power is applied.

For permanent storage of information, one needs to work with non-volatile memories that can retain data even if the power supply turns-off. Inside this group, there are some options that differ from each other by the physical principle used to store information. Nowadays, flash memory is the most used because it is fast, small, economic and a reliable alternative for storing data [16]. It is composed of a metal-oxide-semiconductor (MOS) transistor with two gates : a floating gate and a control gate (see Fig. 1.1). It works by adding (charging) or removing (discharging) electrons to and from the floating gate, by tunnel effect when a high voltage at the gate is supplied [17]. When electrons are present on the floating gate, no current flows through the transistor, indicating a logic state 0. In contrast, when the floating gate is neutral, the transistor conducts, indicating a logic state 1 (see Fig. 1.1 [18]).

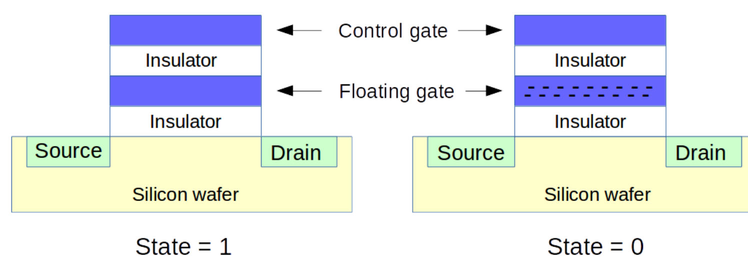

FIGURE 1.1. – Basic scheme of a flash memory cell. It consists of one metal-oxide-semiconductor with an additional floating gate. The logic state is 0 when electrons are presented in the floating gate, otherwise the state is 1 [18].

Depending on how the cells are organized in the matrix, it is possible to distinguish between NAND Flash memories and NOR Flash memories. In the former, the cells are connected in series to the bit lines, while in the second, they are connected in parallel. The series connections consume less space than the parallel ones, reducing the cost of NAND Flash [1]. Although Flash memories are widely used, they are quickly approaching the CMOS (complementary metal-oxide-semiconductor) scaling limits. In this way, some emerging memory technologies have been developed. The most promising option is the group of non-charge-based memories, including ferroelectric random access memory (FeRAM), phase change random access memory (PCRAM), magnetoresistive random access memory (MRAM), and Resistive random access memory (ReRAM) [19].

FeRAM is a type of random-access memory that uses a ferroelectric layer, with two distinct polarization states, to save information (see Fig. 1.2). However, FeRAM requires a large unit cell area ($>10F^2$) and its fabrication process is not compatible with CMOS technology [20]. PCRAM memory concept relies on the ability to switch between two states by joule heating and heat quenching that change the phase of the dielectric (see Fig. 1.2). There are two main problems with PCRAM : first, the energy required to heat the material is high, and second,

the heating and quenching processes lead to device fatigue [21]. On the other hand, the MRAM works with a configuration known as magnetic tunnel junction (MJT). The structure of these devices has two ferromagnetic layers with a tunnel barrier layer in the middle. One of the ferromagnetic layers has a fixed direction and it works as a reference layer, while the another is the free layer and it can change its direction by passing a driving current [22]. If two layers have the same direction, the digital state is "0" while with different directions the digital state is "1" (see Fig. 1.2). Nevertheless, the amount of current needed to reorient the magnetization is at present too high for most commercial applications [1].

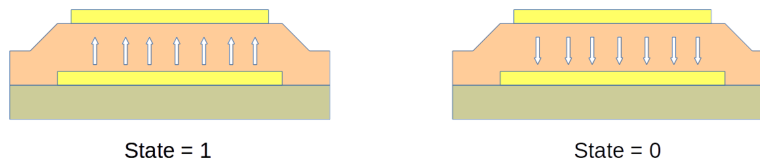

(a) FeRAM

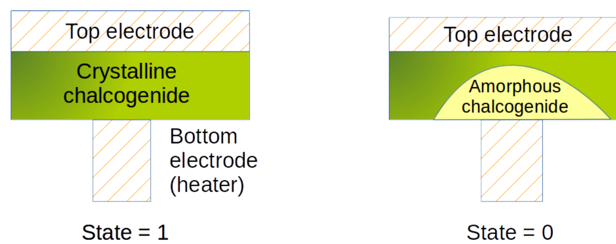

(b) PCRAM

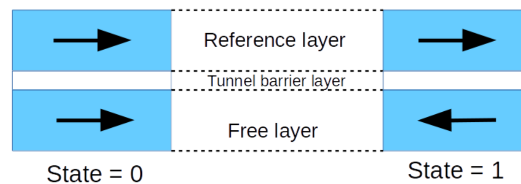

(c) MRAM

FIGURE 1.2. – (a) Schema of a typical ferroelectric random access memory (FRAM) cell [23]. (b) Schema of a phase change random access memory (PCRAM) cell (c) Schema of a magnetoresistive random access memory (MRAM) structure.

Resistive random access memories (ReRAM) are the most promising emerging memory technology to replace Flash devices. ReRAM has a smaller cell structure than MRAM, and it operates faster than PCRAM [1]. ReRAM has the MIM structure (see Fig. 1.3a), where top and bottom electrodes are metals (M) and

the switching layer is an insulator (I). It stores information using electrical resistance as the state variable, contrary to the charge store used in Flash technology. Its states, low resistive state (LRS) and high resistive state (HRS), correspond to binary 1 and 0 and can be toggled by applying two threshold voltage, V_{set} and V_{reset}.

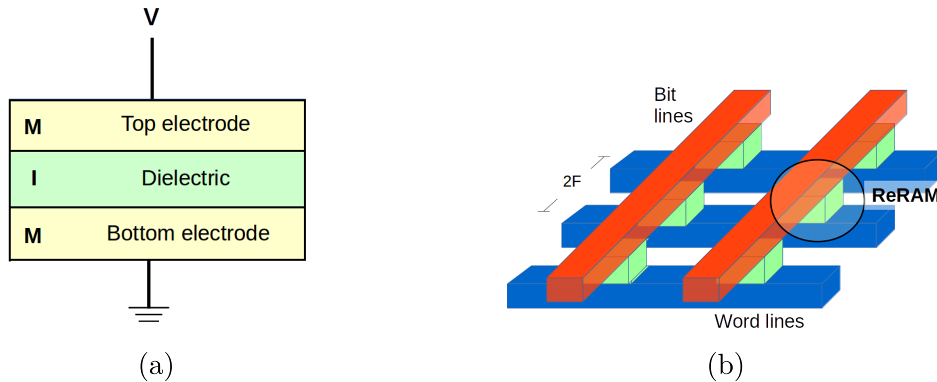

FIGURE 1.3. – (a) Schematic diagram metal-insulator-metal structure (MIM) of ReRAM. (b) Diagram of a cross-point memory architecture where word and bit lines allow to select a memory cell for writing and reading data [24]

One of ReRAM's main advantage is the compatibility with the actual flash memory technology. It can be incorporated into the cross-point arrays of word and bit-lines that are used for writing and reading data in a selected memory cell [24]. Regarding the high-density implementation, ReRAM devices can be arranged in crossbar architecture with a minimum memory cell area of $4F^2$ (see Fig. 1.3b). Further, ReRAM has good compatibility to CMOS fabrication process, which is fundamental for practical applications. They can be fabricated on metal layers or within the contact vias to the source and drain of MOSFET transistors [25]. In terms of performance, ReRAM has good cycling endurance [26, 27], moderate high speed [28] and short switching time [29]. Further, due to its relatively low-voltage operation, ReRAM can work with low program/erase energy that is needed for low-power consumption. In table 1.1 there is a comparison between the properties of non-volatile memories explained before : ReRAM, FeRAM, PCRAM and MRAM.

ReRAM is considered a promising candidate to substitute flash memory technology because all the characteristics mentioned above. However, ReRAM devices often show large variability in the electrical response due the stochastic nature of the switching process [30–32]. This feature must be studied for a successful modeling.

	ReRAM	**FeRAM**	**PCRAM**	**MRAM**
Operation Volgate (V)	3	0.6	3	1.8
Write time	<5ns	20ns	50ns	<100ns
Erase time	<5ns	20ns	120ns	<100ns
Read time	<10ns	20ns	<60ns	<20ns
Endurance	10^{12}	10^{14}	10^{12}	10^{14}

Table 1.1. – Comparison between the properties of non-volatile memory devices (2017) [3]

1.2. From resistive change materials to ReRAM

The first experimental observations of resistive switching could be dated in 1962 by Hickmott, who found the negative resistance in the systems : Al/SiO/Au, Al/Al_2O_3/Au, Ta/Ta_2O_5/Au, Zr/ZrO2/Au and Ti/TiO_2/Au [33]. Nevertheless, this effect has been observed in a variety of materials : perovskite oxide, binary oxides, chalcogenides, organic materials and amorphous silicon.

Specifically, the nonvolatile resistance switching applicable to ReRAM has been observed in many binary transition metal oxides (TMO) and multinary oxides [2, 34, 35]. Some examples are : NiO and CoO [36], Al_2O_3 [37], SnO_2 [38], MgO [39], Cu_2O [40], Nb_2O_5 [41], TiO_2 [8, 42–44], HfO_2 [4, 28, 45–56], among others.

The simple MIM structure of ReRAM device can produce different behaviors, not only due to the properties of the insulator material [25, 57], but also due to the metal electrodes and forming conditions, as it has been reported in the literature [2, 34, 35, 58]. Indeed, some morphological modifications could be created at the oxide-electrode interface due to the accumulation of mobile charge that can affect electrical response of the cell [59].

According to the electrochemical activeness of the electrode and switching mechanism, ReRAM devices can be classified into electrochemical metallization memories (ECM), valence change memories (VCM), and thermochemical memories (TCM) [60]. In ECM, also called conductive bridge RAM (CBRAM), the metallic ions from an active electrode (Ag, Ni or Cu) drift across the insulator and form a conductive filament (CF) [2, 35, 61]. In VCM, the generation of mobile oxygen ions within the insulator helps the formation of CF's. In this case, the electrodes are called inert (Pt, W or TiN) and they can block ion migration [2, 35]. On the other side, in TCM, the CF is built and destroyed by chemical reactions of reduction-oxidation that locally increase the temperature within the insulator [35, 62].

Among all materials proposed in the literature, we will work with ReRAM devices based on hafnium oxide (HfO_2). The HfO_2 is an electrical insulator with a band gap of 5.7eV and high dielectric constant (25 in comparison with 3.9 of silicon dioxide), which makes it an excellent candidate to be used as the insulator

in the MIM structure.

1.3. ReRAM operation

Most of ReRAM devices require an activation process, called electroforming, where a region of the insulator material changes and allows the resistance switching of the entire ReRAM. After this step, ReRAM is ready to work, and it can change between HRS and LRS according to three kinds of switching modes. These two characteristics will be explained in 1.3.1 and 1.3.2.

1.3.1. Activation step : electroforming process

The electroforming process is required to activate the switching properties of the ReRAM devices. In this step, the ReRAM changes from a very high resistive state, or pristine state, to a low resistive state [35, 63] by applying a high voltage stress, called forming voltage (V_{form}). It is higher than the normal operating voltage of the device, and induces a soft dielectric breakdown (SDB) on the insulator [64]. In the SDB, minor deformations in the oxide structure are generated under the influence of the voltage [65]. To prevent the permanent destruction of insulating properties, or hard dielectric breakdown (HDB), the electroforming is limited by a maximum current, called compliance current (I_c).

Depending on the insulator and the electrodes, the conduction paths created after electroforming are different and the switching mechanism can be classified as filamentary-type and interface-type (see Fig. 1.4).

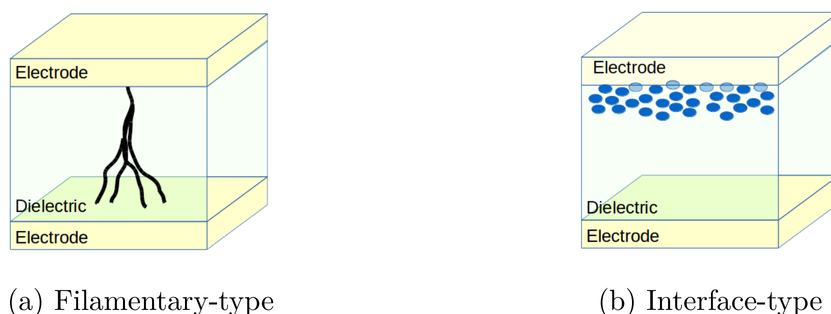

(a) Filamentary-type (b) Interface-type

FIGURE 1.4. – Proposed models for resistive switching can be classified according to either (a) a filamentary conducting path, or (b) an interface-type conducting path [66].

In the filamentary-type switching, a conductive filament (CF) has been created along the insulator as a result of the electro-reduction and the drift processes triggered by the electric field, that also are enhanced by electrical Joule heating [67]. During electroforming oxygen vacancies (V_O) are created under high

electric fields (> 10 MV/cm), and then, they are drifted towards the electrode, until their concentration is big enough to form localized and high conductance channels through the oxide [50]. These paths have been observed in various metal-oxide ReRAMs by conductive atomic force microscopy (C-AFM) [43, 68].

Previous studies show that the CF has a conical shape, stronger at the cathode interface and weaker at the anode interface [69, 70]. Thus, the CF is highly localized in a small fraction of the electrode area [58] and, set and reset processes are due to formation/rupture of the CF caused by the electrochemical migration of oxygen ions and redox reaction near the metal/oxide interface [66]. In this case, it is expected that set and reset transitions do not depend neither on the thickness of the oxide nor on the area-device. It has been reported that HfO_2-based ReRAM, studied in this work, has filamentary-type conduction [46, 71, 72].

The second type of switching is the interface-type and it is due to changes along the interface between the metal electrode and the insulator (see Fig. 1.4b). Contrary to filamentary switching, this type occurs at the whole area of the device. Various models have been proposed to explain the physical mechanism in this case, including : the migration of oxygen vacancies, the oxygen formation/annihilation reactions caused by the applied voltage and the change of Schottky barrier height formed at the metal-insulator interface [34, 73].

The influence of electrofoming step is fundamental in the electrical response of the ReRAM device because it determines current paths and device performance [74]. Experimentally, the current-voltage curve of electroforming shows a sudden change in current at the forming voltage

1.3.2. Switching modes

After electroforming, ReRAM devices are ready to work and can change its state between HRS and LRS by two switching modes : unipolar and bipolar. Although, some devices, called nonpolar, can have both kinds of switching at the same time.

A full physical description for set and reset switching when a ReRAM is under one of these modes is still incomplete [25]. However, most of the models recognize the importance of oxygen vacancies and oxygen migration in the process [44, 75]. In this section, the main characteristics of these switching modes are presented.

1.3.2.1. Unipolar switching

Unipolar switching occurs when the change of state depends on the amplitude of the applied voltage but is independent on its polarity. It means that set and reset occur at the same polarity. Figure 1.5 shows the unipolar-type resistive switching I-V characteristics for metal-oxide-based ReRAM devices. After the forming process, the cell (in LRS) is switched to HRS when the applied voltage achieves a

threshold voltage called reset voltage (V_{reset}). Then, by re-sweeping the voltage, the switching from HRS to LRS is achieved when the external voltage reaches the set voltage (V_{set}), that is larger than V_{reset}. In set process, the current is limited by a compliance current (I_c) [34].

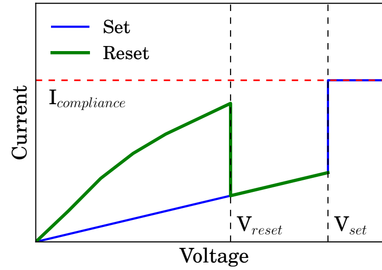

FIGURE 1.5. – Typical unipolar-type resistive switching I–V characteristics of a metal-binary oxide-metal device

The unipolar switching behavior is well described by the metallic filament model [76]. When the current is high enough, the reset process occurs by the destruction of the CF as a result of the thermo-chemical redox oxidation between the metallic elements, that constitute the CF, and the unbonded oxygen atoms [77, 78]. Unipolar mode has been observed in various oxides, such as NiO, TiO_2, Nb_2O_5, CaO, MgO, HfO, MnO_2 and Al_2O_3 [79].

1.3.2.2. Bipolar switching

Bipolar switching occurs when the change of state depends on the polarity of the applied voltage. Thus, set occurs under positive voltages and reset under negative voltages [25], as one can see in Fig. 1.6.

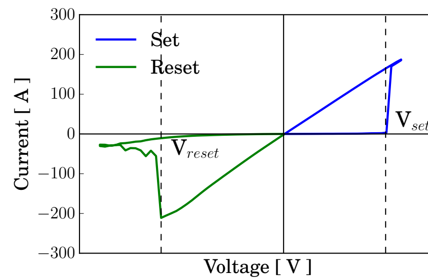

FIGURE 1.6. – Typical bipolar-type resistive switching I–V characteristics of a metal-binary oxide-metal device

Both, filament-type mechanism or interface-type mechanism, can produce bipolar resistive switching [34]. In the former, the change of state is originated by

the formation and rupture of a conductive filament. Meanwhile, in the interface-type, the switching occurs at the interface between the metal electrode and the oxide.

This type of resistive switching behavior occurs with many semiconducting oxides, such as complex perovskite oxides. Some examples are Pt/GdO_x/TaNx [80], Pt/Cr_2O_3/TiN and Pt/Cr_2O_3/Pt [81], Cu/AlN/Pt [82], Pt/$SrTiO_x$/Pt [83], HfO_2-based devices [28, 84], among others.

1.3.2.3. Nonpolar switching

There are some systems that present unipolar and bipolar switching at the same time. One example is the CoO-base ReRAM with a bottom electrode of Pt and a top electrode of Ti/Pt. By changing the thickness of the Ti layer, the device changes its operation mode. Devices with a 5nm-tick Ti layer are unipolar while those with 50nm-tick are bipolar [85].

In other devices, the nonpolar switching mode is determined by the compliance current during the electroforming process. Jeong et al [86] found both switching modes in Pt/TiO_2/Pt stacks. With lower compliance current (<0.1mA), the current-voltage curves showed bipolar switching while with a higher compliance current (1-10mA) the unipolar behavior is observed.

1.3.3. Conduction mechanism of ReRAM

To develop better modeling tools for ReRAM devices, it is important to understand the different kinds of conduction mechanism that can be involved in the electrical response. Some extensive studies have been reported in the literature [87–89], where it is accepted that the mechanisms are strongly dependent on the insulator/dielectric characteristics, fabrication process and electroforming conditions. In general, conduction mechanisms have been divided according to the region where they take place : interface or bulk.

1.3.3.1. Interface-type conduction mechanism

In interface-type the conduction depends on the electrical properties at the electrode-dielectric interface, e.g. the barrier height. There are mainly three mechanisms : Schottky emission, Fowler-Nordheim (F-N) tunneling and direct tunneling (DT), that are schematically represented in Fig. 1.7.

— Schottky emission is a thermally activated process where electrons are injected over the energy barrier into the conduction band of the oxide. This process plays an important role when temperature is relatively high [87].

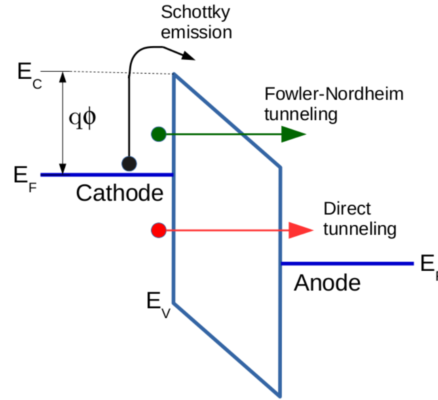

FIGURE 1.7. – Schematic energy band diagram of interface-type conduction mechanisms : Schottky emission, Fowler-Nordheim tunneling and direct tunneling [87]

— Direct tunneling is an important conduction mechanism in ultra-thin oxides (thinner than 3nm) where the electrons can tunnel directly from cathode to anode [89].
— Fowler-Nordhein (F-N) tunneling occurs under the presence of a high electric field that reduces the energy barrier and allows the electrons tunnel into the conduction band [87].

Expression for current density J for these conduction mechanisms are given by equations presented in table 1.2.

Conduction mechanism	Equation
Schottky emission	$J = \frac{4\pi q m^*(kT)^2}{h^3} \exp\left[\frac{-q(\phi_B - \sqrt{qE/4\pi\epsilon})}{kT}\right]$
Fowler-Nordheim	$J = \frac{q^2}{8\pi\phi_B} E^2 \exp\left[\frac{-8\pi\sqrt{2qm^*}}{3hE}\phi_B^{\frac{3}{2}}\right]$
Direct Tunneling	$J = \exp\left[\frac{-8\pi\sqrt{2q}}{3h}(m^*\phi_B)^{\frac{1}{2}}\kappa t_{ox}\right]$

m* is the electron effective mass, k is the Boltzmann's constant, T is the absolute temperature, h is the Planck's constant, E is the electric field across the oxide, ϕ_B is the barrier height, ϵ is the permittivity of the oxide, κ is the relative dielectric constant of the oxide and t_{ox} is the oxide thickness

TABLE 1.2. – Expressions for interface-type conduction mechanisms

1.3.3.2. Bulk-type conduction mechanism

Bulk conduction depends on the properties of the dielectric itself : dielectric relaxation time, density of states in conduction , carrier drift mobility, and trap characteristics (level, mean distance and density) [87]. Inside this group on can find ionic conduction, Poole-Frenkel (P-F) emission, Ohmic conduction, and trap assisted tunneling (TAT) [88], whose schematic representations are plotted in Fig. 1.8.

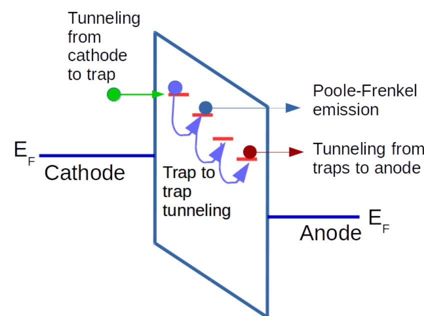

FIGURE 1.8. – Schematic of trap assisted tunneling conduction mechanisms : Poole-Frenkel emission, tunneling from cathode to traps, tunneling from traps to anode, and trap to trap tunneling.

— Ionic conduction is caused by the movement of ions under the influence of the applied electric field, and it is proportional to ion drift velocity [90]. Ions can jump over the potential barrier of different lattice defects in the dielectric and can produce ionic conduction [87].
— Poole-Frenkel (P-F) emission happens when the electric field decreases the potential barrier and trapped electrons get thermally excited and go from the dielectric to the conduction band [91].
— Trap-assisted tunneling process takes place when the oxide has substantial number of traps (particularly oxygen vacancies) [45]. The trap conduction can be due to electrons that tunnel from cathode to traps in the dielectric, electrons that go from trap to conduction band through F-N process or electrons that tunnel trap to trap from cathode to anode.
— Ohmic conduction is caused by the movement of mobile electrons in the conduction band and it is linearly dependent on the electric field [87].

The current density for bulk-type conduction mechanisms are given by equations presented in table 1.3.

Conduction mechanism	Equation
Ionic conduction	$J = J_o \exp\left[-\left(\frac{q\phi_B}{kT} - \frac{qEd}{2kT}\right)\right]$
Poole-Frenkel emission	$J = q\nu N_C E \exp\left[\frac{-q(\phi_T - \sqrt{\frac{qE}{\pi\epsilon}})}{kT}\right]$
Trap-assisted tunneling	$J = A\exp\left(\frac{-8\pi\sqrt{2qm^*}}{3hE}\phi_T^{\frac{3}{2}}\right)$
Ohmic conduction	$J = \sigma E = q\nu N_C E \exp\left[-\frac{(E_C - E_F)}{kT}\right]$

J_o es the proportional constant, $q\phi_B$ is the potential barrier height, E is the applied electric field, d is the distance between two jumping sites, k is the Boltzmann's constant, T is the absolute temperature, ν is the electronic drift mobility, ϕ_T is the depth of traps potential well, A is a constant, N_C is the effective density of states of the conduction band, E_C is the conduction band, E_F is the Fermi energy level

TABLE 1.3. – Expressions for bulk-type conduction mechanisms

1.3.4. Preliminary studies of HfO_2-based ReRAM

Among the possible insulator materials that exhibit resistive switching, hafnium oxide (HfO_2) has been considered as a good option due to its positive results as a high-κ dielectric for high-performance MOSFET's [92]. In the MIM structure different types of electrodes, such as Pt, Cu and TiN, have been reported with HfO_2 : TiN/HfO_2/Pt [47], Cu/HfO_2/Pt [93], Au/HfO_2/TiN [48], TiN/HfO_x/TiN [71]. In this research, we will work with TiN/HfO_2/Hf/TiN devices. Excellent performance for this kind of ReRAM has been reported in the literature due to the presence of the Hf capping layer [57].

The filamentary conduction has been widely accepted to explain the switching process of HfO_2-based ReRAM [50]. During the electroforming, the conductive filament CF, is formed by the breakage of metal-oxygen bonds and the subsequent out-diffusion of the oxygen ions that creates a rich-oxygen deficient region in the dielectric [50, 51]. The change of state is attributed to the formation and the rupture of this CF that can be composed of some conductive paths. The reported set and reset operation voltages are less than 1.5V with a compliance current of 200μA [94].

Regarding to electroforming, it has been found that the forming voltage is linearly dependent of the thickness of the HfO_2 film beyond 5nm [94]. However, HfO_x-based devices could be forming-free when the insulator is only 3nm thick [10]. In our samples, the thickness of the layer is 10nm, so it is expected that the forming voltage will be around 5V.

In the literature some models have been proposed to explain the resistive switching in this kind of ReRAM [4, 10, 48, 84, 95, 96]. Some of them are explained

in appendix D. However, one of the most accepted model to explain resistive switching in this system is the Quantum Point-Contact model (QPC) [26, 84, 97, 98]. QPC model assumes the existence of a filamentary path across the dielectric film that allows electrical conduction. The difference between the two states, HRS or LRS, is attributed to the change of the potential barrier caused by size modulation of thinnest part of the CF that acts a quantum point contact. It is explained in detail in appendix D.1.

In this work, a new model for HfO_2-based ReRAM is presented. To do it, first, we will analyze the electrical response of devices of nine different areas. After, we will develop a phenomenological model based on the results of the electrical characterization. Finally, the influence of the measurement element will be considered in the model.

2. HfO_2-based ReRAM fabrication, activation and electrical characterization

Summary

2.1 Device fabrication . . . 39
2.2 Device structure . . . 40
2.3 Electrical characterization . . . 41
2.4 Electroforming : cell activation . . . 42
2.5 Electrical characterization of HfO_2-based ReRAM . . . 46
2.5.1 Set and reset voltage study . . . 47
2.5.2 ON/OFF ratio . . . 53
2.5.3 Analysis of the conduction mechanism . . . 54
2.5.3.1 Ohmic conduction . . . 55
2.5.3.2 Trap assisted tunneling conduction (TAT) . . . 57
2.5.4 Different electrical response of the samples electroformed with I_c=5mA and I_c=10mA . . . 64
2.6 Stochastic Nature of ReRAM . . . 66

2.1. Device fabrication

In this thesis, we worked with TiN/HfO_2/Hf/TiN stacks fabricated by IMEC (Leuven, Belgium) according with the process flow presented in figure 2.1b. Imec's devices are based on 65nm silicon CMOS process and built on top of a transistor's drain contact via (1T1R) [57].

First, the transistor (1T) is built with front-end-of-line (FEOL) process. Then, 100nm thick TiN is deposited as a bottom electrode (BE) by physical-vapor-deposition method (PVD) [99] where the electrical connection to the select transistor is realized by the tungsten (W) plug. After, a SiO_2 hard mask is deposited by chemical-vapor-deposition (CVD) to produce a thinner layer film with high electrical resistance. This process is followed by two steps, first lithography, to transfer the pattern to the surface of the wafer, and after dry etch, to remove the

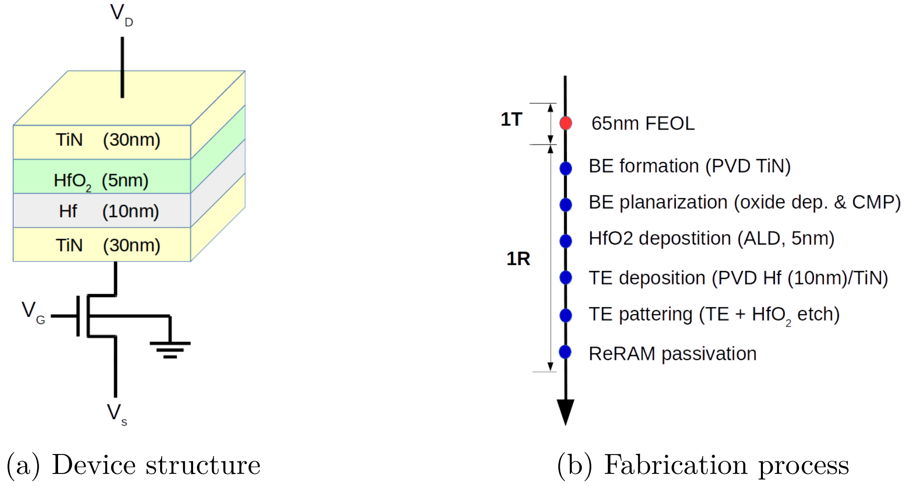

(a) Device structure (b) Fabrication process

FIGURE 2.1. – (a) HfO_2-based integrated 1T1R ReRAM devices structure, consisting of Ti/HfO_2/Hf/TiN stacks. (b) IMEC's device fabrication process flow.

material and create the patterns. Finally, 200nm of SiO_2 is deposited by chemical-mechanical planarization (CMP) to the TiN bottom electrode.

To build the switching layer, first, 5nm of HfO_2 is deposited by atomic layer deposition (ALD) at 300°C using $HfCl_4$ as precursor and H_2O as oxidant. After, the top electrode, composed by a Hf capping layer of 10nm and a TiN layer of 30nm, is deposited by physical-vapor-deposition (PVD), followed by lithography. Finally, passivation process and etch processes are applied to protect the cell from external agents, followed by the deposition of Si_3N_4 and SiO_2 by CVD. It is important to note that HfO_2 thickness and Hf capping layer thickness is the same for all devices regardless the area.

All the methods mentioned above (ALD, PVD, CVD, CMP, lithography, dry etch and passivation) are explained in appendix B due to the importance of fabrication process on the current-voltage response of ReRAM devices.

2.2. Device structure

The ReRAM cells consist of TiN(30nm)/ HfO_2(5nm)/ Hf(10nm)/ TiN(30nm) stacks of nine different areas : 55x55nm^2, 65x65nm^2, 75x75nm^2, 85x85nm^2, 105x105nm^2, 135x135nm^2, 1x1μm^2, 3x3μm^2 and 5x5μm^2.

The one-transistor and one-resistor (1T1R) architecture has been used to enable accurate characterization due to the small area of the devices [57]. The 1T1R array eliminates the sneak path current, thereby decreasing the energy consumption and causing higher reliability [100]. As it was explained in 2.1, the 1T1R structure is obtained by the integration of a MIM device with a metal-

oxide semiconductor field effect transistor (MOSFET) that acts as access device and allows the programming operation of a selected cell (see Fig. 2.1a).

2.3. Electrical characterization

The initial state of the ReRAM is the pristine state, where the cell has a very high resistance. The electroforming is the first step to activate the device and to allow the switching between high resistive state (HRS) and low resistive state (LRS). The change between HRS and LRS is called set, while the change between LRS and HRS is called reset. A schema of this procedure is presented in figure 2.2. Electroforming and set are achieving by applying positive voltages to the top electrode (TE) while reset is obtained by applying negative voltages. A compliance current, I_c, controlled by the MOSFET transistor, is fixed during all process to prevent the hard dielectric breakdown of the samples.

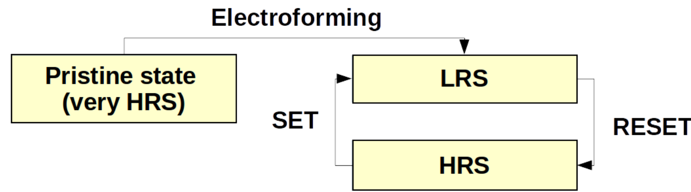

FIGURE 2.2. – Electrical characterization process of HfO_2-based ReRAM devices.

Electrical characterization was done by using a Cascade Alessi REL 4800 equipment along with a wafer load probe station (Fig. 2.3). The wafer was mounted in the station, and the ReRAM structure was chosen with the help of a microscope. After, the probes were located on the ReRAM cell and the measurement were programmed using the Keithley Interactive Test Environment (KITE).

To study the effect of compliance current (I_c) during electroforming, two groups of samples were electroformed. First, all samples were electroformed with I_c=5mA, and after, another group (55x55nm^2, 65x65nm^2, 1x1μm^2, 3x3μm^2, and 5x5μm^2) were electroformed with I_c=10mA.

The electrical characterizations were performed by applying the bias to the top electrode. For set, the voltage sweep increased from 0V to 1.7V and returned to 0V in 0.05V step. For reset, voltage sweep was from 0V to -1.8V and returned to 0V. Such as in electroforming, two values of compliance current were applied, I_c=5mA and I_c=10mA. We worked with 10 to 15 experiments of 10 cycles each one. However, it has been reported that the value of compliance current during reset plays an insignificant role in the performance of Hf-based ReRAM's because annihilation of conducting filament is more sensitive to the driving electrical field than joule heat introduced by current [101].

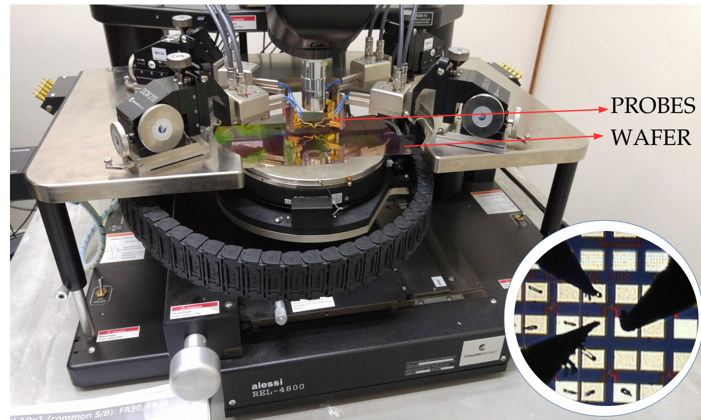

FIGURE 2.3. – Electrical characterization of the ReRAM device on a wafer probe station

2.4. Electroforming : cell activation

During electroforming, two values of compliance current (I_c) were applied to analyze the characteristics of the IV response. In this samples, an I_c less than 5mA is not strong enough to achieve the low resistive state, while an I_c larger than 10mA causes the destruction of the devices due to a high dielectric breakdown of the insulator layer.

The I-V characteristics during electroforming process are shown in Fig. 2.4 and 2.5 for nm-size and μm-size samples. From these curves, forming voltage (V_{form}) can be determined when the system reaches an abrupt current increase at first time (I_{form}) [102]. After the jump, the small virgin conductance permanently changes, which means that the device is ready to electrical operation. This current jump suggests the formation of the conductive filament. In Hf-based ReRAM's, it has been reported that this is mainly a field driven process [71], where the electric field provides the required energy for moving the pre-existing vacancies and for creating new ones thanks to the breaking of Hf-O bonds and the subsequent diffusion of oxygen ions [67]. It must be noted that all devices have been fabricated under same conditions (see sec. 2.1), so it is expected that all of them have similar pre-existing oxygen vacancies profiles. However, the observed variability is an evidence of the stochastic nature of the electroforming process that forms filaments of various size and at different location.

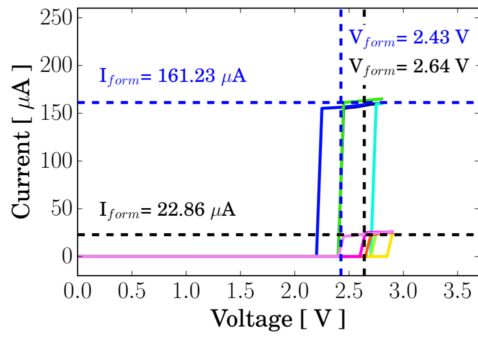

(a) 55x55nm^2

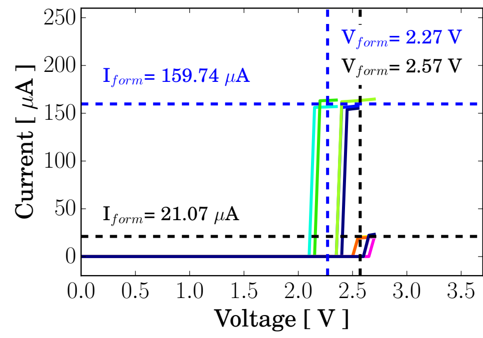

(b) 65x65nm^2

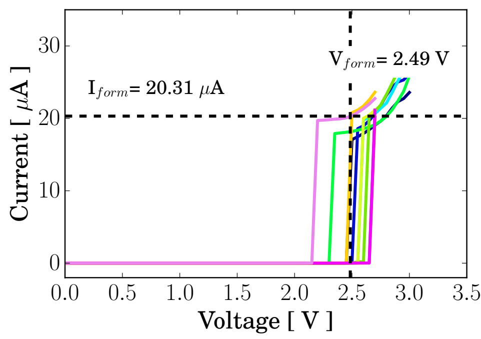

(c) 75x75nm^2

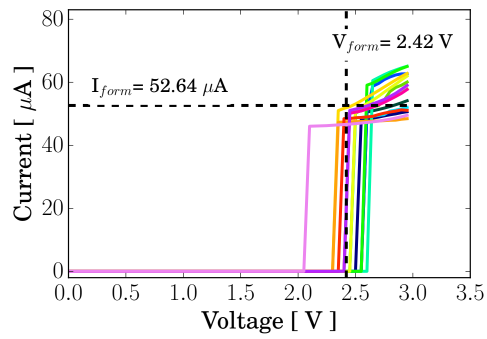

(d) 85x85nm^2

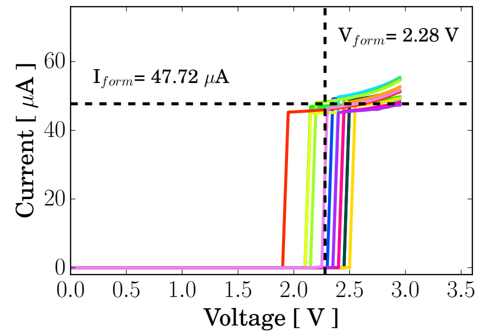

(e) 105x105nm^2

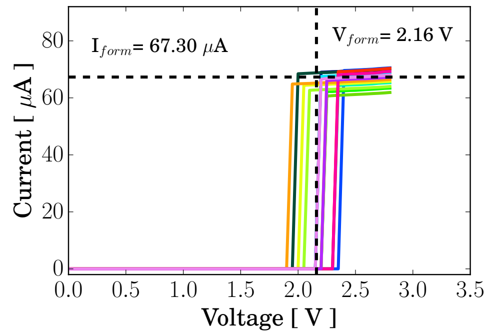

(f) 135x135nm^2

FIGURE 2.4. – Current-voltage characteristics of the HfO_2-based ReRAM devices of nm^2-cell area during electroforming at a positive applied bias with I_c=5mA in black and I_c=10mA in blue.

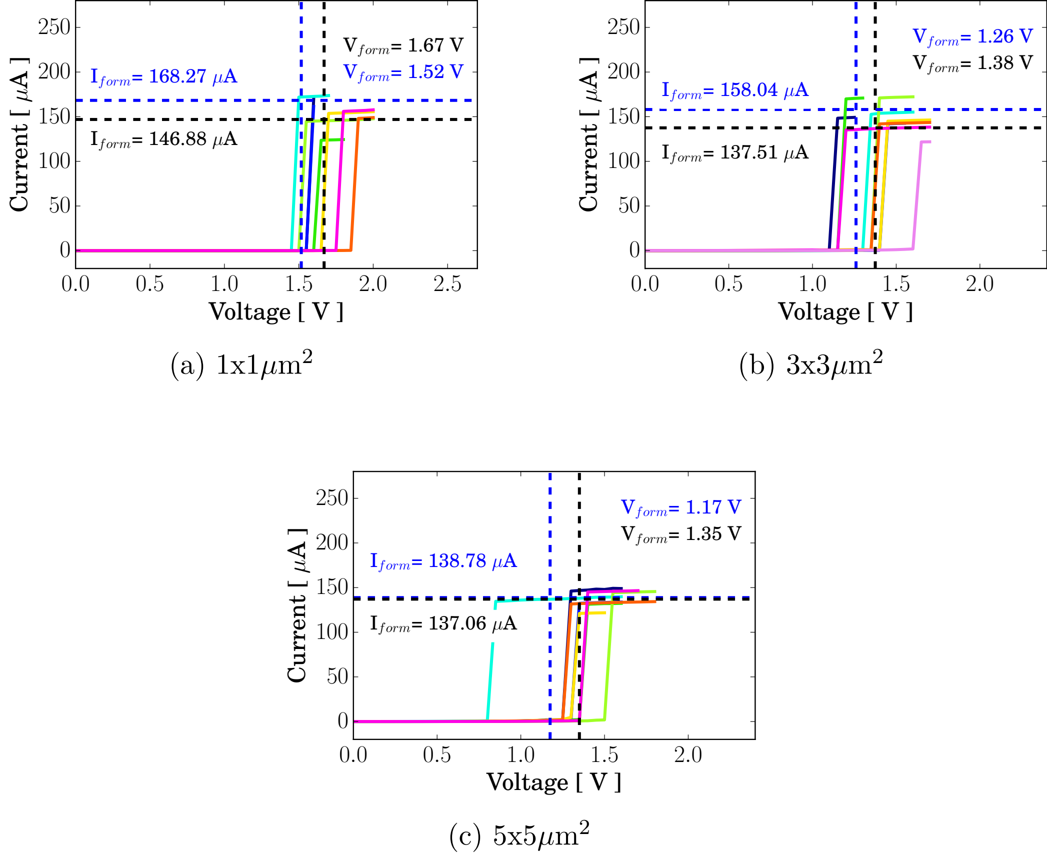

FIGURE 2.5. – Current-voltage characteristics of the HfO_2-based ReRAM devices of μm^2-cell area during electroforming at a positive applied bias with I_c=5mA in black and I_c=10mA in blue.

To compare the electrical response between samples during electroforming process, V_{form} and I_{form} as a function of device area are presented in Fig. 2.6. It is found that smaller-area devices require larger voltage to be electroformed, presumably due to few electrically weak points per unit area [103] that limit the locations to trigger electroforming [104]. On the other hand, I_{form} is almost independent of the device area when I_c is 10mA (see Fig. 2.6b), while it tends to increase when I_c is 5mA. One could infer that 10mA is a saturation value for compliance current in this type of samples.

These differences could be closely related to the shape and the size (number of conducing paths) formed by oxygen vacancies. When I_c is small, few oxygen vacancies are generated and the CF could be thinner. Meanwhile, when I_c increases, more oxygen vacancies are generated such that a cilindrical CF could be formed

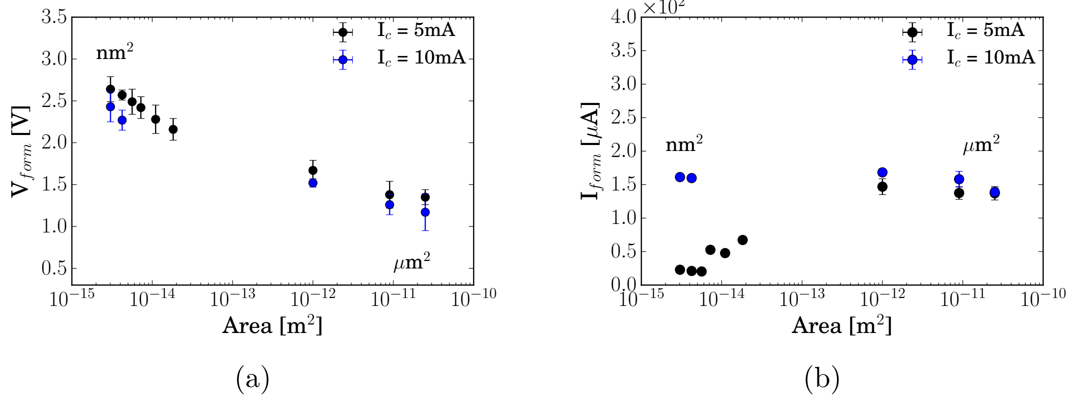

FIGURE 2.6. – Area scaling trends for (a) forming voltage (V_{form}) and (b) forming forming current (I_{form}). One can compare the effect of I_c in these values during electroforming.

[105]. As a result, a higher I_c during electroforming results in the formation of stronger and less resistive filaments. One could prove this hypothesis in Fig. 2.7 where the forming conductance (G_{form}) vs. device area is presented. Although conductance tends to increase with the area in both cases, the values of G_{form} are bigger in those samples electroforming with I_c=10mA.

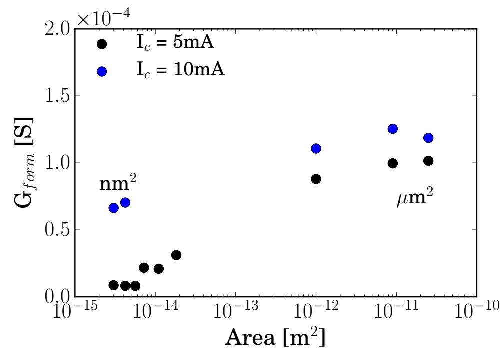

FIGURE 2.7. – Forming conductance as a function of the device-area

As a summary of electroforming process, mean values of V_{form} and I_{form} are presented in table 2.1. A deeper analysis of the effect of compliance current during electroforming in the current-voltage characteristics will be presented in section 2.5.4.

	I_{comp}=5mA		I_{comp}=10mA	
Sample	$V_{forming}$ [V]	$I_{forming}$ [μA]	$V_{forming}$ [V]	$I_{forming}$ [μA]
55x55 nm^2	2.64 ± 0.15	22.86 ± 0.41	2.43 ± 0.18	161.23 ± 2.25
65x65 nm^2	2.57 ± 0.06	21.07 ± 1.19	2.27 ± 0.12	159.74 ± 3.86
75x75 nm^2	2.49 ± 0.15	20.31 ± 2.14	-	-
85x85 nm^2	2.42 ± 0.13	52.64 ± 5.15	-	-
105x105 nm^2	2.28 ± 0.17	47.72 ± 2.49	-	-
135x135 nm^2	2.16 ± 0.13	67.30 ± 2.67	-	-
1x1 μm^2	1.67 ± 0.12	146.88 ± 11.86	1.52 ± 0.05	168.27 ± 5.09
3x3 μm^2	1.38 ± 0.16	137.51 ± 9.46	1.26 ± 0.12	158.04 ± 11.75
5x5 μm^2	1.35 ± 0.09	137.06 ± 10.05	1.17 ± 0.22	138.78 ± 6.62

TABLE 2.1. – Forming voltage (V_{form}) and current (I_{form}) for HfO_2-based ReRAM devices of nm^2-cell area and μm^2-cell area.

2.5. Electrical characterization of HfO_2-based ReRAM

In this section, the analysis of the electrical response for the devices electroformed with I_c=5mA is presented. Current-voltage characteristics for nm-size and μm-size samples are plotted in Fig. 2.8 and 2.9. In reset region, the absolute values of the negative current had been plotted along with the positive set current. The typical hysteresis curve with a "butterfly" shape, reported before for HfO_2-based ReRAM [46, 48, 50], is observed in all cases.

All curves show a cycle to cycle variability that is more evident when the system is in HRS. This is a common characteristic of ReRAM devices and must be studied in order to achieve the accurate modeling of these devices. Another important characteristic is the evidence of current drops between several intermediate states. It has been reported before [49] and reveals the discrete nature of paths that form the CF.

The analysis of experimental IV curves allows the extraction of some parameters involved in the resistive switching. First, two characteristic threshold voltages can be identified by the abrupt current change, observed under positive and negative voltages. They are called set and reset voltages, V_{set} and V_{reset} respectively. Second, the main conduction mechanisms when the system is in HRS or LRS can be identified. Although the electrical behavior of the ReRAM is subjugated to some conduction processes happening simultaneously inside the CF and the insulator, the voltage-current relationship allows us to describe the main mechanisms. Indeed, the linear relationship in LRS is an evidence of Ohmic behavior, while the exponential dependency in HRS is attributed to tunneling conduction, specifically to trap assisted tunneling (TAT).

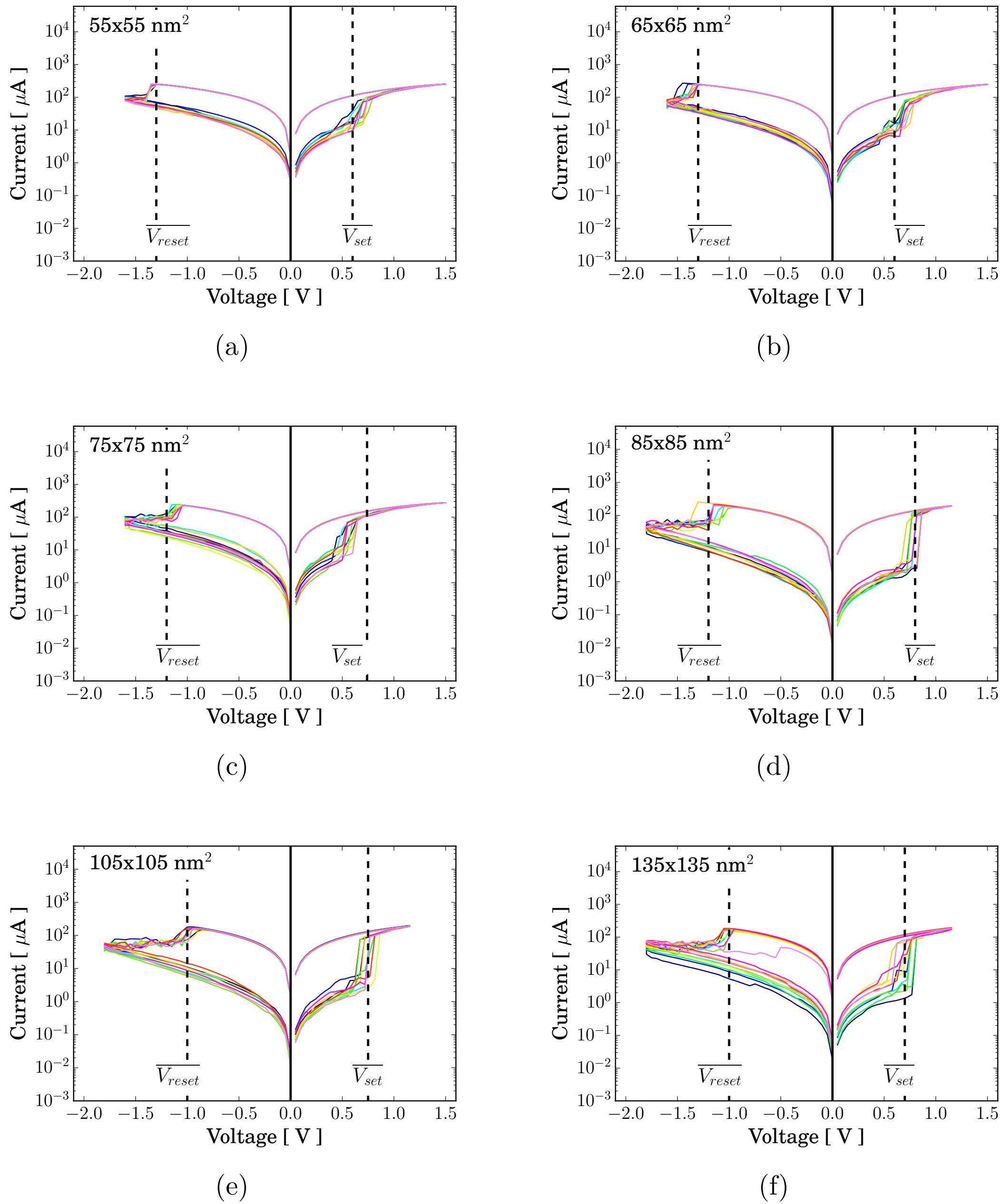

FIGURE 2.8. – Current–voltage characteristics of HfO_2-based ReRAM devices of nm^2-cell area, during one experiment of ten cycles. The devices show bipolar resistive switching behavior.

2.5.1. Set and reset voltage study

The I-V response is different between cycles in all devices. As example, figure 2.10 shows 150 cycles of resistive switching operation under positive and negative voltage sweeps for the sample of 85x85nm^2. One can identify, with the

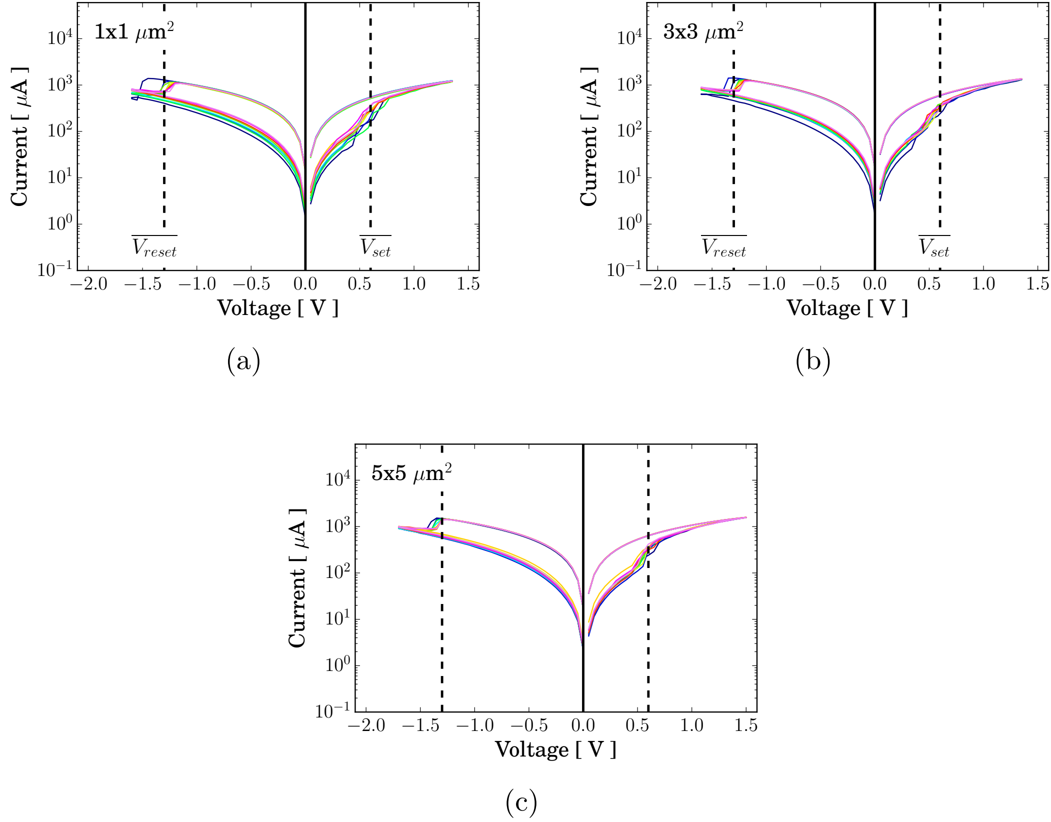

FIGURE 2.9. – Current–voltage characteristics of HfO_2-based ReRAM devices of μm^2-cell area, during one experiment of ten cycles. The devices show bipolar resistive switching behavior.

two cycles in color, that the points where set and reset transitions take place are clearly different (points A and B). Further, several intermediate jumps in the transitions from HRS to LRS (or from LRS to HRS) can be observed.

However, although the samples show electrical variability, there is no evidence of degradation during experiments or cycles. Analysis of voltage variability was carried out to confirm it (see Fig. 2.11). We have to mention that there are two types of variability : device-to-device variability and cycle-to-cycle variability. The first characterizes the uniformity of memory arrays and the second characterizes device stability [106]. In this work, we will study only device response, assuming a good control of the fabrication array process.

A python-based script detects V_{set} and V_{reset} from experimental data. This script recognizes the point where an abrupt change of current occurs. V_{set} when there is an increment of current under positive bias and V_{reset} when there is a decrease of current under negative bias. Figure 2.11 shows the voltage distribution during cycles for one small (65x65 nm^2) and one big sample (3x3 μm^2). The voltage distribution, in both cases, is always inside the same range of values,

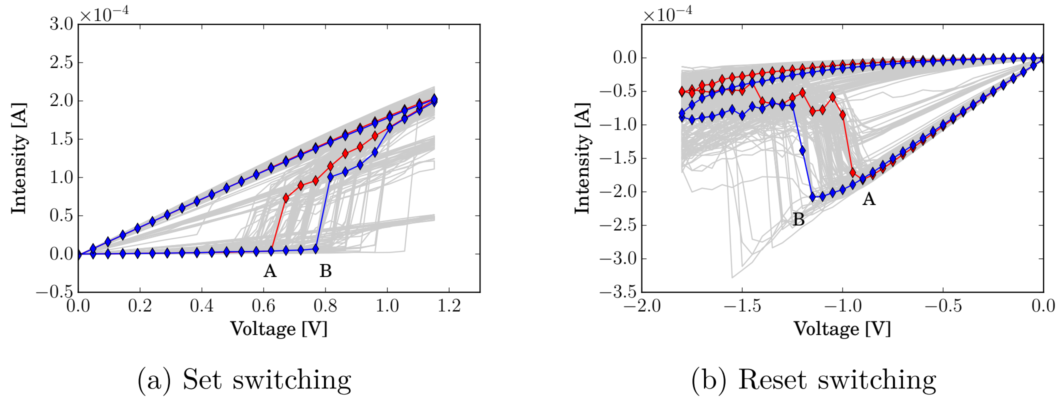

(a) Set switching

(b) Reset switching

FIGURE 2.10. – Current–voltage characteristics during set and reset process of the HfO_2-based ReRAM of 85x85nm^2. One can identify the cycle to cycle variability. As example, two cycles in color are presented.

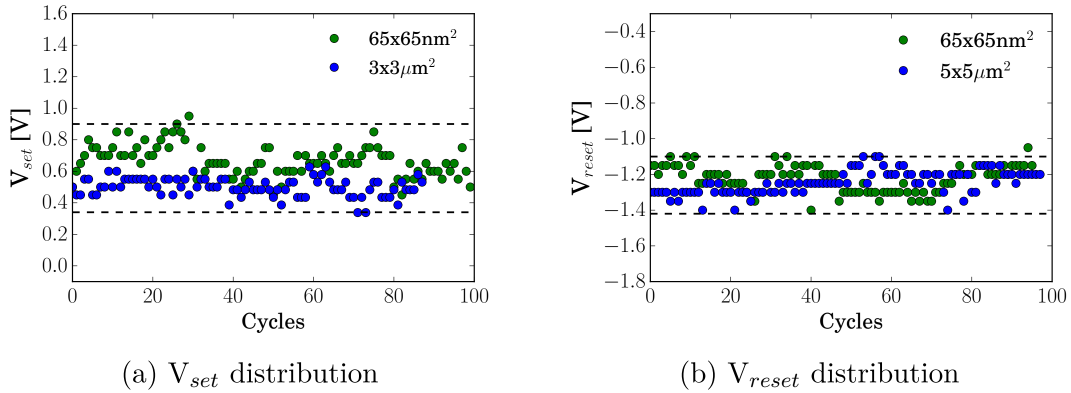

(a) V_{set} distribution

(b) V_{reset} distribution

FIGURE 2.11. – Distribution of V_{set} and V_{reset} values, obtained from experimental data, for two samples, 65x65nm^2 (green dots) and 5x5μm^2 (blue dots)

which implies that samples are not suffering degradation. Important changes in voltages, such as the decrease in value, could be derived from the generation of new oxygen vacancies [107]. In this work, we do not find dependence of V_{set} and V_{reset} with the cycling in any sample.

Now, the statistical analysis of V_{set} and V_{reset} is done. The histograms of V_{set} and V_{reset} are in figures 2.12 and 2.13, respectively. One can describe them as unimodal, where the mean value is the most suitable measure to describe each group with a dispersion given by the standard deviation. Further, the Gaussian function has been included in those samples where the set of data could be well-modeled by a normal distribution. To prove it, a normality test has been applied for both, V_{set} and V_{reset}, and it is presented in appendix C.

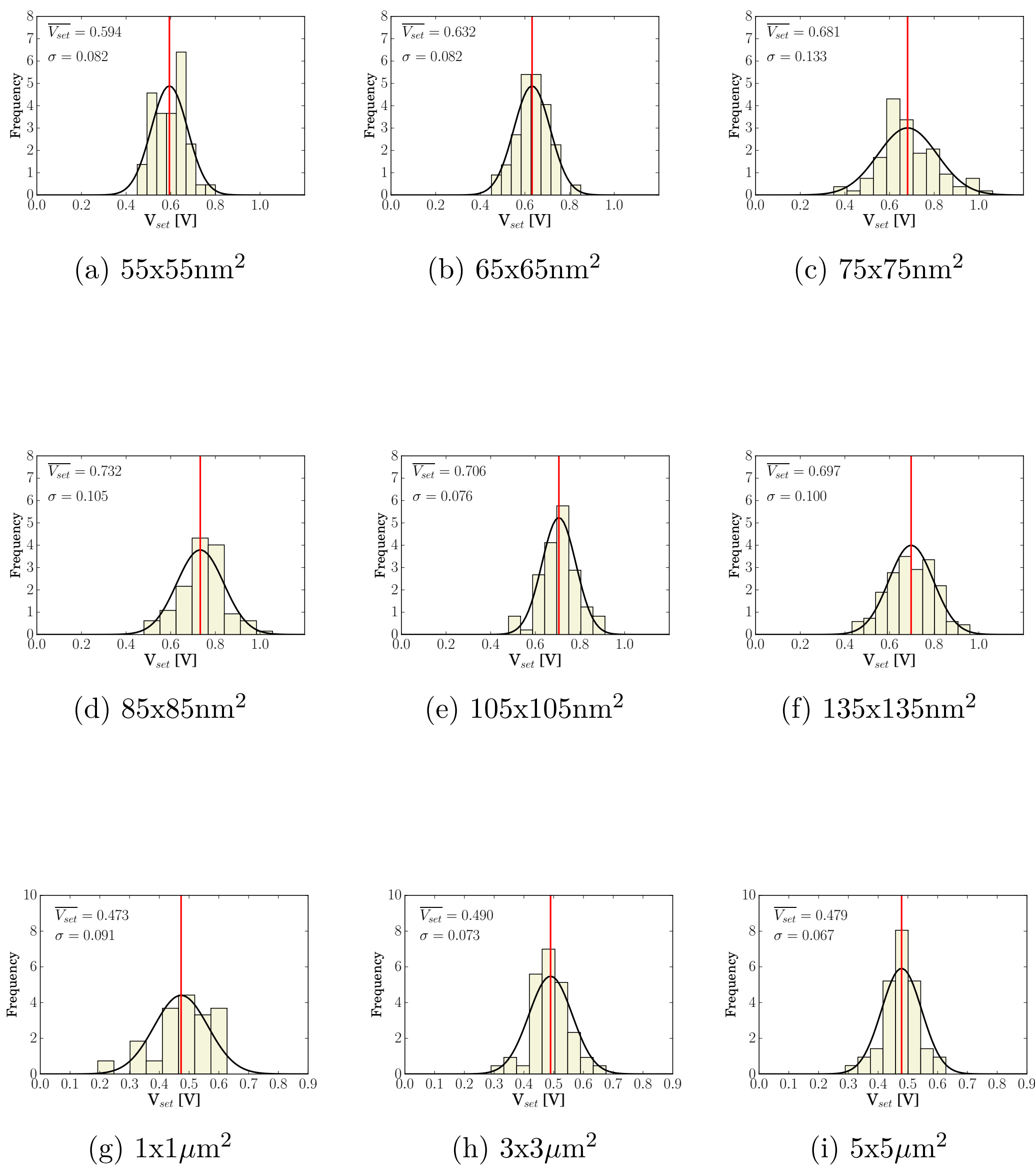

(a) 55x55nm^2 (b) 65x65nm^2 (c) 75x75nm^2

(d) 85x85nm^2 (e) 105x105nm^2 (f) 135x135nm^2

(g) 1x1μm^2 (h) 3x3μm^2 (i) 5x5μm^2

FIGURE 2.12. – Statistical distribution of set voltage (V_{set}) of HfO_2-based ReRAM devices.

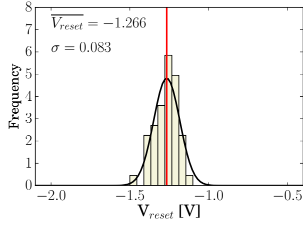

(a) 55x55nm^2

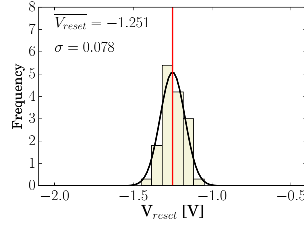

(b) 65x65nm^2

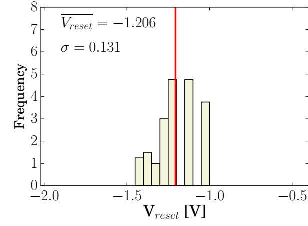

(c) 75x75nm^2

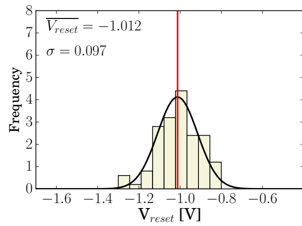

(d) 85x85nm^2

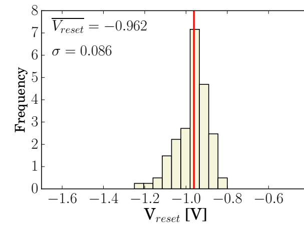

(e) 105x105nm^2

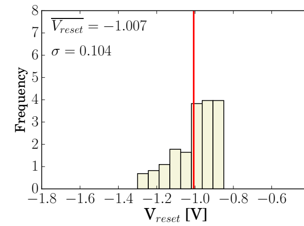

(f) 135x135nm^2

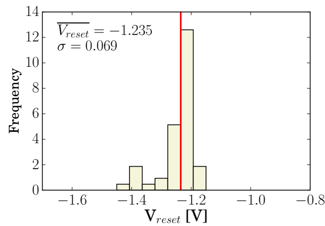

(g) 1x1μm^2

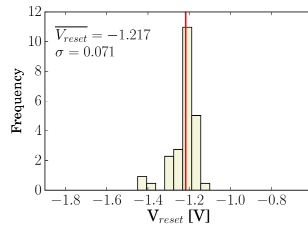

(h) 3x3μm^2

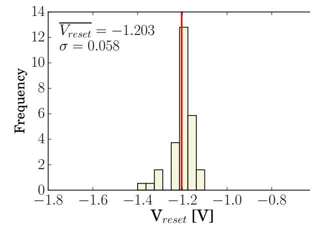

(i) 5x5μm^2

FIGURE 2.13. – Statistical distribution of reset voltage (V_{reset}) of HfO_2-based ReRAM devices.

The fact that V_{set} and V_{reset} have a wide distribution of values is an evidence of the stochastic nature of the switching behavior. According to filamentary switching mechanism, the CF could be localized inside the dielectric but composed of different paths formed by oxygen vacancies. The resistance switching is caused by the formation and rupture of these paths during set and reset transition. This fact has been experimentally confirmed in HfO_2/TiN structure [72] and in NiO-based systems [108]. Thus, by applying positive voltage, set process occurs because there is a random reconnection of some paths due to oxidation/reduction processes of oxygen anions and vacancies, and their migration through dielectric, specially at the interfaces [35, 109].

Nevertheless, the mechanism for reset transition caused by the destruction of those paths is still unclear. Although, two main mechanisms could be considered to the filling up of the oxygen vacancies with the consequent rupturing of the filament [49, 110] : drift of oxygen ions by electric field and diffusion of oxygen ions caused by concentration gradient of oxygen ions [111]. Also, Joule heat might play a crucial role. All of them are unpredictable processes and might generate the wide distribution V_{reset} values, that cannot be represented by a Gaussian distribution, as one can see in Fig. 2.13.

Now, the area dependence of V_{set} and V_{reset} is studied (see Fig. 2.14). During set process, one could identify one characteristic mean value for nm-size samples and one for μm-size samples. Although it has been reported area-independence of set voltage in devices with resistive switching based on CF, it is important to note that μm-size samples are 10^6 bigger than nm-size samples, which could contribute to the formation of a thicker CF that require less energy to be built. On the other hand, V_{reset} appears to have only one value along all samples. It could imply that the mechanism required for reset is the same along all samples and for this, the energy required is similar.

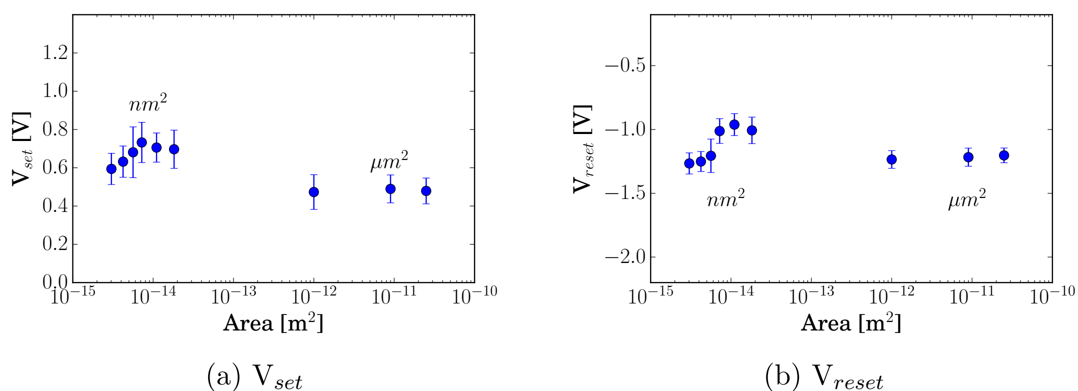

FIGURE 2.14. – V_{set} and V_{reset} as a function of the area of HfO_2-based ReRAM devices.

According with these results, V_{reset} is always bigger than V_{set}, but both are

smaller than V_{form}. Although, big differences among samples were reported for electroforming, these characteristic voltages are similar for all of them.

2.5.2. ON/OFF ratio

The ON/OFF ratio represents the resistive window of the ReRAM and it is way to measure the performance of a device. It is computed by the relationship of the electrical resistance between LRS and HRS, or by the relationship between the currents in LRS and HRS around V_{set} (or V_{reset}), as one can see in the schema of Fig. 2.15.

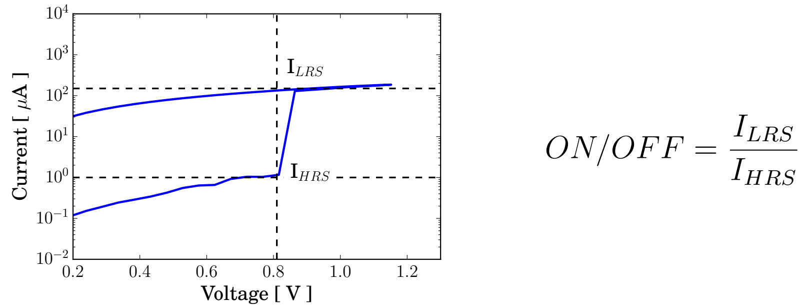

FIGURE 2.15. – IV response for a ReRAM device. At a critical voltage (V_{set}), the current abruptly increases. The relationship between currents gives the ON/OFF ratio

The I-V characteristics of ReRAM devices, presented in figures 2.8 and 2.9, show that the separation between HRS and LRS is bigger in small samples. To quantize the difference, the ON/OFF ratio of all devices has been determined and compared in figure 2.16. The fact that this ratio was one order of magnitude bigger in small devices means that resistance switching (RS) effect is enhanced with the scalability.

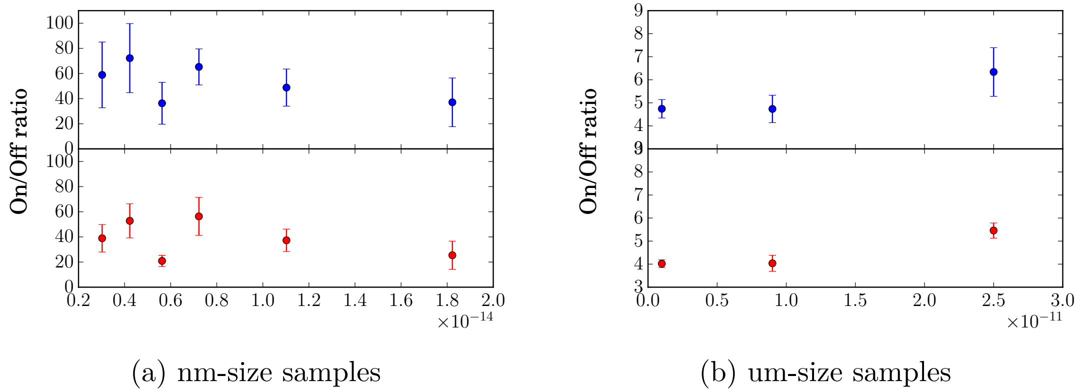

(a) nm-size samples

(b) um-size samples

FIGURE 2.16. – On/off ratio for set (blue) and reset (red) regions.

This result sugests that HfO_2-based ReRAM devices of nm-size could be a good option to be used in high density storage class memory architecture. However, it is also important to consider that variability mostly affects smaller samples.

2.5.3. Analysis of the conduction mechanism

HfO_2-based ReRAM devices have filamentary conduction and the change of state (HRS or LRS) is possible thanks to the CF changes during set and reset transition [50]. In a conductance-voltage curve one can identify this CF modulation. It means, the quantized conductance steps, with multiples of G_o, and the abrupt conductance transition between HRS and LRS. As example, figures 2.17 and 2.18 show the typical set and reset conductance-voltage curves (G-V) for one sample of each type. One can note that the conductance is one order of magnitude bigger in big samples. In these plots, the conductance is presented in units of the quantum conductance $G_0 = 2e^2/h$= 7.748×10^{-5}S.

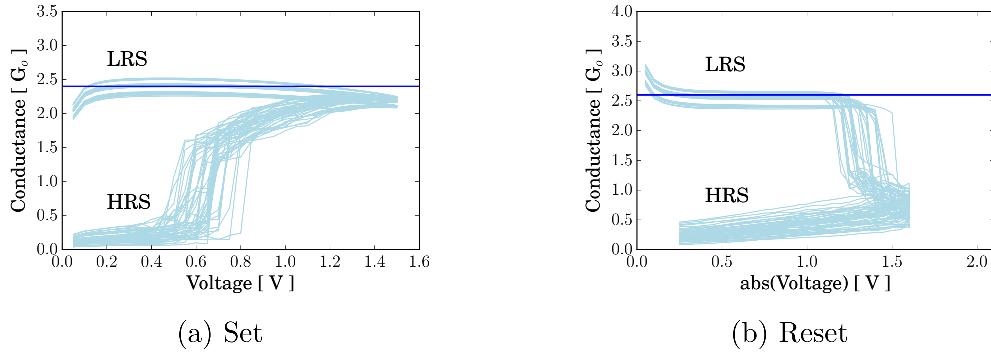

(a) Set (b) Reset

FIGURE 2.17. – Conductance-voltage curve for the HfO_2-based ReRAM device of 55x55nm^2.

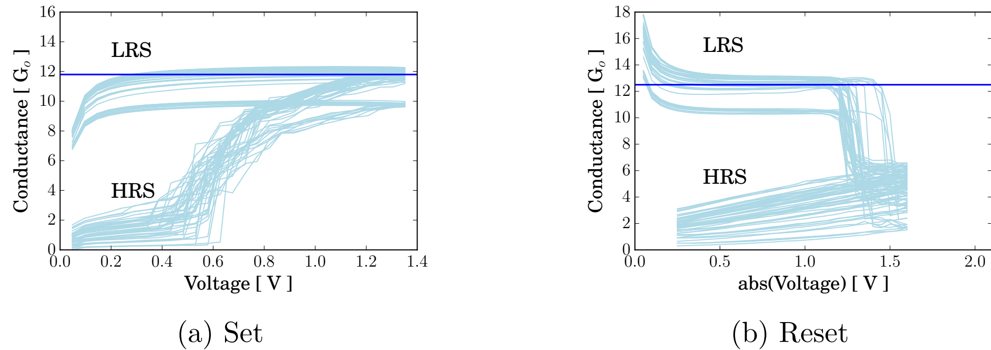

(a) Set (b) Reset

FIGURE 2.18. – Conductance-voltage curve for the HfO_2-based ReRAM device of 1x1μm^2.

Figures 2.17 and 2.18 also reveal the successive current drops that cause successive conductance steps for both, set and reset processes. These intermediate states are evidence of the discrete nature of the CF [49].

From IV curves (Fig. 2.8 and 2.9), one can identify that the main conduction mechanism is Ohmic in LRS and trap assisted tunneling in HRS. In this section, we determine three parameters to describe these two mechanisms. First, we proved that the electrical response, under positive and negative voltages, is symmetric in all devices. As example, in Fig. 2.19 the absolute value of current vs. the absolute value of voltage is plotted for one small sample (55x55nm^2) and for one big sample (3x3μm^2) during one cycle.

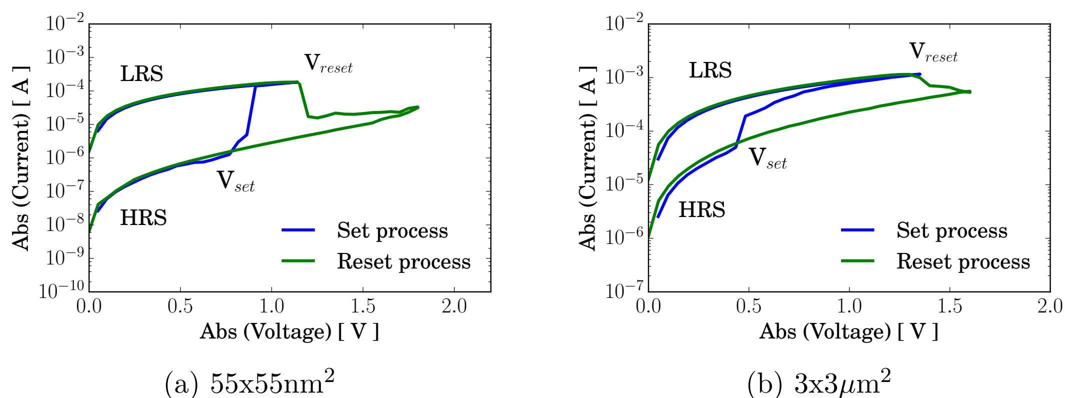

(a) 55x55nm^2 (b) 3x3μm^2

FIGURE 2.19. – Comparison of the I-V curves during set and reset processes for the HfO_2-based ReRAM device of (a) 55x55nm^2 and (b) 3x3μm^2.

As one can see, the conduction mechanisms matches during HRS and LRS independently of the bias polarity. However, while LRS has the same extension in both regions, HRS is larger under negative voltages. For this reason, we will analyse the Ohmic conduction under both voltage polarities and the TAT conduction only under negative voltages.

2.5.3.1. Ohmic conduction

Numerically, the value of G has been determined from the current- voltage experimental curves by the fitting of the linear relationship during LRS. The fitting was done following Ohm's Law :

$$I = GV \tag{2.1}$$

This process has been automated with a Python script that first, detects the region of LRS in the experimental data, and after, fits it with the linear function

of eq. 2.1. In Fig. 2.20, we present an example of this process for one sample of each type.

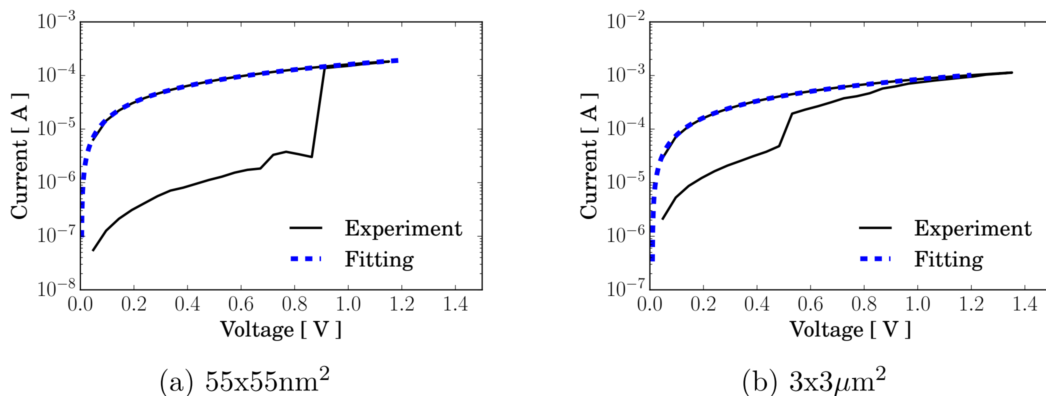

(a) 55x55nm^2

(b) 3x3μm^2

FIGURE 2.20. – Fitting of I-V curves by a function of the form $I = GV$ to obtain the value of the conductance G. The fitting is done in the region where the system is in low resistive state and follows ohmic conduction.

In experimental data (Fig. 2.8 and 2.9), the slope in the IV curves when the system is in LRS do not suffer a remarkable cycle to cycle variability. This behavior is proved by the small values of standard deviations of G are presented in table 2.2 for all samples.

	G [μS]	
Sample	V>0	V<0
55x55 nm^2	173.83 ± 3.86	195.28 ± 5.82
65x65 nm^2	177.16 ± 6.95	214.04 ± 5.40
75x75 nm^2	185.45 ± 6.67	212.99 ± 8.08
85x85 nm^2	181.37 ± 6.10	197.53 ± 6.90
105x105 nm^2	179.92 ± 6.87	193.72 ± 11.00
135x135 nm^2	157.81 ± 6.78	168.10 ± 9.19
1x1 μm^2	909.70 ± 70.58	943.14 ± 72.93
3x3 μm^2	979.27 ± 57.42	1024.66 ± 52.73
5x5 μm^2	993.44 ± 64.98	1051.92 ± 61.36

TABLE 2.2. – Conductance for set and reset processes

In the plot of the conductance as a function of the area A (see Fig. 2.21), one can observe one characteristic value for each group of samples. There is an abrupt jump of the conductance in μm-size samples that is around five times the conductance in the small ones. This difference could be related to the size of the CF.

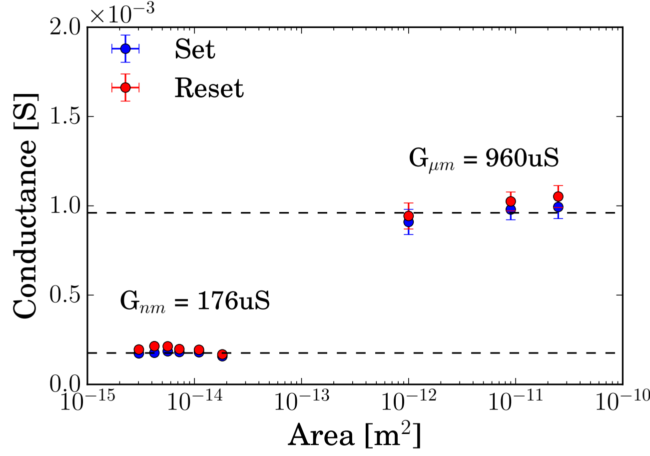

FIGURE 2.21. – Conductance for set and reset process as a function of area device.

It must be mention that the conductance under negative voltages is slightly bigger than those under positive voltages. This fact could be related to the effect of the electric field over the oxygen ions at the interface. Under positive bias the ions move to the Hafnium layer creating an interfacial oxide layer. Conversely, by applying negative bias, oxygen ions in the interfacial layer move back to the dielectric, which in turn causes conductance increases [112].

2.5.3.2. Trap assisted tunneling conduction (TAT)

In the I-V curves of Fig. 2.8 and 2.9, the HRS region shows the exponential dependency typical of TAT conduction. In this case, the current-voltage relationship could be given by the exponential function : $I = I_0 \exp[\alpha(\Delta V)]$, where I_0 and α are electrical parameters that must be determined. However, considering that HfO_2-based ReRAM are bipolar devices, a more suitable expression for the electrical conduction could be given by a hyperbolic sine function that include data under positive and negative voltages. Thus, the IV relationship could be given by :

$$I = I_0 \sinh[\alpha(\Delta V)] \tag{2.2}$$

TAT conduction is attributed to the tunneling currents assisted by defects in the dielectric. In ReRAM devices these defects, or traps, are mainly oxygen vacancies [113], that have been separated and randomly ubicated after reset process. Available traps will be close to the CF and its number might be limited by the initial condition of the CF. Although, the exact conduction mechanism in HRS state can be difficult to determine, one can infer that TAT is strongly dependent on the trap's distribution and the barrier energy that electrons must overcome.

The values of I_o and α have been determined from experimental data. A python script detects the HRS region and after, fits it with equation 2.2. This process is illustrated in Fig. 2.22.

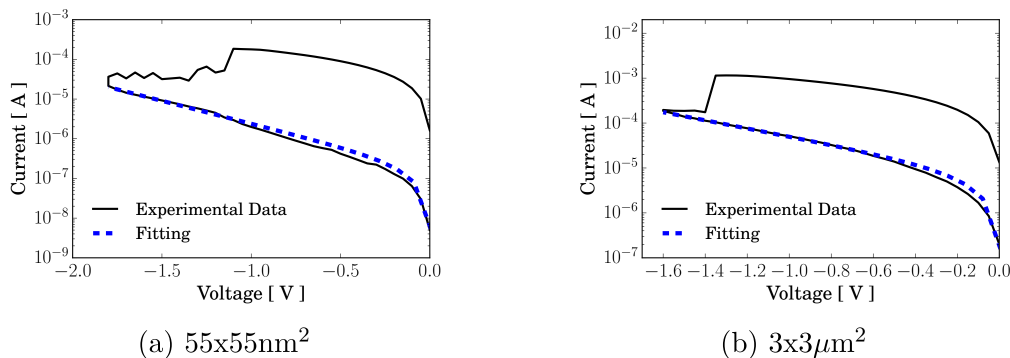

(a) 55x55nm^2 (b) 3x3μm^2

FIGURE 2.22. – Fitting of I-V curves under negative voltages by a function of the form $I = I_0 \sinh[\alpha(\Delta V)]$ to obtain I_0 and α. The fitting is done in the region where the system is in high resistive state and has tunneling conduction.

From the values of I_o and α determined after the fitting, three important characteristics will be analysed. First, the big distribution of data will be presented with histograms. Second, the variability of these two parameters, will be quantified with the relative standard deviation (RDS), and finally, we will use 2D histograms to show the relationship between I_o and α.

In figures 2.23 and 2.24, the histograms of these parameters are presented. Mean values and standard deviations have been included. Furhter, normal distribution has been plotted in those samples that are normally distributed after the normality test (see appendix C). The histograms of I_o show that most of the values are not evenly distributed around the center of the histogram. Only, three groups of data are normally distributed, while the others are skewness right. Also, one can note that I_o histograms are heavy tailed in nm-size samples, while they are light tailed in the big ones.

On the other hand, the behavior of the α histograms are different. Only, in nm-size samples the histograms are normally distributed, with a clear peak. Although, the mean values for all samples are similar.

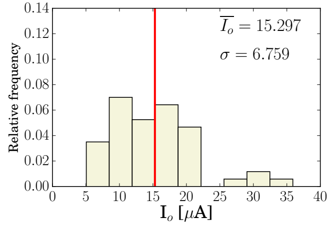

(a) 55x55nm^2

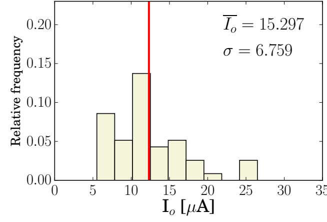

(b) 65x65nm^2

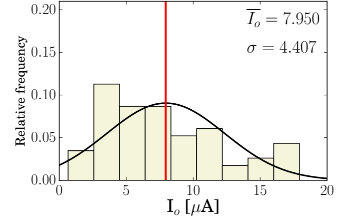

(c) 75x75nm^2

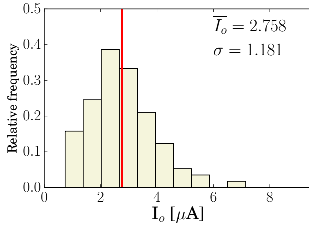

(d) 85x85nm^2

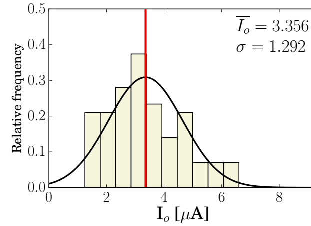

(e) 105x105nm^2

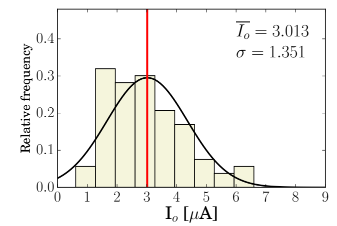

(f) 135x135nm^2

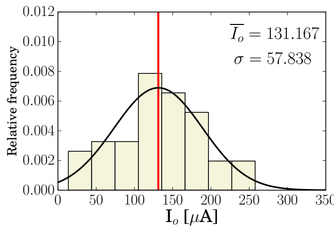

(g) 1x1μm^2

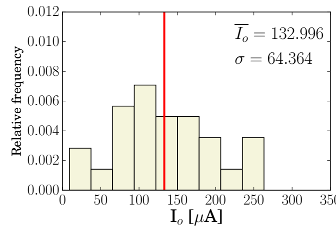

(h) 3x3μm^2

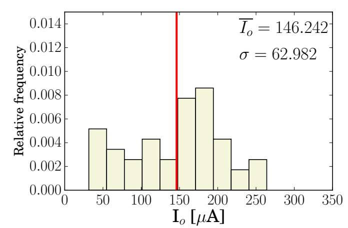

(i) 5x5μm^2

FIGURE 2.23. – Statistical distribution of I_o

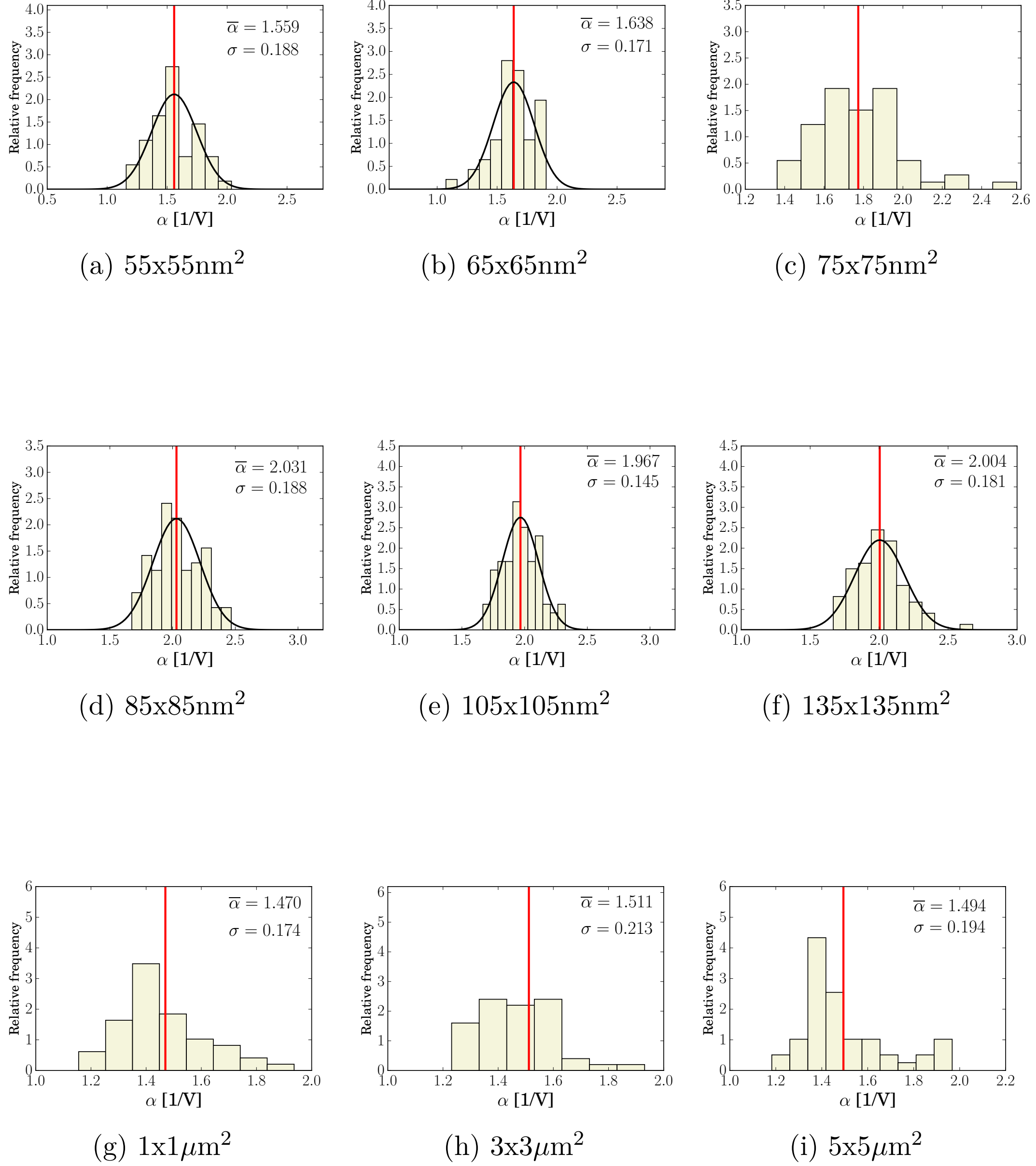

(a) 55x55nm^2 (b) 65x65nm^2 (c) 75x75nm^2

(d) 85x85nm^2 (e) 105x105nm^2 (f) 135x135nm^2

(g) 1x1μm^2 (h) 3x3μm^2 (i) 5x5μm^2

FIGURE 2.24. – Statistical distribution of α

The variability observed in the IV curves (Fig. 2.8 and 2.9), has been quantized by the relative standard deviation (RSD) that is a statistical measure of the dispersion of data around the mean (RDS=σ/μ). In table 2.3, mean values, standard deviations and RDS for I_o and α are presented. As one can see, RDS value is similar between all samples.

I_o, α and RDS as a function of the area are plotted in fig. 2.25 and 2.26. Surprisingly, although the values of I_o and α are different among the areas, the variability have the same behavior in all the samples (see Fig. 2.26).

	I_o [μA]		α [1/V]	
Sample	$\mu \pm \sigma$	$I_{o\ RDS}$ (%)	$\mu \pm \sigma$	$\alpha_{\ RDS}$ (%)
55x55 nm^2	15.297 ± 6.759	44.2	1.559 ± 0.188	12.1
65x65 nm^2	12.319 ± 4.820	39.1	1.638± 0.171	10.4
75x75 nm^2	7.950 ± 4.407	55.4	1.774 ± 0.221	12.5
85x85 nm^2	2.758 ± 1.181	42.8	2.031 ± 0.188	9.3
105x105 nm^2	3.356 ± 1.292	38.5	1.967 ± 0.145	7.4
135x135 nm^2	3.013 ± 1.351	44.8	2.004 ± 0.181	9.0
1x1 μm^2	131.167 ± 57.838	44.1	1.470 ± 0.174	11.8
3x3 μm^2	132.996 ± 64.364	48.4	1.511 ± 0.213	14.1
5x5 μm^2	146.242 ± 62.982	43.1	1.494 ± 0.194	13.0

TABLE 2.3. – Mean value and standard deviation of I_o and α determined by the fitting of IV curves when the system is in HRS with the function $I = I_0 \sinh[\alpha(V)]$

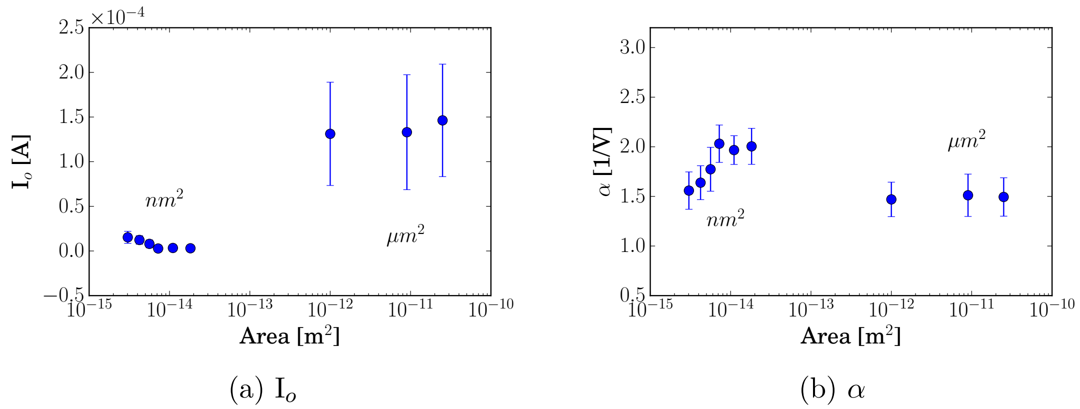

(a) I_o (b) α

FIGURE 2.25. – I_o and α as a function of area device

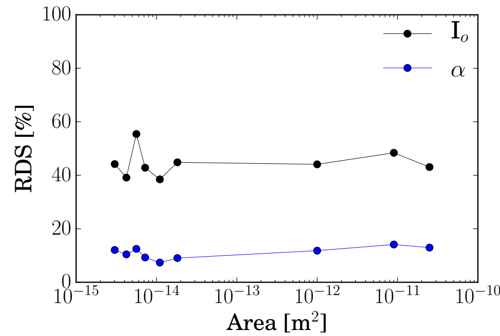

FIGURE 2.26. – Relative standard deviation (RDS) as a function of the area for I_o and α

Finally, to analyse the relationship between I_o and α, 2D histograms have been plotted and presented in Fig. 2.27. These two parameters are close related to each other and further, they show a similar behavior in all samples. With small α, big values of I_o are possible.

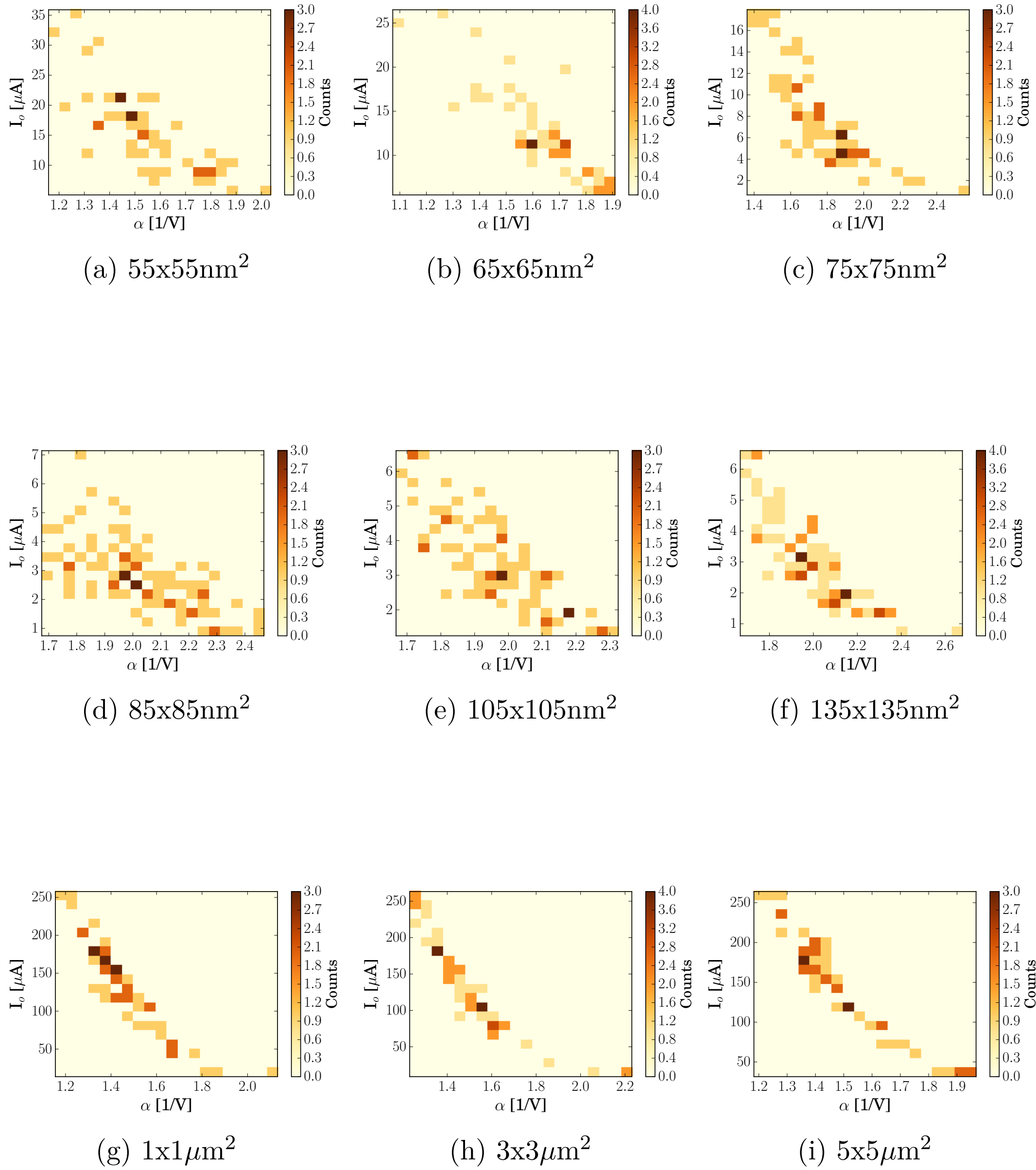

(a) 55x55nm^2 (b) 65x65nm^2 (c) 75x75nm^2

(d) 85x85nm^2 (e) 105x105nm^2 (f) 135x135nm^2

(g) 1x1μm^2 (h) 3x3μm^2 (i) 5x5μm^2

FIGURE 2.27. – Relationship between I_o and α through 2D histograms.

With the mean values presented in table 2.3 for nm-size samples, we plotted I_o versus α in Fig. 2.28. A clear exponential dependency is confirmed with this plot that has been fitted with a function of the form, $I_o = k_1 \exp(-k_2\alpha)$, where k_1 and k_2 are constants. After the fitting, we found for nm-size samples k_1=3.73mA and k_2=3.52V. This process was not possible with big samples due to the small number of points.

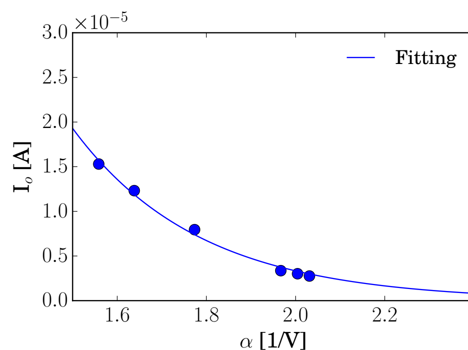

FIGURE 2.28. – I_o as a function of α for nm-size samples.

This behavior has been reported before in the quantum point contact model (QPC), explained in detail in appendix D.1. In this model during the HRS, these is a gap in the CF. At low applied voltages the current could be simplified by an exponential relationship between current and voltage [114]. Comparing with our result, the value of k_2 could represent the height of the potential barrier.

One can understand that the CF is partially destroyed during the HRS. Thus, the conduction is mainly leaded by the movement of electrons through oxygen vacancies that acts as traps. After reset switching, traps remain randomly located along the disconnected CF, with variable distances between them. This could explain the big variability observed in experimental data, that is a common feature of all ReRAM devices [10, 115]. Further, one can argue that the distances between traps and the potential height are changing between cycles and this cause the observed cycle to cycle variability.

However, it is important to mention that another cause of variability in HRS is the random telegraph noise (RTN), caused by the random capture and emission of charge carriers into or out of traps. This effect has been reported before in HfO_2-based ReRAM's [116] and it is more important in small devices because the device size is so small that trapping/de-trapping of one individual defect has greater impact on the device performance [117]. This topic will be the objective of a future work.

2.5.4. Different electrical response of the samples electroformed with I_c=5mA and I_c=10mA

In this section, the effect of two compliance current during electroforming is explored (see sec. 2.4). In Fig. 2.29, the IV curves of the samples electroformed with two values of I_c are presented. Mean values are identified in black for I_c=5mA and in blue for I_c=10mA. One can observe that the differences are more evident when the devices are in HRS, specially under negative voltages.

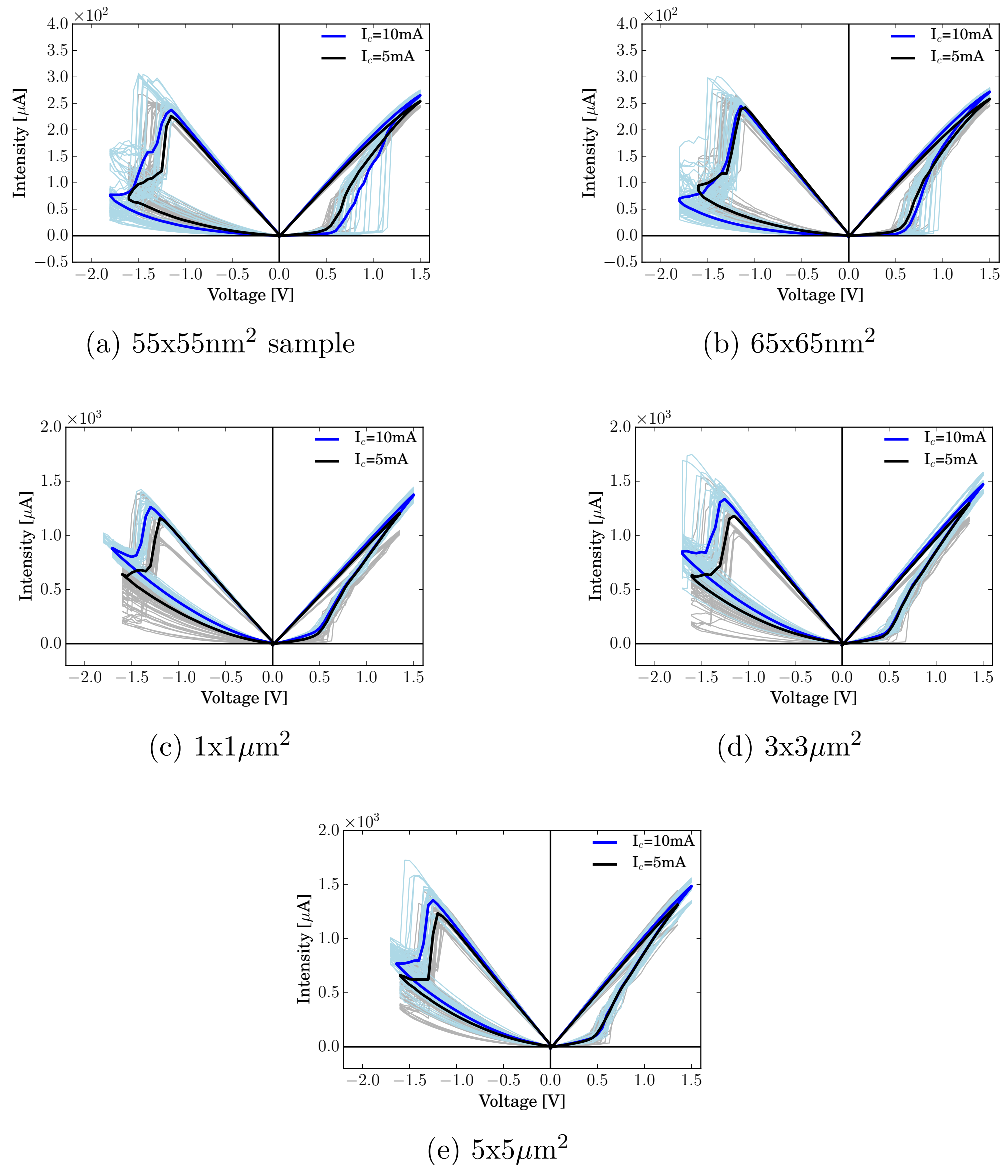

(a) 55x55nm^2 sample

(b) 65x65nm^2

(c) 1x1μm^2

(d) 3x3μm^2

(e) 5x5μm^2

FIGURE 2.29. – Current-voltage characteristics of HfO_2-based ReRAM devices electroformed with two values of compliance current, I_c=5mA in black and I_c=10mA in blue.

The switching parameters (V_{set}, V_{reset}, G, I_o and α) used to describe the resistive switching in the ReRAM devices were extracted from the experimental curves. V_{set} and V_{reset} as a function of the device area are plotted in Fig. 2.30. One can see that these values exhibit a slight change when the compliance current increases from 5mA to 10mA.

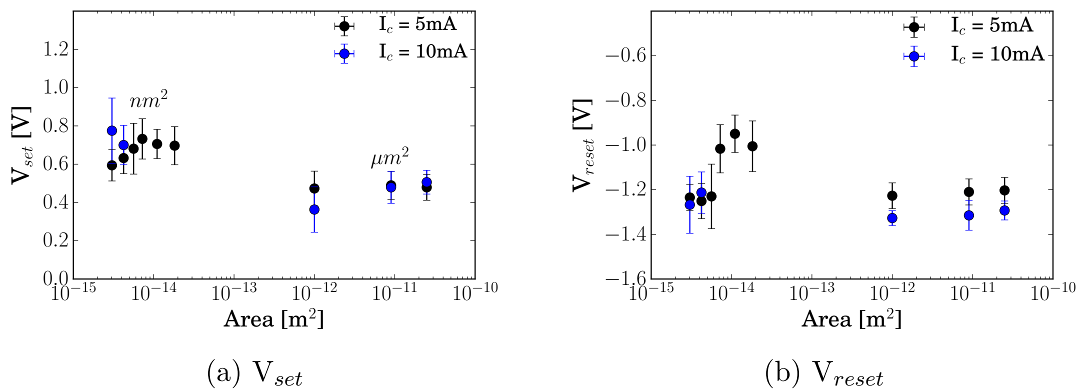

(a) V_{set} (b) V_{reset}

FIGURE 2.30. – V_{set} and V_{reset} as a function of the device area for samples electroformed with I_c=5mA in black and I_c=10mA in blue.

On the other hand, as one can see in Fig 2.29, the conduction mechanisms do not change between the two kind of samples. Trap assisted tunneling, described by eq. 2.2, is observed in HRS while ohmic conduction, described by eq. 2.1, is presented in LRS. After the fitting of the IV curves, the values of G, I_o and α were determined and they are plotted in figures 2.32 and 2.31.

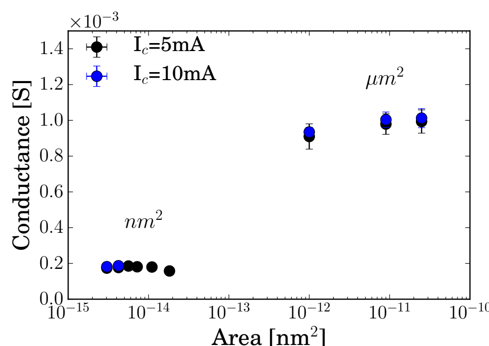

FIGURE 2.31. – Conductance G, used to describe ohmic conduction in LRS, as a function of the device area for samples electroformed with I_c=5mA in black and I_c=10mA in blue.

The main characteristic is that conductance is similar between the samples electroformed under two I_c. This result could imply that in LRS all devices have a complete CF of similar characteristic independently of the electroforming conditions. However, although in HRS the conduction mechanism can be described by

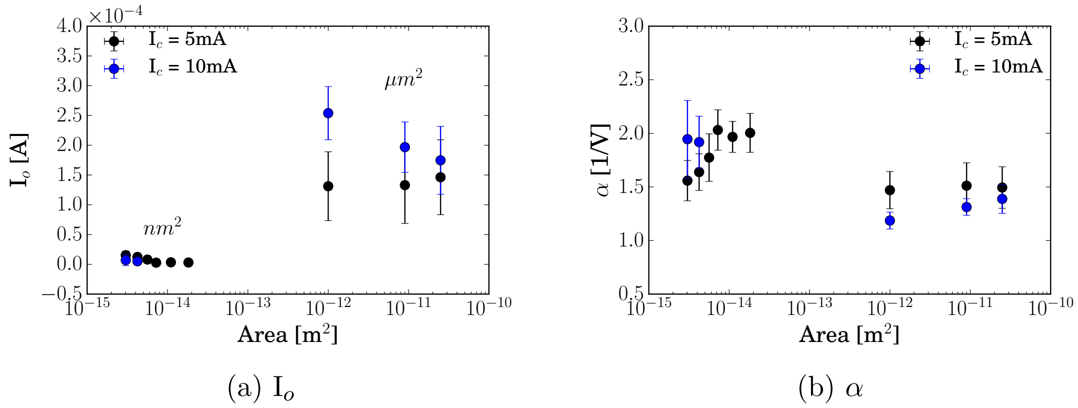

(a) I_o (b) α

FIGURE 2.32. – I_o and α, used to describe TAT conduction in HRS, as a function of the device area for samples electroformed with I_c=5mA in black and I_c=10mA in blue.

TAT, I_o and α values are clearly different among all samples. As a conclusion, the effect of compliance current during electroforming is more important in HRS.

2.6. Stochastic Nature of ReRAM

The stochastic behavior of HfO_2-based ReRAM's has been studied in this chapter through the analysis of the electrical parameters involved in electroforming and resistive switching. During the electroforming, the CF is formed by a soft dielectric breakdown in the dielectric due to the oxygen vacancies segregation towards the HfO_2-grain boundaries. This process is governed by random and uncontrolled events that causes device variability, even though the devices would have the same physical characteristics after fabrication. As a result, there is not guarantee that all CFs are located at the same place and had the same behavior, even within devices of the same area. This causes the electrical variability observed during electroforming, studied in section 2.4.

The stochastic nature of the CF's affects the electrical response during set and reset processes and generates fluctuations in the IV curves. In this way, all parameters involved in the switching, V_{set}, V_{reset}, G, I_o and α, were analysed statistically in this chapter. This analysis allows us to determine, not only the distribution of the data but also the mean values (μ) and the standard deviations (σ) of each data set.

Two conduction mechanisms have been proposed in these ReRAM devices. In LRS, the system has Ohmic conduction due to the metallic nature of the CFs created by the continuous distribution of oxygen vacancies. As a result, the electrical variability in this state is not important (see sec.2.5.3.1). On the other hand, during HRS the main mechanism is by trap assisted tunneling conduction.

In this state the electrical conduction is possible thanks to traps, mainly oxygen vacancies, that are randomly distributed along the CF. This causes the variability observed in section 2.5.3.2. The conduction has been described with two parameter, I_o and α, that could depend on energy barrier height ϕ and average distance between traps (a).

The results of the electrical analysis reported in this chapter will be used to build a phenomenological model in the next chapter.

3. Phenomenological model for resistive switching of bipolar ReRAM devices

Summary

3.1 One-Chain model 69
3.1.1 Switching probability 70
3.1.2 Set and reset switching simulation 71
3.2 N-Chain model 73
3.3 Conduction mechanisms in the model 74
3.4 Model implementation 75
3.5 Model calibration 79
3.6 Simulation results and discussion 81

Several models, with different approaches and degrees of accuracy, have been developed to explain the resistive switching of ReRAM devices. These models are mainly divided in three levels : microscopic, macroscopic and compact models [118], whose main characteristics are detailed in appendix D. Inside the group of compact models, the filamentary conduction, accepted for most of binary oxide-based ReRAM, is usually explained with a 1-D filament simplification. Some of them propose that the resistance switching is due to the tunneling gap growth [119–121], while others explain it with the change of the filament diameter during switching [122, 123].

In this chapter, a phenomenological model for resistive switching of bipolar devices is presented. It has been developed based on the experimental evidence found in chapter 2 for HfO_2-based ReRAM. It assumes that the electric field affects mainly a localized region of the conductive filament, that in the following will be called "active region". This region is represented by a network of parallel circuit breakers that can change the state according with a switching probability. This approach has been proposed considering the stochastic nature of the resistive switching. This model has been fully implemented in Python, which makes it flexible and easily modifiable to analyze the resistive switching in other devices, even with other kinds of conduction mechanisms.

3.1. One-Chain model

In the one-chain model, the active region is represented with one vertical chain composed of three electrical elements. Those connected with the region of the filament that does not suffer any significative change during switching are always low resistive (LR), meanwhile the middle element acts as a "resistive breaker" and can be low or high resistive (HR) (see Fig. 3.1). The change of state is directly related to the applied external voltage (V_{ext}), that can connect or disconnect the breaker due to the potential difference that produce on it. The ReRAM device will be in low resistive state (LRS) when all elements are LR. Otherwise, if the breaker is high resistive (HR), the entire ReRAM will be in high resistive state (HRS).

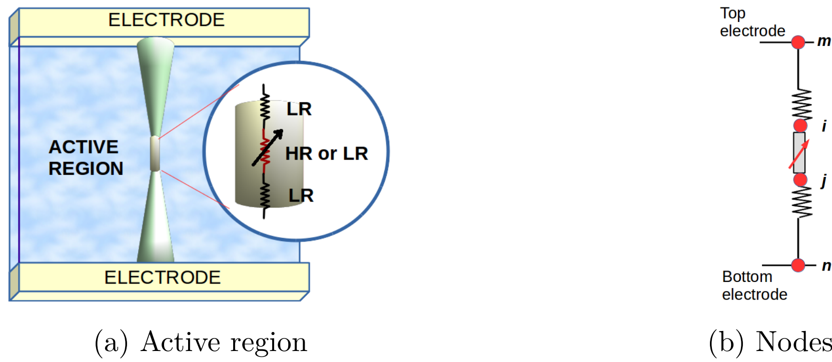

(a) Active region (b) Nodes

FIGURE 3.1. – One-chain model : schematic representation of the active region inside the conductive filament. This is represented by one chain with three electrical elements with low resistance (LR) or high resistance (HR)

We work only with vertical connections based on the fact that the electric field modifies the energy barrier in one direction and allows the vertical migration of charges species, especially oxygen ions and vacancies [124]. The stochastic nature of filamentary conduction has been included in the model through a switching probability P_s that controls the change of breaker's state and depends on the voltage drop along it (V_{link}=V_i-V_j). In the model, for each V_{ext} applied, the values of V_{link} and current I are computed by solving Kirchhoff's equation at each node.

$$I_i = I_{i-j} + I_{i-m} = 0 \qquad (3.1)$$

The current I_{i-j} depends on the conduction mechanism of the chain. For the moment, we consider that the dominant mechanism is Ohmic for HRS and LRS, with two different values of conductance, as it has been proposed in [83]. Thus, conduction will be modeled by :

$$I_{ij} = G_{ij}(V_i - V_j) \tag{3.2}$$

where i and j are the nodes of the chain (see Fig. 3.1b). Electrical elements that are LR have always high conductance, G_H, while the breaker, G_B, could have two values, G_H or G_L, for high or low conductance. The system of linear equations for this one-chain model is given by 3.3, and has been solved in Python by using sparse matrix resolution method.

$$\begin{bmatrix} -1 & -G_H & 0 \\ 0 & G_H + G_B & -G_B \\ 0 & -G_B & G_B + G_H \end{bmatrix} \begin{bmatrix} -I \\ V_j \\ V_i \end{bmatrix} = \begin{bmatrix} -G_H * V_n \\ G_H * V_n \\ G_H * V_m \end{bmatrix} \tag{3.3}$$

As in the experimental setup, the bottom electrode is grounded, so V_n=0.

3.1.1. Switching probability

Physically, set and reset processes are caused by the stochastic movement of oxygen vacancies under the influence of the applied external voltage. This fact could be one of the reasons for the statistical fluctuation during cycles observed in the IV curves of figures 2.8 and 2.9. To reproduce this behavior, a switching probability, P_s, has been included in the model. A suitable mathematical expression for P_s could be a sigmoid function [125], given by eq. 3.4. This function ensures that the probability values falls between 0 and 1, for any value of external voltage.

$$P_S = \frac{1}{2}\left\{1 + \tanh\left[C_s\left(V_{link} - V_{ref}\right)\right]\right\} \tag{3.4}$$

V_{ref} and C_s are two parameters that need to be determined for set and reset processes independently. V_{ref} is set voltage (V_{set}) or reset voltage (V_{reset}), according with the process, and its value can be determined from experimental data. On the other hand, C_s is the slope of the probability function and changes the direction and the steepness of the function. For set process the slope will be positive and open to the right, and for reset will be negative and open to the left, as it is shown in Fig. 3.2. In the model, the probability of set switching is represented as P_{set}, while the probability of reset is P_{reset}.

Once the switching probability has been calculated, its value is compared with a computer-generated random number p. Only if P_s is bigger than p, the breaker's state changes, otherwise the state is the same and V_{ext} is increased. The p number has been generated in Python, with the function **random()** [126]. The function

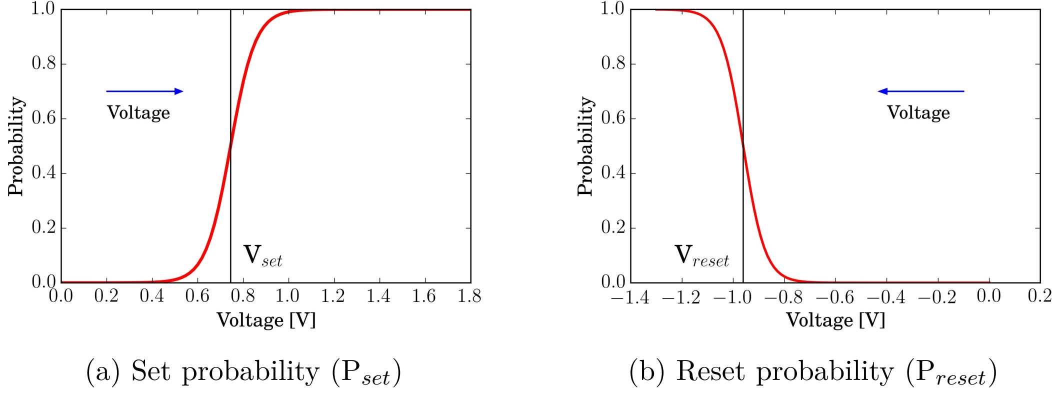

(a) Set probability (P_{set})

(b) Reset probability (P_{reset})

FIGURE 3.2. – Switching probability P_s of set and reset processes.

random() works with the Mersenne Twister as core the generator [127].

3.1.2. Set and reset switching simulation

In computer simulation, for set process initially the breaker is HR and the external voltage (V_{ext}) is applied. Then, the current (I) through the chain and the voltage at each node (V_i) are computed. If the current is smaller than the compliance current (I_{comp}), the voltage drops across the breaker (V_{link}) is calculated. After, the set probability (P_{set}) is computed and the random number (p) is generated. Only if P_{set} is bigger than p, the breaker state change to LR. Otherwise, the V_{ext} is increased and the process is repeated. Once all elements in the chain are LR, the ReRAM is in LRS. This process is illustrated in the flowchart of Fig. 3.3a.

For reset process, at the beginning the breaker is LR and negative voltage is applied over the system. For computer simulation the steps are presented in flowchart of Fig. 3.3b. It must be noted that the compliance current, I_{comp}, has been included in both, set and reset process, such as occurs in real systems to prevent high dielectric breakdown of the device.

The I-V simulation of this one-chain model after 5 cycles is presented in Fig. 3.4a, while the I-V experimental response of a bipolar HfO_2-based ReRAM of 85x85nm^2 is in Fig. 3.4b. By comparison, the model can simulate set and reset transition with certain degree of variability.

However, two important facts must be considered. First, in experimental curves set and reset transitions are gradual processes, and second, the conduction mechanism observed in experimental data when the system is in HRS is better represented by trap assisted tunneling conduction (TAT). These two characteristics will be included in the next two sections.

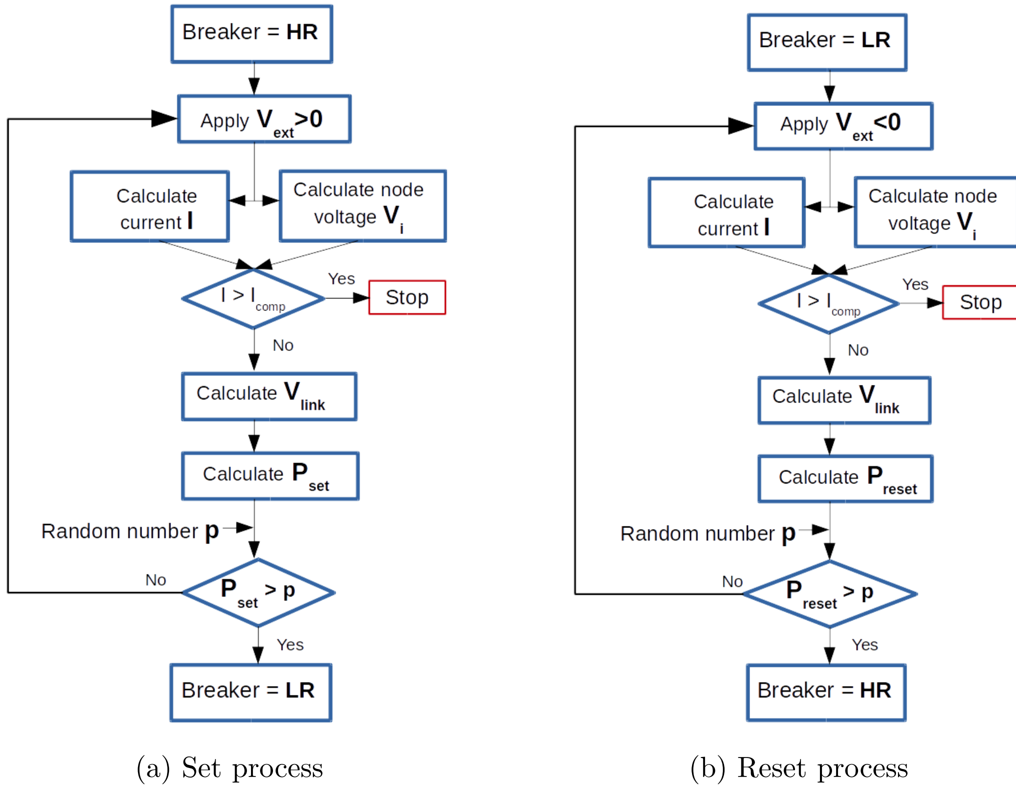

(a) Set process (b) Reset process

FIGURE 3.3. – Flowchart for set and reset processes used in computer simulation.

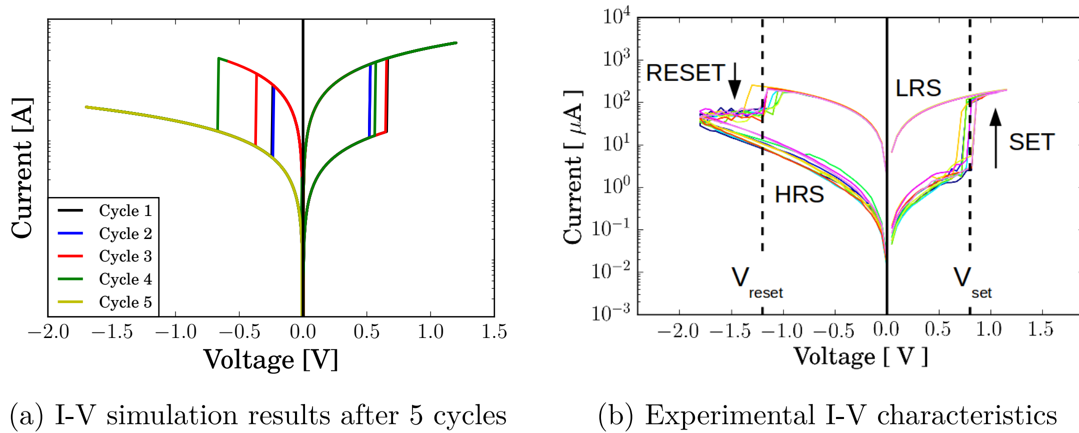

(a) I-V simulation results after 5 cycles (b) Experimental I-V characteristics

FIGURE 3.4. – (a) Simulation result of a bipolar ReRAM-device modeled with an active region composed of one vertical chain and (b) Experimental I-V response of a bipolar HfO_2-based ReRAM of 85x85nm^2.

3.2. N-Chain model

In experimental data, several intermediate jumps in the transitions from HRS to LRS (or from LRS to HRS) have been identified. For instance, two cycles in linear scale are presented in Fig. 3.5.

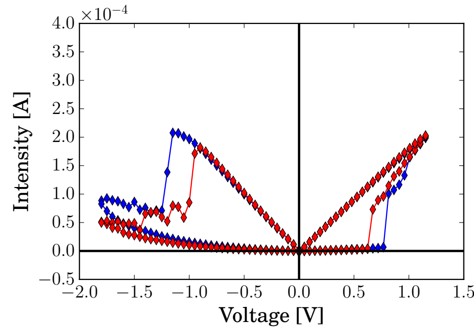

FIGURE 3.5. – I-V characteristics of the HfO_2-based ReRAM of $85x85nm^2$ where some jumps in set and reset switching can be identified.

The gradually switching process observed in experimental data can be reproduced by the model when the active region is represented with some vertical chains instead of one. Thus, set and reset transitions will be the result of the gradual activation (or deactivation) of the breakers. A schema of a 4-chain model is presented in figure 3.6.

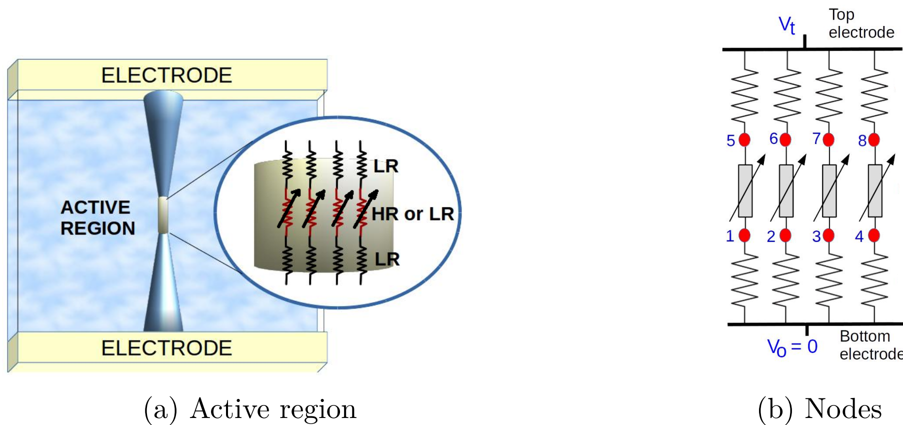

(a) Active region (b) Nodes

FIGURE 3.6. – Scheme of the active region composed by four chains, each one with of three elements with low resistance (LR) or high resistance (HR)

In this N-chain model, the switching process occurs when all breakers in the active region change its state. As in the case of the 1-chain model, the electrical potentials at each point (V_i) are determined by solving Kirchhoff's equations. For the moment, all electrical elements obey Ohm's law, with two values of conduc-

tance, G_H or G_L, for HRS and LRS respectively. The systems of linear equations for the 4-chain model of figure 3.6 is presented in 3.5

$$\begin{bmatrix} 1 & -G_H & -G_H & -G_H & -G_H & 0 & 0 & 0 & 0 \\ 0 & G_H+G_B & 0 & 0 & 0 & -G_H & 0 & 0 & 0 \\ 0 & 0 & G_H+G_B & 0 & 0 & 0 & -G_H & 0 & 0 \\ 0 & 0 & 0 & G_H+G_B & 0 & 0 & 0 & -G_H & 0 \\ 0 & 0 & 0 & 0 & G_H+G_B & 0 & 0 & 0 & -G_H \\ 0 & -G_H & 0 & 0 & 0 & G_H+G_B & 0 & 0 & 0 \\ 0 & 0 & -G_H & 0 & 0 & 0 & G_H+G_B & 0 & 0 \\ 0 & 0 & 0 & -G_H & 0 & 0 & 0 & G_H+G_B & 0 \\ 0 & 0 & 0 & 0 & -G_H & 0 & 0 & 0 & G_H+G_B \end{bmatrix} \begin{bmatrix} -I \\ V_1 \\ V_2 \\ V_3 \\ V_4 \\ V_5 \\ V_6 \\ V_7 \\ V_8 \end{bmatrix} = \begin{bmatrix} 0 \\ 0 \\ 0 \\ 0 \\ 0 \\ G_H V_t \\ G_H V_t \\ G_H V_t \\ G_H V_t \end{bmatrix} \tag{3.5}$$

In computer simulation, for set process initially all breakers are HR and the simulation follows the steps presented flowchart of Fig. 3.3a. The system changes to LRS when all breakers are LR. Meanwhile, for reset process initially all breakers are LR and the simulation follows the sequence presented in flowchart of Fig. 3.3b. The system will be HRS when all breakers have been deactivated.

The simulation of the IV response for a model of four chains in the active region is presented in figure 3.5. At this point, it is possible to observe the cycle to cycle variability and the gradual switching simulated by the model.

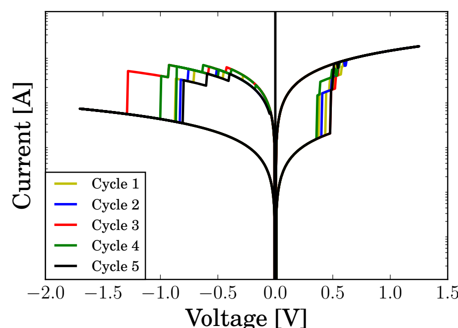

FIGURE 3.7. – I-V simulation results of 5 cycles of a bipolar ReRAM device modeled with an active region composed of four vertical chains

3.3. Conduction mechanisms in the model

Experimental results for ReRAM devices show an exponential dependency in the current-voltage characteristics when the system is in HRS (see Fig. 3.8). This relationship is typical of some kind of tunneling mechanism : trap-assisted tunneling (TAT), Poole–Frenkel emission, Fowler–Northeim tunneling or direct tunneling [25], that have been explained in section 1.3.3. However, the most accepted mechanism for HRS in HfO_2-based devices is TAT [45, 50, 128].

In the model, to reproduce this voltage-current relationship in HRS, the expression for this non lineal-conduction could be given by $I_{i,j} = I_0 \exp[\alpha(V_i - V_j))]$,

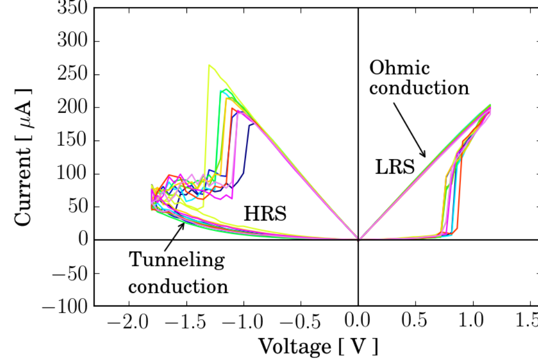

FIGURE 3.8. – I-V experimental data. Linear relationship in LRS shows an ohmic conduction while the exponential dependency in HRS implies a tunneling mechanism.

where I_0 and α are fitting parameters determined from experimental data. However, for bipolar switching it is necessary to include the electrical response under positive and negative voltages at the same time. In this case, an accurate equation for the electrical conduction should include a hyperbolic sine function (sinh). Thus, in HRS the conduction is given by :

$$I_{i,j} = I_0 \sinh\left[\alpha(V_i - V_j))\right] \tag{3.6}$$

Now, Kirchhoff's equations at each node must be rewritten according with the state of the breaker. It means that current at node i is a combination of Ohmic and TAT conduction if the breaker is HR, while it is a sum of two ohmic conduction contributions if the breaker is LR. Thus, the current for the node i will be given by 3.7 if the breaker is HR and by 3.8 if it is LR.

$$I_i = \sigma_{im}(V_i - V_m) + I_0 \sinh(\alpha(V_i - V_j))) \tag{3.7}$$

$$I_i = \sigma_{im}(V_i - V_m) + \sigma_{ij}(V_i - V_j) \tag{3.8}$$

In the N-chain model with two conduction mechanisms, Kirchhoff's equations result in a system of nonlinear equations that will be solved by the Newton-Raphson method [129].

3.4. Model implementation

This model has been implemented in Python to automates its execution. The simulation follows the procedure presented in flowcharts 3.3a and 3.3b for set and reset process, respectively.

Initially, for script execution the user must introduce some initial parameters :

1. Size of active region. The number of vertical chains (N_x), with three elements each one (N_z=3).
2. Set and reset voltages (V_{set} and V_{reset}).
3. The parameters to calibrate Ohmic and TAT conduction (G, I_o and α) given by eq. 3.2 and 3.6.
4. Voltage sweep information : maximum voltage values and voltage step value.

These data give the script the information required to build the active region. The script computes the number of nodes k_s, k_s=N_xx(N_z+1), that is equal to the number of equations to be solved. For instance, in Fig. 3.9 the active region of five chains (N_x=5) is presented. This size of active region will be used throughout this section.

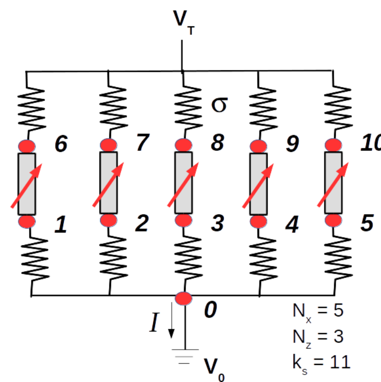

FIGURE 3.9. – Scheme of the active region composed by five chains

Then, the script is ready to run simulation. It enters in a loop that set the external voltage and follow the steps of flowchart 3.3. The code computes current (I), node voltages (V_i), switching probability (P_s), and determines the change of breaker's state. One section of this code is presented in Fig. 3.10 as example.

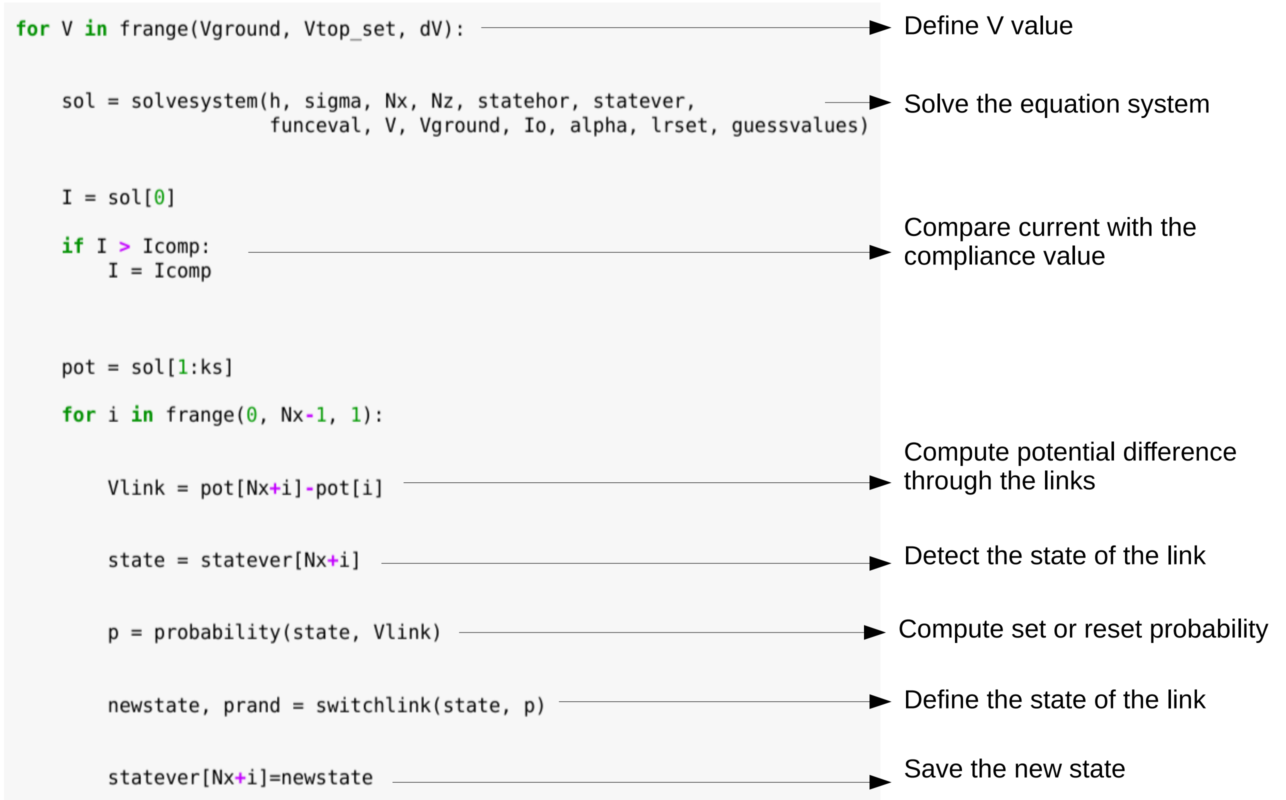

FIGURE 3.10. – Section of the Python script used for resistive switching simulation.

Three important functions have been written to optimize the model

1. **solvesystem** function solves Kirchhoff's equations.
2. **probability(state, Vlink)** function calculates the switching probability.
3. **switchlink(state, p)** function determine the breaker's state.

In our model, the system of k_n non-linear equations will be solved by Newton Raphson method. This is a powerful technique for solving equations numerically [130] that works with an iterative root-finding procedure based on the linear approximation. Providing an initial guess x_o to $f(x) = 0$, the method iterate $x_{n+1} = x_n - \frac{f(x_n)}{f'(x_n)}$ until the function converges to a solution, when $f(x) \approx 0$.

In the model, the multidimensional Newton-Raphson method, given by eq. 3.9, will be applied.

$$\vec{X} = \vec{X}_o - [f'(\vec{X}_o)]^{-1} f(\vec{X}_o) \tag{3.9}$$

where $\vec{X}_o$ is the vector of initial guess values, $[f'(\vec{X}_o)]^{-1}$ is the inverse of Jacobian matrix evaluated at $\vec{X}_o$ and $f(\vec{X}_o)$ is the vector of evaluated functions.

For the 5-chain model of Fig. 3.9, the system of nonlinear equation is given by 3.1 and the Jacobian matrix is given by 3.10 :

Node	**Equation**
0	$f_0 = I + \sigma(V_0 - V_1) + \sigma(V_0 - V_2) + \sigma(V_0 - V_3) + \sigma(V_0 - V_4) + \sigma(V_0 - V_5)$
1	$f_1 = \sigma(V_1 - V_0) + I_o \sinh[\alpha(V_1 - V_6)]$
2	$f_2 = \sigma(V_2 - V_0) + I_o \sinh[\alpha(V_2 - V_7)]$
3	$f_3 = \sigma(V_3 - V_0) + I_o \sinh[\alpha(V_3 - V_8)]$
4	$f_4 = \sigma(V_4 - V_0) + I_o \sinh[\alpha(V_4 - V_9)]$
5	$f_5 = \sigma(V_5 - V_0) + I_o \sinh[\alpha(V_5 - V_{10})]$
6	$f_6 = I_o \sinh[\alpha(V_6 - V_1)] + \sigma(V_6 - V_T)$
7	$f_7 = I_o \sinh[\alpha(V_7 - V_2)] + \sigma(V_7 - V_T)$
8	$f_8 = I_o \sinh[\alpha(V_8 - V_3)] + \sigma(V_8 - V_T)$
9	$f_9 = I_o \sinh[\alpha(V_9 - V_4)] + \sigma(V_9 - V_T)$
10	$f_{10} = I_o \sinh[\alpha(V_{10} - V_5)] + \sigma(V_{10} - V_T)$

TABLE 3.1. – Kirchhoff's equations for the 5-chain model (Fig. 3.9) when all breakers are HR.

$$
\begin{bmatrix}
\frac{\partial f_0}{\partial I} & \frac{\partial f_0}{\partial V_1} & \frac{\partial f_0}{\partial V_2} & \frac{\partial f_0}{\partial V_3} & \frac{\partial f_0}{\partial V_4} & \frac{\partial f_0}{\partial V_5} & 0 & 0 & 0 & 0 & 0 \\
0 & \frac{\partial f_1}{\partial V_1} & 0 & 0 & 0 & 0 & \frac{\partial f_1}{\partial V_6} & 0 & 0 & 0 & 0 \\
0 & 0 & \frac{\partial f_2}{\partial V_2} & 0 & 0 & 0 & 0 & \frac{\partial f_2}{\partial V_7} & 0 & 0 & 0 \\
0 & 0 & 0 & \frac{\partial f_3}{\partial V_3} & 0 & 0 & 0 & 0 & \frac{\partial f_3}{\partial V_8} & 0 & 0 \\
0 & 0 & 0 & 0 & \frac{\partial f_4}{\partial V_4} & 0 & 0 & 0 & 0 & \frac{\partial f_4}{\partial V_9} & 0 \\
0 & 0 & 0 & 0 & 0 & \frac{\partial f_5}{\partial V_5} & 0 & 0 & 0 & 0 & \frac{\partial f_5}{\partial V_{10}} \\
0 & \frac{\partial f_6}{\partial V_1} & 0 & 0 & 0 & 0 & \frac{\partial f_6}{\partial V_6} & 0 & 0 & 0 & 0 \\
0 & 0 & \frac{\partial f_7}{\partial V_2} & 0 & 0 & 0 & 0 & \frac{\partial f_7}{\partial V_7} & 0 & 0 & 0 \\
0 & 0 & 0 & \frac{\partial f_8}{\partial V_3} & 0 & 0 & 0 & 0 & \frac{\partial f_8}{\partial V_8} & 0 & 0 \\
0 & 0 & 0 & 0 & \frac{\partial f_9}{\partial V_4} & 0 & 0 & 0 & 0 & \frac{\partial f_9}{\partial V_9} & 0 \\
0 & 0 & 0 & 0 & 0 & \frac{\partial f_{10}}{\partial V_5} & 0 & 0 & 0 & 0 & \frac{\partial f_{10}}{\partial V_{10}}
\end{bmatrix} \tag{3.10}
$$

After solving eq. 3.9, the values of current I and node voltages V_i are determined. If I is smaller than the compliance current (I_{comp}), the code continues and computes the potential difference through the links (V_{link}). Then, **probability(state, Vlink)** function computes switching probability, P_s, according with breaker's state and V_{link}. Finally, P_s is compared with a random number p in **switchlink(state, p)** function to define the change of breaker's state. This process is repeated for every voltage value, and for set and reset region.

3.5. Model calibration

For model calibration, seven parameters are required : V_{set}, V_{reset}, G, I_o, α, C_{set} and C_{reset}. In this work, the simulation has been calibrated for the Hf-based ReRAM studied in chapter 2 and according to the results of the electrical characterization. The devices have nine different areas : 55x55nm^2, 65x65nm^2, 75x75nm^2, 85x85nm^2, 105x105nm^2, 135x135nm^2, 1x1μm^2, 3x3μm^2 and 5x5μm^2. For calibration, they have been divided in two groups, nm-size and μm-size devices, due to the differences found in the electrical response.

The parameters used for simulations are presented in table 3.2. V_{set} and V_{reset} were obtained in section 2.5.1, while G correspond to the effective conductance obtained in section 2.5.3.1.

Parameter	nm-size samples	μm-size samples
V_{set} [V]	0.673	0.480
V_{reset} [V]	-1.117	-1.117
G [μS]	175.56	904.34
I_0 [A]	I_0= 2.42x10^{-23}A$^{-1.2}$	I_0= 3^{-4}A$^{0.03}$
α [1/V]	α = 0.27A+10.26	α = 0.009A+1.74
C_{set} [1/V]	10.77	13.19
C_{reset} [1/V]	12.20	12.20

TABLE 3.2. – Parameters used to calibrate the model.

However, to calibrate TAT conduction (eq. 3.6) we have considered the relationship of I_o and α with the device area A, identified in experimental data. In Fig. 3.11 the fitting for nm-size samples is presented, although the same process has been applied to μm-size samples.

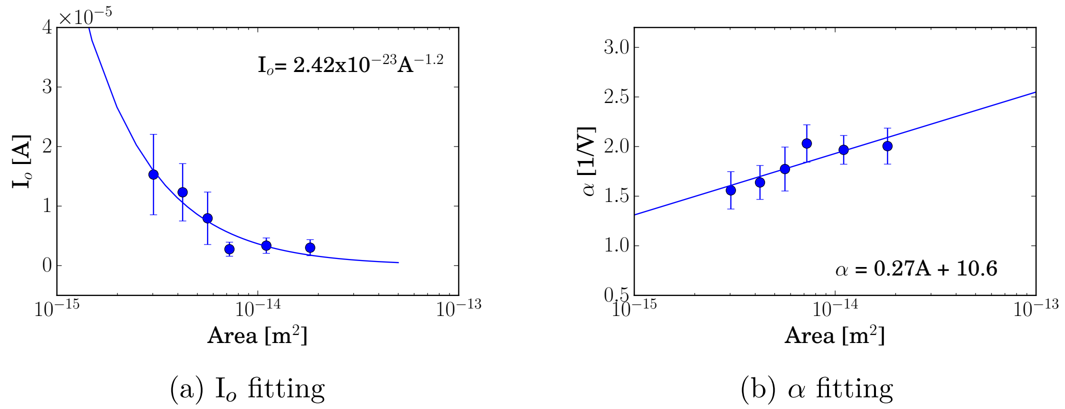

(a) I_o fitting

(b) α fitting

FIGURE 3.11. – I_o and α as a function of the area for HfO_2-based ReRAM of nm-size, along with the fitting used to calibrate the model.

A linear relationship between α and the area A has been determined for both types of samples. Meanwhile, the relationship between I_o and A can be described by a potential function. Further, the variability observed in experimental data has been included in the model according with the result presented in Fig. 2.26. It was found that the relative standard deviation (RSD), that is a statistical measure of the dispersion of data around the mean (RDS=σ/μ), has the same behavior in all samples. It means, RDS for I_o=40% and RDS of α=10%.

Finally, to calibrate the probability function, given by eq. 3.4, the value of C_s is required. C_s corresponds to the steepness of the probability function and determines how wide is the range of voltage values where the breaker can change its state. After the statistical analysis of V_{set} and V_{reset}, we realized that the cumulative distribution function of these data matches with the shape of our proposed

switching probability when $C_s = \frac{1}{\sigma_{V_{ref}}}$. This feature is presented in Fig. 3.12. Thus, to calibrate the model the values of C_s has been determined by the standard deviation of set and reset voltages.

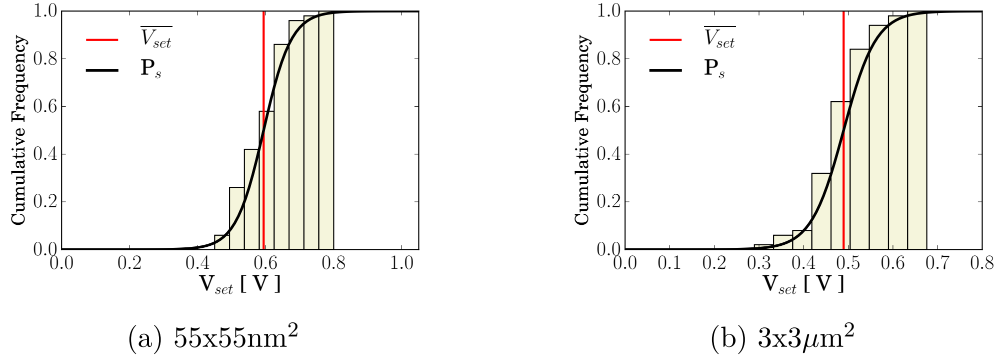

(a) 55x55nm^2 (b) 3x3μm^2

FIGURE 3.12. – Cumulative distribution of set voltage (V_{set}) along with the probability function.

3.6. Simulation results and discussion

Before displaying simulation results, the relationship between the real systems and the active region is presented. It is important to note that the studied samples have a bilayer structure HfO_2/Hf that allow the formation of a sub-stoichiometric region at the interface that acts as an oxygen reservoir for the resistive switching [96]. The active region of the model, where the breakers can be connected or disconnected would represent this region of the cell, where the movement of oxygen vacancies induces the partial creation or destruction of the CF (see Fig. 3.13).

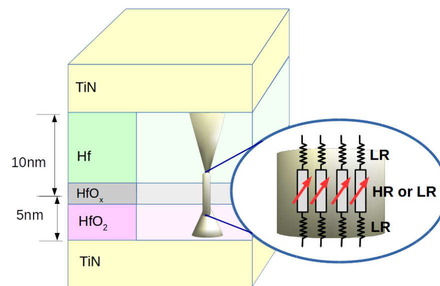

FIGURE 3.13. – Relationship between active region of the model and the sub-stoichiometric region the TiN/HfO_2/Hf/TiN ReRAM devices.

We propose that the active region is the narrowest zone of the CF, such as

it has been proposed before in the "Hour glass" model [96] or in the quantum point contact model [84, 97, 131]. However, our approach is different because we propose a switching probability leaded by the electric field to control the change of ReRAM's state.

Now, in order to verify the accuracy of the model, we combined experimental data and simulation results (50 cycles) in figure 3.14 for all samples. Grey lines correspond to the model with the mean value in black, while light blue lines correspond to experimetal curves with the mean value in blue. The model has been calibrated according with the information provided in table 3.2.

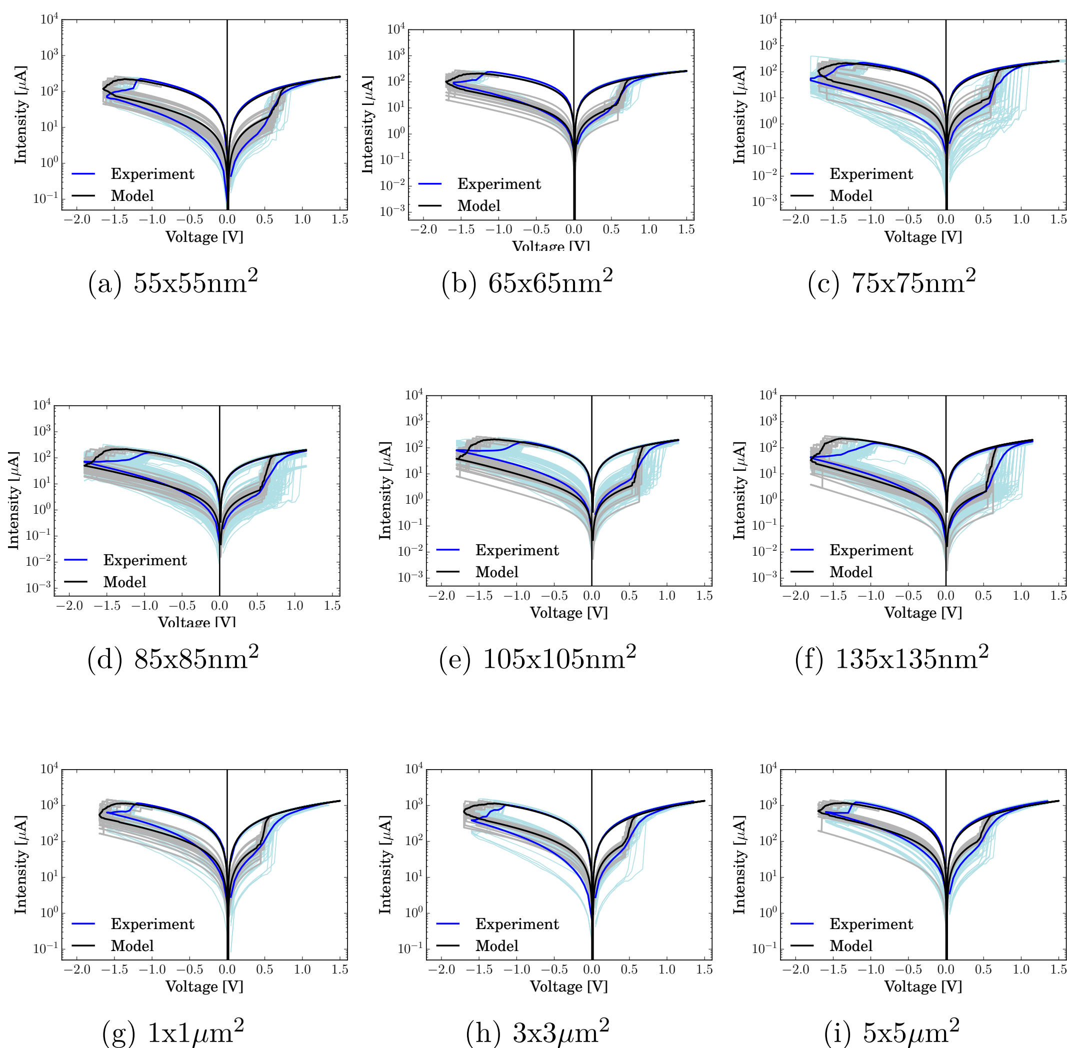

(a) 55x55nm^2 (b) 65x65nm^2 (c) 75x75nm^2

(d) 85x85nm^2 (e) 105x105nm^2 (f) 135x135nm^2

(g) 1x1μm^2 (h) 3x3μm^2 (i) 5x5μm^2

FIGURE 3.14. – Model and experimental current–voltage response of HfO_2ReRAM devices. Grey lines correspond to the model and light blue lines correspond to experimetal curves.

Simulation results confirm that the model can reproduce the switching beha-

vior of bipolar devices with only few parameters. The simulations also confirm that set and reset transitions are due to the microscopic connection or disconnection of the conductive paths created in the insulator after electroforming. The gradual set (or reset) process has been suitably reproduced in the model by an active region of some chains.

On the other hand, the stochastic nature of the switching has been obtained by a switching probability. A stochastic process is usually defined as a collection of random variables, that in the case of resistive switching are the position, number and distribution of charges species, oxygen vacancies or ions. All of them are changing cycle to cycle, and they are difficult to control during the process. The switching probability for ReRAM commutation has been proposed before in Kinetic Monte Carlo simulation [132]. However, at the level of circuit simulation the switching probability to control the change of state in ReRAM devices is considered for first time.

We can conclude that this model is efficient and can simulate the IV response of bipolar devices with only few parameters. It does not require an extensive calculation time because it works in a localized zone of the CF and it can reproduce the cycle to cycle variability observed in experimental data.

4. A model for 1T1R measurement configuration

Summary

4.1 Intrinsic IV switching characteristics 85
4.2 Intrinsic resistive switching parameters 87
4.2.1 Number of conduction channels in LRS 88
4.3 Model for the resistive switching of 1T1R ReRAM cell structure . . 89

The conventional characterization of ReRAM devices relies on the use of one transistor (1T) to control current and protect devices from hard dielectric breakdown. These elements help to cell performance and reliability characterization, but they can also generate their own electrical signal which could avoid the real characterization of the ReRAM element (see Fig. 4.2). Thus, other structures, such as 2R test structure [133] or one-resistor (1R) RRAM array [134], has been proposed to avoid the effect of the external element during measurement.

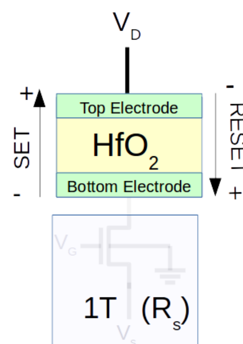

FIGURE 4.1. – 1T1R test structures during forming, set and reset electrical characterization of HfO_2-based ReRAM.

However, in the modelling of the resistive switching of ReRAM devices, the effect of the transistor has not been included yet. We propose that the current

controlled by the transistor is limited by an external parasitic effect that can be represented by a series resistance R_s. In this chapter, we extract R_s of the IV experimental curves, and after, we modify the model proposed in chapter 3 to include the series resistance.

4.1. Intrinsic IV switching characteristics

We propose that the electrical response of the transistor, represented by a series resistance (R_s), has ohmic behavior. This contribution exhibits a linear relationship between the applied voltage and the electric current that can be observed in the the IV curves after set transition, when the system change from HRS to LRS, and there is a remanent linear relationship (see Fig. 4.2) [135]. We identified this region in IV curves and, by the fitting with a function $I = G_s V$, we determined the R_s value.

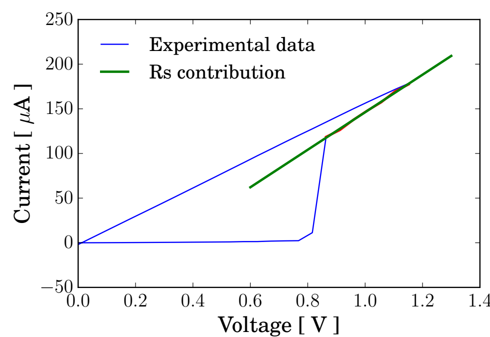

FIGURE 4.2. – IV characteristic of the HfO_2-based ReRAM with area $135x135nm^2$, where one can observe the linear relationship related to series resistance generated by the transistor.

Thus, to find the intrinsic switching characteristics of the ReRAM devices, the voltage drop over the access resistance R_s is subtracted from IV curves [133]. In Fig. 4.3, the IV experimental curves (in black), along with the intrinsic IV response of the ReRAM device (in red), are presented. The R_s value has been also included in all plots.

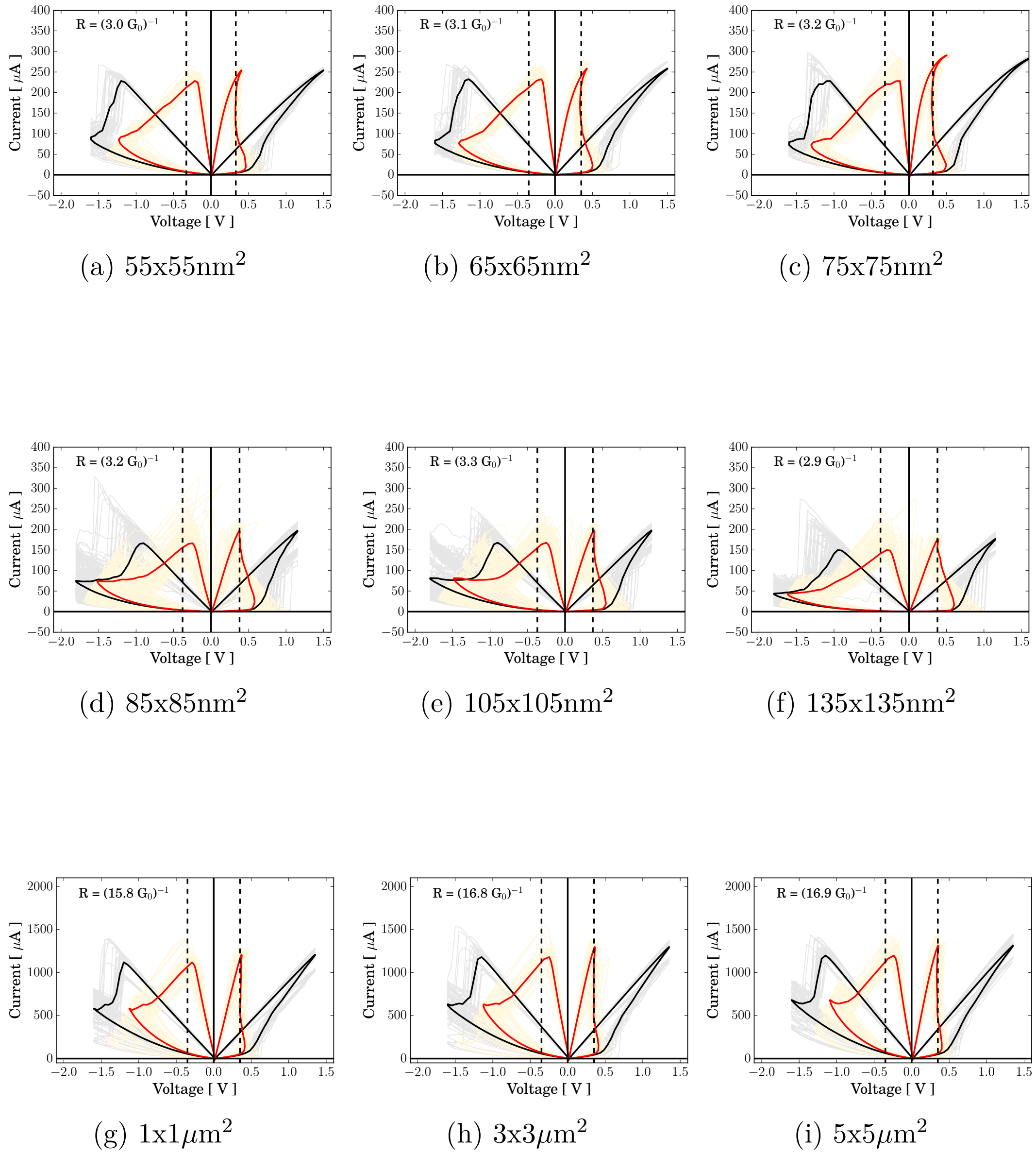

(a) $55x55nm^2$ (b) $65x65nm^2$ (c) $75x75nm^2$

(d) $85x85nm^2$ (e) $105x105nm^2$ (f) $135x135nm^2$

(g) $1x1\mu m^2$ (h) $3x3\mu m^2$ (i) $5x5\mu m^2$

FIGURE 4.3. – Experimental IV curves (black) and the intrinsic electrical response for the HfO_2-based ReRAM (red).

4.2. Intrinsic resistive switching parameters

To characterize the real behavior of the ReRAM devices, we determined the parameters used the describe the resistive switching (V_{set}, V_{reset}, G, I_o and α) from the intrinsic IV curves (in red).

As it has been reported before in [133], after the extraction of the R_s, the set switching triggers to a constant threshold voltage (intrinsic V_{set}) that is similar among all samples. Regarding the intrinsic reset voltage, V_{reset}, this value is shifted to the right, and it is smaller than V_{set}. These two parameters as a function of the area are plotted in Fig. 4.4.

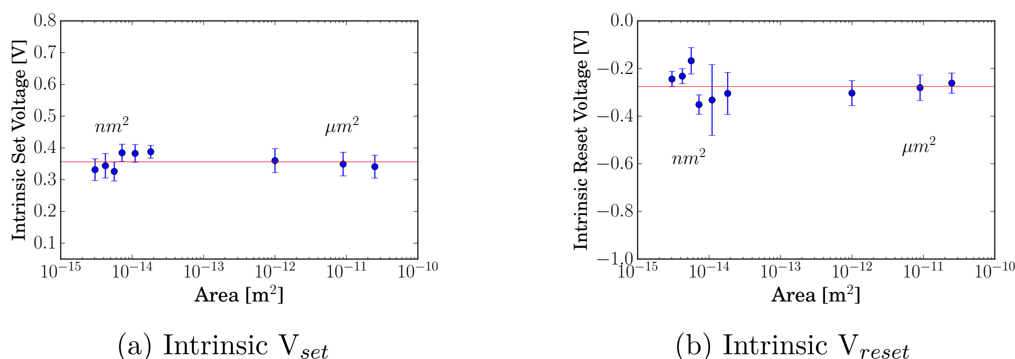

(a) Intrinsic V_{set} (b) Intrinsic V_{reset}

FIGURE 4.4. – Instrinsic V_{set} and V_{reset} as a function of the area.

The value of the intrinsic conductance (G_{int}) can be calculated by $\frac{1}{G_{int}} = \frac{1}{G} - \frac{1}{G_s}$, where G is the conductance of the system, determined in section 2.5.3.1, and G_s is the series conductance, $G_s = 1/R_s$, determined in 4.1. One value of G_{int} has been determined for each group of data. They are presented in table 4.1 :

	G	G_s	G_{int}
nm^2	176 μS	241.51 μS	647.21 μS
nm^2	960 μS	1278.42 μS	3854.29 μS

TABLE 4.1. – Intrinsic conductance

On the other hand, to describe the conduction in HRS, the values of I_o and α were determined by the fitting of the intrinsic IV curves. Two characteristic values of I_o can be identified in Fig. 4.5 : 6.465μA for nm-size samples and 76.385μA for μ-size samples. However, α has a linear relationship with the area (A) given by : $\alpha = 0.038 \log(A) + 3.6$.

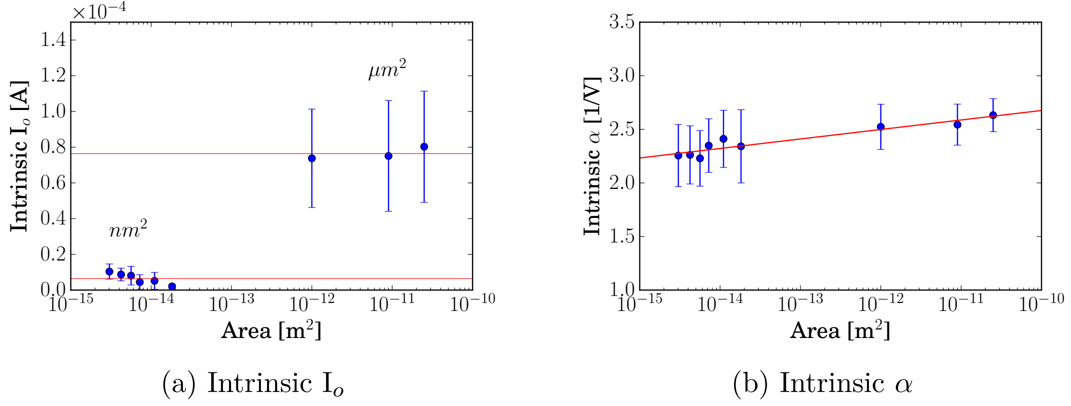

(a) Intrinsic I_o (b) Intrinsic α

FIGURE 4.5. – Instrinsic I_o and α as a function of the area.

4.2.1. Number of conduction channels in LRS

HfO_2-based ReRAM devices have been studied in the literature using QPC model [26, 84, 98, 109, 114, 131]. QPC model assumes the existence of a narrow constriction between two wide electrically conducting regions, of a width comparable to the electronic wavelength. The difference between the two states, HRS or LRS, is attributed to the change of the potential barrier caused by size modulation of the constriction of the CF that acts a quantum point contact (see appendix D.1). When the system is in LRS, the conduction is ideally ballistic, and the current can be written by :

$$I \approx \frac{NG_o}{1 + NG_oR_{sc}}V \tag{4.1}$$

where G_o is the quantum conductance unit, G is the experimental conductance, N is the number of active channels in the filament, and R_{sc} is the series resistance external to the constriction. Assuming that the parasitic effect represented by R_s also quantify the resistance external to the constriction (active region in our model), we can obtain the number of conduction channels for each sample, using eq. 4.2.

$$N = \frac{1}{G_0}\left(\frac{G}{1 - GR_s}\right) \tag{4.2}$$

The statistical distribution of N shows that the number of active channels in nm-size samples has the same order of magnitude, while in the μm-size samples is one order of magnitude larger (see Fig. 4.6).

The model proposed in chapter 3 is consistent with the QPC model, in the sense that it works with the narrow zone of the filament, such as the constriction

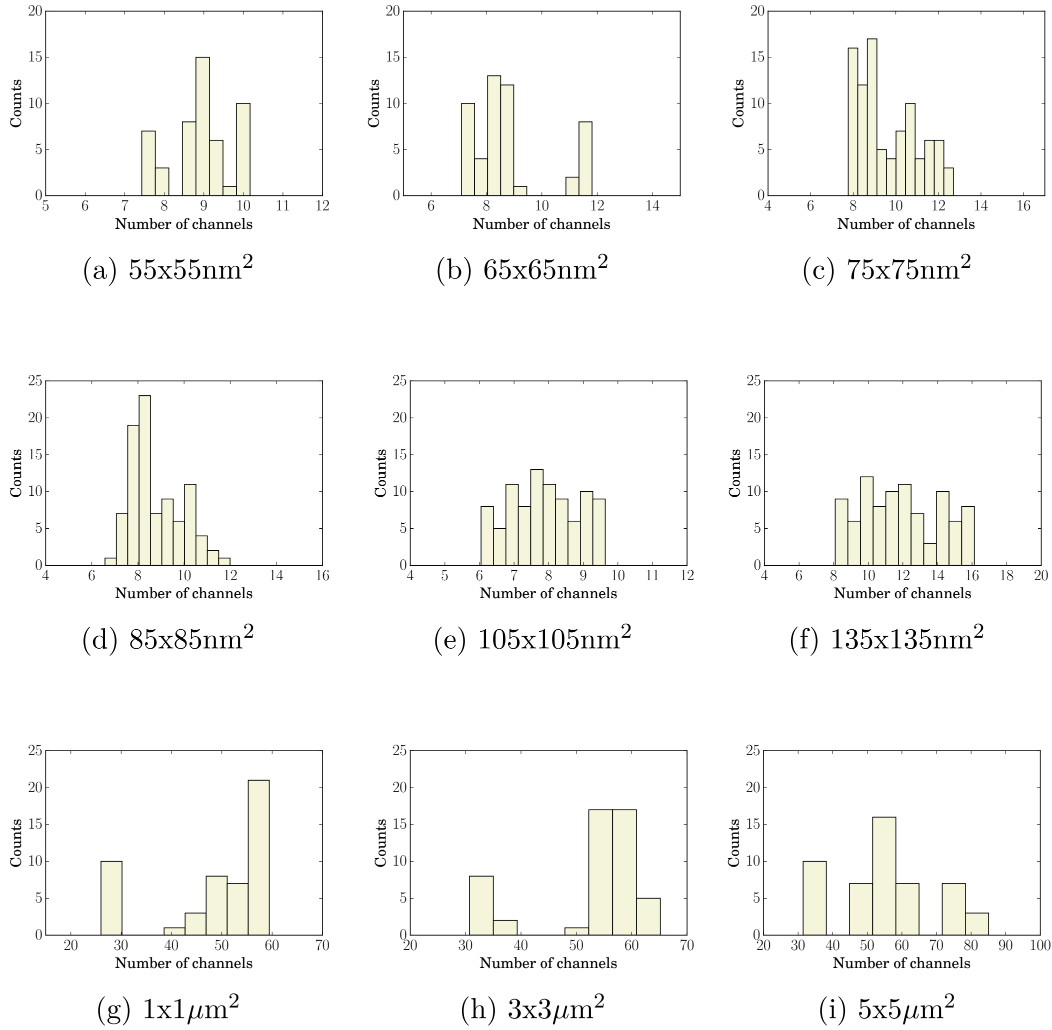

FIGURE 4.6. – Distribution of the number of active channels in LRS

of the QPC model. The vertical chains used in the circuit representation of the CF could be understood as a representation of the multiple conduction channels.

4.3. Model for the resistive switching of 1T1R ReRAM cell structure

Most of the models proposed in the literature for resistive switching of ReRAM devices do not consider the electrical response of the series resistance R_s that could be associated with the 1T1R configuration used for measurement [48, 63, 83, 136–139]. In this way, the model proposed in chapter 3 is modified to include the series resistance (R_s). A schema of this new model is presented in fig. 4.7.

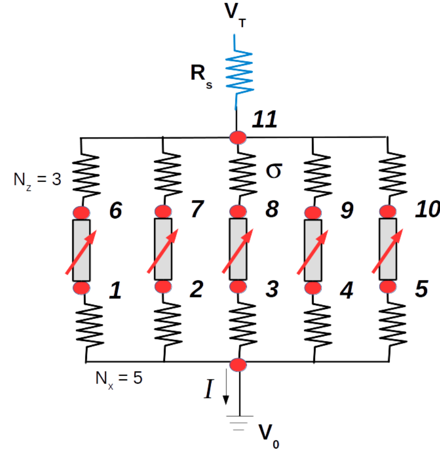

FIGURE 4.7. – 5 chain model with a series resistance R_s

Such as in the previous model, Kirchhoff's equations at each node must be written according with the state of the breaker : Ohmic conduction (eq. 3.2) or TAT conduction (eq. 3.6). For the 5-chain model of Fig. 4.7, the system of nonlinear equations is presented in table 4.2, where σ_s is the inverse of R_s.

Node	Equation
0	$f_0 = I + \sigma(V_0 - V_1) + \sigma(V_0 - V_2) + \sigma(V_0 - V_3) + \sigma(V_0 - V_4) + \sigma(V_0 - V_5)$
1	$f_1 = \sigma(V_1 - V_0) + I_o \sinh[\alpha(V_1 - V_6)]$
2	$f_2 = \sigma(V_2 - V_0) + I_o \sinh[\alpha(V_2 - V_7)]$
3	$f_3 = \sigma(V_3 - V_0) + I_o \sinh[\alpha(V_3 - V_8)]$
4	$f_4 = \sigma(V_4 - V_0) + I_o \sinh[\alpha(V_4 - V_9)]$
5	$f_5 = \sigma(V_5 - V_0) + I_o \sinh[\alpha(V_5 - V_{10})]$
6	$f_6 = I_o \sinh[\alpha(V_6 - V_1)] + \sigma(V_6 - V_{11})$
7	$f_7 = I_o \sinh[\alpha(V_7 - V_2)] + \sigma(V_7 - V_{11})$
8	$f_8 = I_o \sinh[\alpha(V_8 - V_3)] + \sigma(V_8 - V_{11})$
9	$f_9 = I_o \sinh[\alpha(V_9 - V_4)] + \sigma(V_9 - V_{11})$
10	$f_{10} = I_o \sinh[\alpha(V_{10} - V_5)] + \sigma(V_{10} - V_{11})$
11	$f_{11} = \sigma_s(V_{11} - V_{top}) + \sigma(V_{11} - V_6) + \sigma(V_{11} - V_7) + \sigma(V_{11} - V_8) + \sigma(V_{11} - V_9) + \sigma(V_{11} - V_{10})$

TABLE 4.2. – Kirchhoff's equations for an active region of five vertical chains with an access series resistance R_s.

This model has been implemented in a Python-based script. The intrinsic parameters presented in figures 4.4 and 4.5 have been used for model calibration. The value of the conductance has been divided into two contributions : σ_s (G_s) for the series conductance and σ (G_{int}) for the intrinsic ReRAM's contribution (see tab. 4.1).

Experimental data along with simulation results are presented in Fig. 4.8. Grey lines correspond to the model with the mean value in black, while light blue lines correspond to experimetal curves with the mean value in blue.

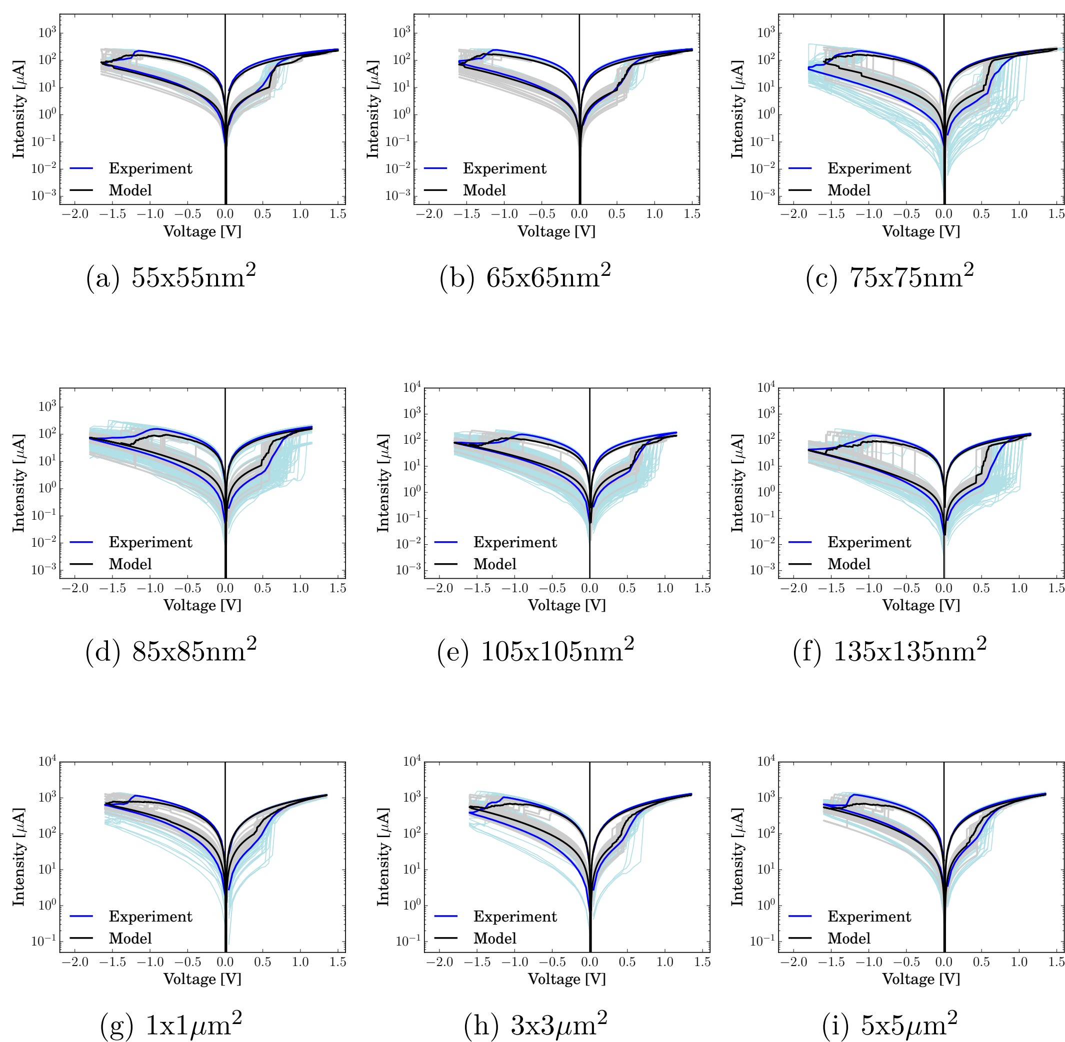

(a) 55x55nm^2 (b) 65x65nm^2 (c) 75x75nm^2

(d) 85x85nm^2 (e) 105x105nm^2 (f) 135x135nm^2

(g) 1x1μm^2 (h) 3x3μm^2 (i) 5x5μm^2

FIGURE 4.8. – Model and experimental current–voltage response of HfO_2ReRAM devices. Grey lines correspond to the model and light blue lines correspond to experimetal curves.

Model simulations have been validated by comparing measured and modelled

curves. A good relationship between the experimental and the simulated data is found. However, it must be noted that the model has a lack of accuracy in the reset switching. This could be improved if the reset process is carried by the current instead of the voltage. This will be the topic of a future work.

Conclusion

In this manuscript, a model for the resistive switching of bipolar HfO_2-based ReRAM devices is proposed. First, a complete analysis of the electrical response of devices of two areas (nm^2 and μm^2) was done. We propose that the resistive switching can be analyzed with five parameters : V_{set}, V_{reset}, G, I_o and α. Two of them are the voltages where the system change its state, V_{set} and V_{reset}, and the others are related to the conduction mechanisms. For our devices, we worked with ohmic conduction for LRS and trap assisted tunneling conduction for HRS.

First, the electroforming process was studied. It is one of the most area-related aspects of ReRAM characterization and it is imporant when assessing scalability. In this study, we found that the forming voltage is strongly dependent of the device area and in fact, it increases with the scaling. This behavior can be explained because, in small devices, the number of pre-fabricated defects (oxygen vacancies) is lower. Thus, the probability to form conductive paths reduces. Our values for forming voltage are under the 5V reported before [94].

Second, the current-voltage characteristics were studied. All the electrical parameters had been analyzed statistically due to the the stochastic nature of the resistive switching. It is a fact that the probability to recreate the same conductive filament at every cycle is extremely small, thus the electrical parameters must be studied as a distribution of values instead of only a representative value.

After the statistical analysis of V_{set} and V_{reset}, we identified some interesting characteristics. According to the distribution of V_{set}, one could infer that the energy required to move the oxygen vacancies and regenerate the CF has similar characteristics between cycles. Moreover, V_{set} can be properly represented by a Gaussian distribution in all samples.

On the other hand, V_{reset} showed a wide distribution of values that are only bell-shaped in small samples. Physically, during reset, the oxygen ions are forced to go back to the oxide layer and recombine with the oxygen vacancies. In small samples, these two processes are spacially limited and are controlled. However, we can mention that all devices work with low operation voltages (<1.5V).

During electrical characterization, all samples showed a cycle to cycle variability, especially in the HRS under both, positive and negative voltages. This behavior could be generated for two reasons. First, after reset transition the CF is partially destroyed and traps (oxygen vacancies) remain randomly distributed. And second, the variabiliy could be associated to random telegraph noise (RTN) [31, 56, 116] generated by the trap assisted tunneling process. The causes of variability had not been studied in this work. However, we have analyzed the ex-

perimental IV response to quantify it and to include it in the model. Specifically, in HRS it has been found that the relative standard deviation (RSD), that is a statistical measure of the dispersion of data around the mean (RDS = σ/μ), is the same in all samples. This factor allows to reproduce the HRS's variability in the model.

The model presented in this manuscript is based on the circuit representation of the narrowest zone of the CF, called "active region". This region is represented by a network of vertical chains, each one composed of three electrical elements. Two of them are always low resistive and the third one is a breaker that changes its state during the switching. In HfO_2-based ReRAM, the "active region" would correspond to the sub-stoichiometric region at the HfO_2/Hf interface where the formation and rupture of the CF takes place. However, it must be noted that this sub-stoichiometric region is a common characteristic of all ReRAM devices and most of the times it is attribuited to the metal/oxide interface [66].

The idea of working with the constriction of the CF (active region) has been proposed before in the "Hour glass" model [96] or in the quantum point contact model [84, 97, 131]. Nevertheless, our approach is different because we propose a circuit representation of this region, where the electrical elements can change its state between HR or LR according with a switching probability (P_s). Working with a probability is a way to include the stochastic nature of the resistive switching observed in experimental data. Further, the dependency of P_s with the threshold voltage (V_{set} or V_{reset}) is reasonable since the resistive switching mechanism is mainly a self-accelerated process triggered by the electric field. There is a direct relationship between our model and the behavior of real systems. The vertical chains of the active region represent the conductive paths that form the CF, while the conection or deconection of the breakers represents the formation or rupture of this paths caused by the migration of oxygen vacancies and ions under the influence of the electric field [34, 73].

Regarding conduction mechanism, our model allows a suitable simulation of the resistive switching working with Ohmic conduction in LRS and trap assited tunneling in HRS. However, the conduction mechanisms in ReRAM devices are diverse and strongly dependent on the insulator/dielectric characteristics, fabrication process and electroforming conditions [87–89]. With this background, it is important to note that the model proposed in this work can easily be modified to include other conduction mechanisms.

The simulation results of nm^2 and μm^2 devices show good agreement with experimental data. Although both kind of samples follow similar behavior, the model was calibrated independently. There are two parameters that are appreciably different : the conductance and the current I_o. Because they characterize the CF conditions in the LRS (G) and HRS (I_o), one could suggest that the CF has different size between the two kinds of samples. The number of conductive channels, found in chapter 4, also confirms this hypothesis.

Finally, a modified model was presented. The electrical response of the transis-

tor, used in the 1T1R configuration, has been included in the model as a series resistance, R_s. This element improves the simulation, especially in the HRS. For model calibration, the intrinsic resistive switching parameters (V_{set}, V_{reset}, G, I_o and α) were determined. To do it, first, the series resistance R_s was subtracted from the experimental IV curves.

Although, the simulation has still a lack of accuracy under negative voltages, we propose that reset switching could be considered as a current-controlled process, instead of a voltage-controlled mechanism. Under this condition, a switching probability that depends of current would be necessary. This will be the next step in the development of the model.

Among some advantages of this model, one can mention that it can be calibrated to other types of ReRAM with similar IV characteristics. For instance, for the Pt/Ni :SiO_2/TiN structure [140] or the Ti/ZrO_2/Pt device [141]. Further, it can be modified to include other kind of conduction mechanism, or to include other elements, such as the R_s. On the other hand, it is important to mention that the stochastic approach of this model could be applied to other devices that have this characteristic.

In summary, the model proposed in this work is flexible to be modified and implemented for the user for other kind of ReRAM or stochastic devices. These characteristics makes it a powerful tool for simulation and studying of the resistive switching of ReRAM devices.

Bibliographie

[1] J.S. Meena, S.M. Sze, U. Chand et al. « Overview of emerging nonvolatile memory technologies ». In : *Nanoscale Research Letters* 9.1 (sept. 2014), p. 526. ISSN : 1556-276X. DOI : 10.1186/1556-276X-9-526. URL : https://doi.org/10.1186/1556-276X-9-526 (cf. p. 24, 27, 28).

[2] R. Waser et M. Aono. « Nanoionics-based resistive switching memories ». In : *Nature Materials* 6.833 (). DOI : 10.1038/nmat2023. URL : http://dx.doi.org/10.1038/nmat2023 (cf. p. 24, 30).

[3] D. Kumar, R. Aluguri, U. Chand et al. « Metal Oxide Resistive Switching Memory : Materials, Properties, and Switching Mechanisms ». In : (mai 2017) (cf. p. 24, 30).

[4] C. Walczyk, D. Walczyk, T. Schroeder et al. « Impact of Temperature on the Resistive Switching Behavior of Embedded $hboxHfO_2$-Based RRAM Devices ». In : *IEEE Transactions on Electron Devices* 58.9 (sept. 2011), p. 3124–3131. ISSN : 0018-9383. DOI : 10.1109/TED.2011.2160265 (cf. p. 24, 30, 37, 127).

[5] S. Park, H.S. Kim, M. Choo et al. « RRAM-based synapse for neuromorphic system with pattern recognition function ». In : *Electron Devices Meeting, 1988. IEDM '88. Technical Digest., International*. T. 2012. Déc. 2012, p. 10.2.1–10.2.4. ISBN : 978-1-4673-4872-0 (cf. p. 24).

[6] S. Mittal. « A Survey of ReRAM-Based Architectures for Processing-In-Memory and Neural Networks ». In : *Machine Learning and Knowledge Extraction* 1.1 (2018), p. 75–114. ISSN : 2504-4990. DOI : 10.3390/make1010005. URL : http://www.mdpi.com/2504-4990/1/1/5 (cf. p. 24).

[7] J. Jang, S. Park, Y. Jeong et al. « ReRAM-based synaptic device for neuromorphic computing ». In : *2014 IEEE International Symposium on Circuits and Systems (ISCAS)*. Juin 2014, p. 1054–1057. DOI : 10.1109/ISCAS.2014.6865320 (cf. p. 24).

[8] S. Kim et Y. K. Choi. « A Comprehensive Study of the Resistive Switching Mechanism in $hboxAl/TiO_x/hboxTiO_2/hboxAl$-Structured RRAM ». In : *IEEE Transactions on Electron Devices* 56.12 (déc. 2009), p. 3049–3054. ISSN : 0018-9383. DOI : 10.1109/TED.2009.2032597 (cf. p. 24, 30).

[9] Z. Wei, Y. Kanzawa, K. Arita et al. « Highly reliable TaO_x ReRAM and direct evidence of redox reaction mechanism ». In : *2008 IEEE International Electron Devices Meeting*. Déc. 2008, p. 1–4. doi : 10.1109/IEDM.2008.4796676 (cf. p. 24).

[10] H. Y. Lee, P. S. Chen, T. Y. Wu et al. « Low power and high speed bipolar switching with a thin reactive Ti buffer layer in robust HfO_2 based RRAM ». In : *2008 IEEE International Electron Devices Meeting*. Déc. 2008, p. 1–4. doi : 10.1109/IEDM.2008.4796677 (cf. p. 24, 37, 63).

[11] D. Panda, P. P. Sahu et T. Y. Tseng. « A Collective Study on Modeling and Simulation of Resistive Random Access Memory ». In : *Nanoscale Research Letters* 13.1 (jan. 2018), p. 8. issn : 1556-276X. doi : 10.1186/s11671-017-2419-8. url : https://doi.org/10.1186/s11671-017-2419-8 (cf. p. 24).

[12] S. Yu, Y. Wu et H.S.P. Wong. « Investigating the switching dynamics and multilevel capability of bipolar metal oxide resistive switching memory ». In : *Applied Physics Letters* 98.10 (2011), p. 103514. doi : 10.1063/1.3564883. eprint : https://doi.org/10.1063/1.3564883. url : https://doi.org/10.1063/1.3564883 (cf. p. 24).

[13] P. Huang, X. Y. Liu, B. Chen et al. « A Physics-Based Compact Model of Metal-Oxide-Based RRAM DC and AC Operations ». In : *IEEE Transactions on Electron Devices* 60.12 (déc. 2013), p. 4090–4097. issn : 0018-9383. doi : 10.1109/TED.2013.2287755 (cf. p. 24).

[14] S. Larentis, F. Nardi, S. Balatti et al. « Resistive Switching by Voltage-Driven Ion Migration in Bipolar RRAM—Part II : Modeling ». In : *IEEE Transactions on Electron Devices* 59.9 (sept. 2012), p. 2468–2475. issn : 0018-9383. doi : 10.1109/TED.2012.2202320 (cf. p. 24).

[15] S. Natarajan, S. Chung, L. Paris et al. « Searching for the dream embedded memory ». In : *IEEE Solid-State Circuits Magazine* 1.3 (2009), p. 34–44. issn : 1943-0582. doi : 10.1109/MSSC.2009.933521 (cf. p. 26).

[16] R. Bez, E. Camerlenghi, A. Modelli et al. « Introduction to flash memory ». In : *Proceedings of the IEEE* 91.4 (avr. 2003), p. 489–502. issn : 0018-9219. doi : 10.1109/JPROC.2003.811702 (cf. p. 27).

[17] A. Chen. « A review of emerging non-volatile memory (NVM) technologies and applications ». In : *Solid-State Electronics* 125 (2016). Extended papers selected from ESSDERC 2015, p. 25–38. issn : 0038-1101. doi : https://doi.org/10.1016/j.sse.2016.07.006. url : http://www.sciencedirect.com/science/article/pii/S0038110116300867 (cf. p. 27).

[18] A. Fazio. « Flash Memory Scaling ». In : 29 (nov. 2004), p. 814–817 (cf. p. 27).

[19] A. Chen. « Ionic memories : Status and challenges ». In : *2008 9th Annual Non-Volatile Memory Technology Symposium (NVMTS)*. Nov. 2008, p. 1–5. doi : 10.1109/NVMT.2008.4731188 (cf. p. 27).

[20] H. Shiga, D. Takashima, S. i. Shiratake et al. « A 1.6 GB/s DDR2 128 Mb Chain FeRAM With Scalable Octal Bitline and Sensing Schemes ». In : *IEEE Journal of Solid-State Circuits* 45.1 (jan. 2010), p. 142–152. issn : 0018-9200. doi : 10.1109/JSSC.2009.2034414 (cf. p. 27).

[21] L. Goux, D. Tio Castro, G. A. M. Hurkx et al. « Degradation of the Reset Switching During Endurance Testing of a Phase-Change Line Cell ». In : *IEEE Transactions on Electron Devices* 56.2 (fév. 2009), p. 354–358. issn : 0018-9383. doi : 10.1109/TED.2008.2010568 (cf. p. 28).

[22] X. Dong, X. Wu, G. Sun et al. « Circuit and microarchitecture evaluation of 3D stacking magnetic RAM (MRAM) as a universal memory replacement ». In : *2008 45th ACM/IEEE Design Automation Conference*. Juin 2008, p. 554–559 (cf. p. 28).

[23] P. Heremans, G. H. Gelinck, R. Müller et al. « Polymer and Organic Nonvolatile Memory Devices ». In : *Chemistry of Materials* 23.3 (2011), p. 341–358. doi : 10.1021/cm102006v. eprint : https://doi.org/10.1021/cm102006v. url : https://doi.org/10.1021/cm102006v (cf. p. 28).

[24] G. S. Rose. « Overview : Memristive devices, circuits and systems ». In : *Proceedings of 2010 IEEE International Symposium on Circuits and Systems*. Mai 2010, p. 1955–1958. doi : 10.1109/ISCAS.2010.5536990 (cf. p. 29).

[25] H. S. P. Wong, H. Y. Lee, S. Yu et al. « Metal-Oxide RRAM ». In : *Proceedings of the IEEE* 100.6 (juin 2012), p. 1951–1970. issn : 0018-9219. doi : 10.1109/JPROC.2012.2190369 (cf. p. 29, 30, 32, 33, 74).

[26] Y. Y. Chen, L. Goux, S. Clima et al. « Endurance/Retention Trade-off on HfO_2/Metal Cap 1T1R Bipolar RRAM ». In : *IEEE Transactions on Electron Devices* 60.3 (mar. 2013), p. 1114–1121. issn : 0018-9383. doi : 10.1109/TED.2013.2241064 (cf. p. 29, 38, 88).

[27] M.J. Lee, C.B. Lee, D. Lee et al. « A Fast, High-Endurance and Scalable Non-Volatile Memory Device Made from Asymmetric Ta_2O_{5-x}/TaO_{2-x} Bilayer Structures ». In : 10 (juil. 2011), p. 625–30 (cf. p. 29).

[28] H. Y. Lee, Y. S. Chen, P. S. Chen et al. « Evidence and solution of over-reset problem for HfO_x based resistive memory with sub-ns switching speed and high endurance ». In : *2010 International Electron Devices Meeting*. Déc. 2010, p. 19.7.1–19.7.4. doi : 10.1109/IEDM.2010.5703395 (cf. p. 29, 30, 34).

[29] D. Ielmini. « Resistive switching memories based on metal oxides : mechanisms, reliability and scaling ». In : *Semiconductor Science and Technology* 31.6 (2016), p. 063002. URL : http://stacks.iop.org/0268-1242/31/i=6/a=063002 (cf. p. 29).

[30] S. Balatti, S. Ambrogio, D. C. Gilmer et al. « Set Variability and Failure Induced by Complementary Switching in Bipolar RRAM ». In : *IEEE Electron Device Letters* 34.7 (juil. 2013), p. 861–863. ISSN : 0741-3106. DOI : 10.1109/LED.2013.2261451 (cf. p. 29).

[31] S. Ambrogio, S. Balatti, A. Cubeta et al. « Understanding switching variability and random telegraph noise in resistive RAM ». In : *2013 IEEE International Electron Devices Meeting*. Déc. 2013, p. 31.5.1–31.5.4. DOI : 10.1109/IEDM.2013.6724732 (cf. p. 29, 93).

[32] Z. Fang, H. Y. Yu, W. J. Fan et al. « Current Conduction Model for Oxide-Based Resistive Random Access Memory Verified by Low Frequency Noise Analysis ». In : *IEEE Transactions on Electron Devices* 60.3 (mar. 2013), p. 1272–1275. ISSN : 0018-9383. DOI : 10.1109/TED.2013.2240457 (cf. p. 29).

[33] T. W. Hickmott. « Low Frequency Negative Resistance in Thin Anodic Oxide Films ». In : *Journal of Applied Physics* 33.9 (1962), p. 2669–2682. DOI : 10.1063/1.1702530. eprint : https://doi.org/10.1063/1.1702530. URL : https://doi.org/10.1063/1.1702530 (cf. p. 30).

[34] A. Sawa. « Resistive switching in transition metal oxides ». In : *Materials Today* 11.6 (2008), p. 28–36. ISSN : 1369-7021. DOI : https://doi.org/10.1016/S1369-7021(08)70119-6. URL : http://www.sciencedirect.com/science/article/pii/S1369702108701196 (cf. p. 30, 32, 33, 94).

[35] R. Waser, R. Dittmann, G. Staikov et al. « Redox-Based Resistive Switching Memories – Nanoionic Mechanisms, Prospects, and Challenges ». In : *Advanced Materials* 21.25-26 (), p. 2632–2663. DOI : 10.1002/adma.200900375. eprint : https://onlinelibrary.wiley.com/doi/pdf/10.1002/adma.200900375. URL : https://onlinelibrary.wiley.com/doi/abs/10.1002/adma.200900375 (cf. p. 30, 31, 52).

[36] H. Shima, F. Takano, H. Akinaga et al. « Resistance switching in the metal deficient-type oxides : NiO and CoO ». In : *Applied Physics Letters* 91.1 (2007), p. 012901. DOI : 10.1063/1.2753101. eprint : https://doi.org/10.1063/1.2753101. URL : https://doi.org/10.1063/1.2753101 (cf. p. 30).

[37] C.Y. Lin, D.Y. Lee, S.Y. Wang et al. « Effect of thermal treatment on resistive switching characteristics in Pt/Ti/Al_2O_3/Pt devices ». In : *Surface and Coatings Technology* 203.5 (2008). Proceedings of the 35th International Conference on Metallurgical Coatings and Thin Films, p. 628–631. ISSN :

0257-8972. DOI : https://doi.org/10.1016/j.surfcoat.2008.06.133. URL : http://www.sciencedirect.com/science/article/pii/S0257897208005720 (cf. p. 30).

[38] K. Nagashima, T. Yanagida, K. Oka et al. « Unipolar resistive switching characteristics of room temperature grown SnO_2 thin films ». In : *Applied Physics Letters* 94.24 (2009), p. 242902. DOI : 10.1063/1.3156863. eprint : https://doi.org/10.1063/1.3156863. URL : https://doi.org/10.1063/1.3156863 (cf. p. 30).

[39] F.C. Chiu, W.C. Shih et J.J. Feng. « Conduction mechanism of resistive switching films in MgO memory devices ». In : *Journal of Applied Physics* 111.9 (2012), p. 094104. DOI : 10.1063/1.4712628. eprint : https://doi.org/10.1063/1.4712628. URL : https://doi.org/10.1063/1.4712628 (cf. p. 30).

[40] A. Chen, S. Haddad, Y. C. Wu et al. « Erasing characteristics of Cu_2O metal-insulator-metal resistive switching memory ». In : *Applied Physics Letters* 92.1 (2008), p. 013503. DOI : 10.1063/1.2828864. eprint : https://aip.scitation.org/doi/pdf/10.1063/1.2828864. URL : https://aip.scitation.org/doi/abs/10.1063/1.2828864 (cf. p. 30).

[41] H. Mahne, L. Berger, D. Martin et al. « Filamentary resistive switching in amorphous and polycrystalline Nb_2O_5 thin films ». In : *Solid-State Electronics* 72 (2012), p. 73–77. ISSN : 0038-1101. DOI : https://doi.org/10.1016/j.sse.2012.01.005. URL : http://www.sciencedirect.com/science/article/pii/S003811011200007X (cf. p. 30).

[42] C. Rohde, B.J. Choi, D.S. Jeong et al. « Identification of a determining parameter for resistive switching of TiO_2 thin films ». In : *Applied Physics Letters* 86.26 (2005), p. 262907. DOI : 10.1063/1.1968416. eprint : http://dx.doi.org/10.1063/1.1968416. URL : http://dx.doi.org/10.1063/1.1968416 (cf. p. 30).

[43] B. J. Choi, D. S. Jeong, S. K. Kim et al. « Resistive switching mechanism of TiO_2 thin films grown by atomic-layer deposition ». In : *Journal of Applied Physics* 98.3 (2005), p. 033715. DOI : 10.1063/1.2001146. eprint : https://doi.org/10.1063/1.2001146. URL : https://doi.org/10.1063/1.2001146 (cf. p. 30, 32).

[44] H.Y. Jeong, J.Y. Lee et S.Y. Choi. « Direct observation of microscopic change induced by oxygen vacancy drift in amorphous TiO_2 thin films ». In : *Applied Physics Letters* 97.4 (2010), p. 042109. DOI : 10.1063/1.3467854. eprint : https://doi.org/10.1063/1.3467854. URL : https://doi.org/10.1063/1.3467854 (cf. p. 30, 32).

[45] S. Yu, X. Guan et H.S. Philip Wong. « Conduction mechanism of TiN/HfO_x/Pt resistive switching memory : A trap-assisted-tunneling model ». In : *Applied Physics Letters* 99.6 (2011), p. 063507. DOI : 10.1063/1.3624472. eprint : https://doi.org/10.1063/1.3624472. URL : https://doi.org/10.1063/1.3624472 (cf. p. 30, 36, 74).

[46] S. Privitera, G. Bersuker, S. Lombardo et al. « Conductive filament structure in HfO_2 resistive switching memory devices ». In : 111 (sept. 2015) (cf. p. 30, 32, 46).

[47] S. Yu, X. Guan et H.S.P. Wong. « On the stochastic nature of resistive switching in metal oxide RRAM : Physical modeling, monte carlo simulation, and experimental characterization ». In : *2011 International Electron Devices Meeting*. Déc. 2011, p. 17.3.1–17.3.4. DOI : 10.1109/IEDM.2011.6131572 (cf. p. 30, 37, 126).

[48] E. A. Miranda, C. Walczyk, C. Wenger et al. « Model for the Resistive Switching Effect in HfO_2 MIM Structures Based on the Transmission Properties of Narrow Constrictions ». In : *IEEE Electron Device Letters* 31.6 (juin 2010), p. 609–611. ISSN : 0741-3106. DOI : 10.1109/LED.2010.2046310 (cf. p. 30, 37, 46, 89, 127–130).

[49] S. Long, L. Perniola, C. Cagli et al. « Voltage and Power-Controlled Regimes in the Progressive Unipolar RESET Transition of HfO_2-Based RRAM ». In : *Scientific Reports* 3.2929 (2013). URL : http://www.ncbi.nlm.nih.gov/pmc/articles/PMC3796310/ (cf. p. 30, 46, 52, 55).

[50] G. Bersuker, J. Yum, V. Iglesias et al. « Grain boundary-driven leakage path formation in HfO_2 dielectrics ». In : *2010 Proceedings of the European Solid State Device Research Conference*. Sept. 2010, p. 333–336. DOI : 10.1109/ESSDERC.2010.5618225 (cf. p. 30, 32, 37, 46, 54, 74).

[51] L. Larcher, O. Pirrotta, F. M. Puglisi et al. « Progresses in Modeling HfO_x RRAM Operations and Variability ». In : *ECS Transactions* 64.14 (2014), p. 49–60. DOI : 10.1149/06414.0049ecst. eprint : http://ecst.ecsdl.org/content/64/14/49.full.pdf+html. URL : http://ecst.ecsdl.org/content/64/14/49.abstract (cf. p. 30, 37).

[52] L. Larcher, F. M. Puglisi, P. Pavan et al. « A Compact Model of Program Window in HfO_x RRAM Devices for Conductive Filament Characteristics Analysis ». In : *IEEE Transactions on Electron Devices* 61.8 (août 2014), p. 2668–2673. ISSN : 0018-9383. DOI : 10.1109/TED.2014.2329020 (cf. p. 30, 127).

[53] S. Ambrogio, S. Balatti, A. Cubeta et al. « Statistical Fluctuations in HfO_x Resistive-Switching Memory : Part I - Set Reset Variability ». In : *IEEE Transactions on Electron Devices* 61.8 (août 2014), p. 2912–2919. ISSN : 0018-9383. DOI : 10.1109/TED.2014.2330200 (cf. p. 30).

[54] P. Lorenzi, R. Rao et F. Irrera. « Forming Kinetics in HfO_2 Based RRAM Cells ». In : *IEEE Transactions on Electron Devices* 60.1 (jan. 2013), p. 438–443. ISSN : 0018-9383. DOI : 10.1109/TED.2012.2227324 (cf. p. 30).

[55] B. Hudec, I.T. Wang, W.L. Lai et al. « Interface engineered HfO_2-based 3D vertical ReRAM ». In : *Journal of Physics D : Applied Physics* 49.21 (2016), p. 215102. URL : http://stacks.iop.org/0022-3727/49/i=21/a=215102 (cf. p. 30).

[56] S. Ambrogio, S. Balatti, A. Cubeta et al. « Statistical Fluctuations in HfO_x Resistive-Switching Memory : Part II Random Telegraph Noise ». In : *IEEE Transactions on Electron Devices* 61.8 (août 2014), p. 2920–2927. ISSN : 0018-9383. DOI : 10.1109/TED.2014.2330202 (cf. p. 30, 93).

[57] B. Govoreanu, G. S. Kar, Y. Y. Chen et al. « 10x10nm^2 Hf/HfO_x crossbar resistive RAM with excellent performance, reliability and low-energy operation ». In : *2011 International Electron Devices Meeting*. Déc. 2011, p. 31.6.1–31.6.4. DOI : 10.1109/IEDM.2011.6131652 (cf. p. 30, 37, 39, 40).

[58] H. Akinaga et H. Shima. « Resistive Random Access Memory (ReRAM) Based on Metal Oxides ». In : *Proceedings of the IEEE* 98.12 (déc. 2010), p. 2237–2251. ISSN : 0018-9219. DOI : 10.1109/JPROC.2010.2070830 (cf. p. 30, 32).

[59] J.J. Yang, J. Borghetti, D. Murphy et al. « A Family of Electronically Reconfigurable Nanodevices ». In : *Advanced Materials* 21.37 (), p. 3754–3758. DOI : 10.1002/adma.200900822. eprint : https://onlinelibrary.wiley.com/doi/pdf/10.1002/adma.200900822. URL : https://onlinelibrary.wiley.com/doi/abs/10.1002/adma.200900822 (cf. p. 30).

[60] S. Liu, X. Zhao, Q. Li et al. « Analysis of the Negative-SET Behaviors in Cu/ZrO_2/Pt Devices ». In : *Nanoscale Research Letters* 11.1 (déc. 2016), p. 542. ISSN : 1556-276X. DOI : 10.1186/s11671-016-1762-5. URL : https://doi.org/10.1186/s11671-016-1762-5 (cf. p. 30).

[61] M. N. Kozicki, Mira Park et M. Mitkova. « Nanoscale memory elements based on solid-state electrolytes ». In : *IEEE Transactions on Nanotechnology* 4.3 (mai 2005), p. 331–338. ISSN : 1536-125X. DOI : 10.1109/TNANO.2005.846936 (cf. p. 30).

[62] J.F. Gibbons et W.E. Beadle. « Switching properties of thin Nio films ». In : *Solid-State Electronics* 7.11 (1964), p. 785–790. ISSN : 0038-1101. DOI : https://doi.org/10.1016/0038-1101(64)90131-5. URL : http://www.sciencedirect.com/science/article/pii/0038110164901315 (cf. p. 30).

[63] S.C. Chae, J.S. Lee, S. Kim et al. « Random Circuit Breaker Network Model for Unipolar Resistance Switching ». In : *Advanced Materials* 20.6 (2008), p. 1154–1159. issn : 1521-4095. doi : 10.1002/adma.200702024. url : http://dx.doi.org/10.1002/adma.200702024 (cf. p. 31, 89, 127).

[64] S. Ambrogio, B. Magyari, N. Onofrio et al. « Modeling resistive switching materials and devices across scales ». In : *Journal of Electroceramics* (juin 2017), p. 1–22 (cf. p. 31, 126).

[65] K. Fujiwara, T. Nemoto, M. Rozenberg et al. « Resistance Switching and Formation of a Conductive Bridge in Metal/Binary Oxide/Metal Structure for Memory Devices ». In : 47 (août 2008), p. 6266–6271 (cf. p. 31).

[66] A. Prakash, D. Jana et S. Maikap. « TaO_x based resistive switching memories : Prospective and challenges ». In : 8 (oct. 2013), p. 418 (cf. p. 31, 32, 94).

[67] J.J. Yang, F. Miao, M.D. Pickett et al. « The mechanism of electroforming of metal oxide memristive switches ». In : *Nanotechnology* 20.21 (2009), p. 215201. url : http://stacks.iop.org/0957-4484/20/i=21/a=215201 (cf. p. 31, 42).

[68] J. Y. Son et Y.-H. Shin. « Direct observation of conducting filaments on resistive switching of NiO thin films ». In : *Applied Physics Letters* 92.22 (2008), p. 222106. doi : 10.1063/1.2931087. eprint : https://doi.org/10.1063/1.2931087. url : https://doi.org/10.1063/1.2931087 (cf. p. 32).

[69] U. Celano, Y.Y. Chen, D.J. Wouters et al. « Filament observation in metal-oxide resistive switching devices ». In : *Applied Physics Letters* 102.12 (2013), p. 121602. doi : 10.1063/1.4798525. eprint : https://doi.org/10.1063/1.4798525. url : https://doi.org/10.1063/1.4798525 (cf. p. 32).

[70] K.M. Kim, T.H. Park et C.S. Hwang. « Dual Conical Conducting Filament Model in Resistance Switching TiO_2 Thin Films ». In : 5 (jan. 2015), p. 7844 (cf. p. 32).

[71] G. Bersuker, D. C. Gilmer, D. Veksler et al. « Metal oxide resistive memory switching mechanism based on conductive filament properties ». In : *Journal of Applied Physics* 110.12 (2011), p. 124518. doi : 10.1063/1.3671565. eprint : https://doi.org/10.1063/1.3671565. url : https://doi.org/10.1063/1.3671565 (cf. p. 32, 37, 42, 127).

[72] S. Brivio, G. Tallarida, E. Cianci et al. « Formation and disruption of conductive filaments in a HfO_2/TiN structure ». In : *Nanotechnology* 25.38 (2014), p. 385705. url : http://stacks.iop.org/0957-4484/25/i=38/a=385705 (cf. p. 32, 52).

[73] A. Sawa, T. Fujii, M. Kawasaki et al. « Interface resistance switching at a few nanometer thick perovskite manganite active layers ». In : *Applied Physics Letters* 88.23 (2006), p. 232112. doi : 10.1063/1.2211147. eprint : https://doi.org/10.1063/1.2211147. url : https://doi.org/10.1063/1.2211147 (cf. p. 32, 94).

[74] P. Sun, L. Li, N. Lu et al. « Physical model of electroforming mechanism in oxide-based resistive switching devices (RRAM) ». In : *2014 12th IEEE International Conference on Solid-State and Integrated Circuit Technology (ICSICT)*. Oct. 2014, p. 1–3. doi : 10.1109/ICSICT.2014.7021263 (cf. p. 32).

[75] C. Yoshida, K. Kinoshita, T. Yamasaki et al. « Direct observation of oxygen movement during resistance switching in NiO/Pt film ». In : *Applied Physics Letters* 93.4 (2008), p. 042106. doi : 10.1063/1.2966141. eprint : https://doi.org/10.1063/1.2966141. url : https://doi.org/10.1063/1.2966141 (cf. p. 32).

[76] H.D. Lee, B. Magyari-Köpe et Y. Nishi. « Model of metallic filament formation and rupture in NiO for unipolar switching ». In : *Phys. Rev. B* 81 (19 mai 2010), p. 193202. doi : 10.1103/PhysRevB.81.193202. url : https://link.aps.org/doi/10.1103/PhysRevB.81.193202 (cf. p. 33).

[77] R. Waser, S. Menzel et V. Rana. « Recent progress in redox-based resistive switching ». In : *2012 IEEE International Symposium on Circuits and Systems*. Mai 2012, p. 1596–1599. doi : 10.1109/ISCAS.2012.6271558 (cf. p. 33).

[78] J. Kim, K. Jung, Y. Kim et al. « Switching Power Universality in Unipolar Resistive Switching Memories ». In : *Scientific Reports* 6 (2016), p. 23930 (cf. p. 33).

[79] D. C. Kim, S. Seo, S. E. Ahn et al. « Electrical observations of filamentary conductions for the resistive memory switching in NiO films ». In : *Applied Physics Letters* 88.20 (2006), p. 202102. doi : 10.1063/1.2204649. eprint : https://doi.org/10.1063/1.2204649. url : https://doi.org/10.1063/1.2204649 (cf. p. 33).

[80] Q. Zhou et J. Zhai. « Study of the bipolar resistive-switching behaviors in Pt/GdOx/TaNx structure for RRAM application ». In : *physica status solidi (a)* 211.1 (), p. 173–179. doi : 10.1002/pssa.201330098. eprint : https://onlinelibrary.wiley.com/doi/pdf/10.1002/pssa.201330098. url : https://onlinelibrary.wiley.com/doi/abs/10.1002/pssa.201330098 (cf. p. 34).

[81] S.C. Chen, Chang T.C., S.Y. Chen et al. « Bipolar resistive switching of chromium oxide for resistive random access memory ». In : *Solid-State Electronics* 62.1 (2011), p. 40–43. issn : 0038-1101. doi : https://doi.org/10.1016/j.sse.2010.12.014. url : http://www.sciencedirect.com/science/article/pii/S003811011000434X (cf. p. 34).

[82] R. Prakash et D. Kaur. « Bipolar resistive switching behavior in Cu/AlN/Pt structure for ReRAM application ». In : *Vacuum* 143 (2017), p. 102–105. issn : 0042-207X. doi : https://doi.org/10.1016/j.vacuum.2017.05.041. url : http://www.sciencedirect.com/science/article/pii/S0042207X17302968 (cf. p. 34).

[83] S. B. Lee, J. S. Lee, S. H. Chang et al. « Interface-modified random circuit breaker network model applicable to both bipolar and unipolar resistance switching ». In : *Applied Physics Letters* 98.3 (2011), p. 033502. doi : 10.1063/1.3543776. eprint : http://dx.doi.org/10.1063/1.3543776. url : http://dx.doi.org/10.1063/1.3543776 (cf. p. 34, 69, 89, 127).

[84] L. M. Prócel, L. Trojman, J. Moreno et al. « Experimental evidence of the quantum point contact theory in the conduction mechanism of bipolar HfO_2-based resistive random access memories ». In : *Journal of Applied Physics* 114.7 (2013), p. 074509. doi : 10.1063/1.4818499. eprint : https://doi.org/10.1063/1.4818499. url : https://doi.org/10.1063/1.4818499 (cf. p. 34, 37, 38, 82, 88, 94, 127, 130).

[85] H. Shima, T. Nakano et H. Akinaga. « Nanoscale chemical state analysis of resistance random access memory device reacting with Ti ». In : *Applied Physics Letters* 96.19 (2010), p. 192107. doi : 10.1063/1.3373594. eprint : https://doi.org/10.1063/1.3373594. url : https://doi.org/10.1063/1.3373594 (cf. p. 34).

[86] D.S. Jeong, H. Schroeder et R. Waser. « Coexistence of Bipolar and Unipolar Resistive Switching Behaviors in a Pt/TiO_2/Pt Stack ». In : *Electrochemical and Solid-State Letters* 10.8 (2007), G51–G53. doi : 10.1149/1.2742989. eprint : http://esl.ecsdl.org/content/10/8/G51.full.pdf+html. url : http://esl.ecsdl.org/content/10/8/G51.abstract (cf. p. 34).

[87] F.C. Chiu. « A Review on Conduction Mechanisms in Dielectric Films ». In : 2014 (fév. 2014), p. 1–18 (cf. p. 34–36, 94).

[88] E.W. Lim et M. Bassiouni. « Conduction Mechanism of Valence Change Resistive Switching Memory : A Survey ». In : 2015 (cf. p. 34, 36, 94).

[89] B. Majkusiak, P. Palestri, A. Schenk et al. « Modeling and Simulation Approaches for Gate Current Computation ». In : *Nanoscale CMOS*. Wiley-Blackwell, 2013. Chap. 7, p. 213–257. isbn : 9781118621523. doi : 10.1002/9781118621523.ch7. eprint : https://onlinelibrary.wiley.com/doi/

pdf/10.1002/9781118621523.ch7. URL : https://onlinelibrary.wiley.com/doi/abs/10.1002/9781118621523.ch7 (cf. p. 34, 35, 94).

[90] S.M. Sze. « Physics of Semiconductor Devices ». In : 27 (jan. 2007), p. 111–126 (cf. p. 36).

[91] F.C. Chiu, S. Mondal et T.M. Pan. « Structural and Electrical Characteristics of Alternative High-k Dielectrics for CMOS Applications ». In : *High-k Gate Dielectrics for CMOS Technology*. Wiley-Blackwell, 2012. Chap. 5, p. 111–184. ISBN : 9783527646340. DOI : 10.1002/9783527646340.ch5. eprint : https://onlinelibrary.wiley.com/doi/pdf/10.1002/9783527646340.ch5. URL : https://onlinelibrary.wiley.com/doi/abs/10.1002/9783527646340.ch5 (cf. p. 36).

[92] Y.H. Kim et J.C. Lee. « Reliability characteristics of high-k dielectrics ». In : *Microelectronics Reliability* 44.2 (2004), p. 183–193. ISSN : 0026-2714. DOI : https://doi.org/10.1016/j.microrel.2003.10.008. URL : http://www.sciencedirect.com/science/article/pii/S0026271403004311 (cf. p. 37).

[93] S. Pengxiao, L. Su, L. Ling et al. « Simulation study of conductive filament growth dynamics in oxide-electrolyte-based ReRAM ». In : *Journal of Semiconductors* 35.10 (2014), p. 104007. URL : http://stacks.iop.org/1674-4926/35/i=10/a=104007 (cf. p. 37, 126).

[94] Y S. Chen, h.y Lee, P. S. Chen et al. « Overview and Future Challenges of Hafnium Oxide ReRAM ». In : sept. 2010 (cf. p. 37, 93).

[95] F. M. Puglisi, L. Larcher, A. Padovani et al. « Bipolar Resistive RAM Based on HfO_2 : Physics, Compact Modeling, and Variability Control ». In : *IEEE Journal on Emerging and Selected Topics in Circuits and Systems* 6.2 (juin 2016), p. 171–184. ISSN : 2156-3357. DOI : 10.1109/JETCAS.2016.2547703 (cf. p. 37).

[96] R. Degraeve, A. Fantini, S. Clima et al. « Dynamic hour glass model for set and reset in HfO_2 RRAM ». In : *2012 Symposium on VLSI Technology (VLSIT)*. Juin 2012, p. 75–76. DOI : 10.1109/VLSIT.2012.6242468 (cf. p. 37, 81, 82, 94).

[97] X. Lian, S. Long, C. Cagli et al. « Quantum point contact model of filamentary conduction in resistive switching memories ». In : *2012 13th International Conference on Ultimate Integration on Silicon (ULIS)*. Mar. 2012, p. 101–104. DOI : 10.1109/ULIS.2012.6193367 (cf. p. 38, 82, 94, 128, 130).

[98] L. Trojman, S. Guitarra, L. M. Procel et al. « Study of the scaling and the temperature for RERAM cells using the QPC model ». In : *IEEE Latin America Transactions* 14.12 (déc. 2016), p. 4693–4698. ISSN : 1548-0992. DOI : 10.1109/TLA.2016.7816999 (cf. p. 38, 88, 118, 130).

[99] R. Prabu, S. Ramesh, M. Savith et al. « Review of Physical Vapour Deposition (PVD) techniques ». In : *International Conference on Sustainable Manufacturing*. Juil. 2013. doi : 10.13140/RG.2.1.5063.4964 (cf. p. 39, 119).

[100] M. Mao, Y. Cao, S. Yu et al. « Optimizing latency, energy, and reliability of 1T1R ReRAM through appropriate voltage settings ». In : *2015 33rd IEEE International Conference on Computer Design (ICCD)*. Oct. 2015, p. 359–366. doi : 10.1109/ICCD.2015.7357125 (cf. p. 40).

[101] Y. Fang, Y. Cai, Z. Wang et al. « Influence of selector-introduced compliance current on HfO_x RRAM switching operation ». In : *2015 15th Non-Volatile Memory Technology Symposium (NVMTS)*. Oct. 2015, p. 1–3. doi : 10.1109/NVMTS.2015.7457474 (cf. p. 41).

[102] M.J. Song, K.H. Kwon et J.G. Park. « Electro-Forming and Electro-Breaking of Nanoscale Ag Filaments for Conductive-Bridging Random-Access Memory Cell using Ag-Doped Polymer-Electrolyte between Pt Electrodes ». In : *Scientific Reports* (2017). url : https://doi.org/10.1038/s41598-017-02330-x (cf. p. 42).

[103] Y.F. Chang, P.Y. Chen, B. Fowler et al. « Understanding the resistive switching characteristics and mechanism in active SiO_x-based resistive switching memory ». In : *Journal of Applied Physics* 112 (déc. 2012). doi : 10.1063/1.4769218 (cf. p. 44).

[104] A. Chen. « Area and Thickness Scaling of Forming Voltage of Resistive Switching Memories ». In : *IEEE Electron Device Letters* 35.1 (jan. 2014), p. 57–59. issn : 0741-3106. doi : 10.1109/LED.2013.2288262 (cf. p. 44).

[105] C. Wang, W. He, Y. Tong et al. « Investigation and Manipulation of Different Analog Behaviors of Memristor as Electronic Synapse for Neuromorphic Applications ». In : 6 (mar. 2016), p. 22970 (cf. p. 45).

[106] H. Aziza, M. Bocquet, J.M. Portal et al. « A novel test structure for OxRRAM process variability evaluation ». In : *Microelectronics Reliability* 53 (2013), p. 1208–1212 (cf. p. 48).

[107] K. Ohmori, A. Shinoda, K. Kawai et al. « Reduction of cycle-to-cycle variability in ReRAM by filamentary refresh ». In : *2017 Symposium on VLSI Technology*. Juin 2017, T90–T91. doi : 10.23919/VLSIT.2017.7998206 (cf. p. 49).

[108] Y. S. Kim, J.-S. Kim, J. S. Choi et al. « Resistive switching behaviors of NiO films with controlled number of conducting filaments ». In : *Applied Physics Letters* 98.19 (2011), p. 192104. doi : 10.1063/1.3589825. eprint : https://doi.org/10.1063/1.3589825. url : https://doi.org/10.1063/1.3589825 (cf. p. 52).

[109] S. Long, X. Lian, C. Cagli et al. « A Model for the Set Statistics of RRAM Inspired in the Percolation Model of Oxide Breakdown ». In : *IEEE Electron Device Letters* 34.8 (août 2013), p. 999–1001. ISSN : 0741-3106. DOI : 10.1109/LED.2013.2266332 (cf. p. 52, 88).

[110] U. Russo, D. Ielmini, C. Cagli et al. « Filament Conduction and Reset Mechanism in NiO-Based Resistive-Switching Memory (RRAM) Devices ». In : *IEEE Transactions on Electron Devices* 56.2 (fév. 2009), p. 186–192. ISSN : 0018-9383. DOI : 10.1109/TED.2008.2010583 (cf. p. 52).

[111] S. Yu et H.P. Wong. « A Phenomenological Model for the Reset Mechanism of Metal Oxide RRAM ». In : *IEEE Electron Device Letters* 31.12 (déc. 2010), p. 1455–1457. ISSN : 0741-3106. DOI : 10.1109/LED.2010.2078794 (cf. p. 52).

[112] K. Moon, A. Fumarola, S. Sidler et al. « Bidirectional Non-Filamentary RRAM as an Analog Neuromorphic Synapse, Part I : Al/Mo/$Pr_{0.7}Ca_{0.3}MnO_3$ Material Improvements and Device Measurements ». In : *IEEE Journal of the Electron Devices Society* 6.1 (déc. 2018), p. 146–155. DOI : 10.1109/JEDS.2017.2780275 (cf. p. 57).

[113] M. Phon Houng, Y. Her Wang et W. Jyh Chang. « Current transport mechanism in trapped oxides : A generalized trap-assisted tunneling model ». In : 86 (août 1999), p. 1488–1491 (cf. p. 57).

[114] Y. Li, S. Long, Y. Liu et al. « Conductance Quantization in Resistive Random Access Memory ». In : *Nanoscale Research Letters* 10.1 (oct. 2015), p. 420. ISSN : 1556-276X. DOI : 10.1186/s11671-015-1118-6. URL : https://doi.org/10.1186/s11671-015-1118-6 (cf. p. 63, 88, 129).

[115] Q. Liu, S. Long, H. Lv et al. « Controllable Growth of Nanoscale Conductive Filaments in Solid-Electrolyte-Based ReRAM by Using a Metal Nanocrystal Covered Bottom Electrode ». In : *ACS Nano* 4.10 (2010). PMID : 20853865, p. 6162–6168. DOI : 10.1021/nn1017582. eprint : https://doi.org/10.1021/nn1017582. URL : https://doi.org/10.1021/nn1017582 (cf. p. 63).

[116] Y. T. Chung, Y. H. Liu, P. C. Su et al. « Investigation of random telegraph noise amplitudes in hafnium oxide resistive memory devices ». In : *2014 IEEE International Reliability Physics Symposium*. Juin 2014, MY.2.1–MY.2.5. DOI : 10.1109/IRPS.2014.6861157 (cf. p. 63, 93).

[117] E. Simoen, B. Kaczer, M. Toledano-Luque et al. « (Invited) Random Telegraph Noise : From a Device Physicist's Dream to a Designer's Nightmare ». In : *ECS Transactions* 39.1 (2011), p. 3–15. DOI : 10.1149/1.3615171. eprint : http://ecst.ecsdl.org/content/39/1/3.full.pdf+html. URL : http://ecst.ecsdl.org/content/39/1/3.abstract (cf. p. 63).

[118] M. Villena, J. Roldan, F. Jiménez-Molinos et al. « SIM^{2}RRAM : a physical model for RRAM devices simulation ». In : (oct. 2017) (cf. p. 68, 126, 127).

[119] Z. Jiang, Y. Wu, S. Yu et al. « A Compact Model for Metal–Oxide Resistive Random Access Memory With Experiment Verification ». In : *IEEE Transactions on Electron Devices* 63.5 (mai 2016), p. 1884–1892. issn : 0018-9383. doi : 10.1109/TED.2016.2545412 (cf. p. 68).

[120] S. Yu, B. Gao, Z. Fang et al. « A neuromorphic visual system using RRAM synaptic devices with Sub-pJ energy and tolerance to variability : Experimental characterization and large-scale modeling ». In : *2012 International Electron Devices Meeting*. Déc. 2012, p. 10.4.1–10.4.4. doi : 10.1109/IEDM.2012.6479018 (cf. p. 68).

[121] X. Guan, S. Yu et H.P. Wong. « A SPICE Compact Model of Metal Oxide Resistive Switching Memory With Variations ». In : *IEEE Electron Device Letters* 33.10 (oct. 2012), p. 1405–1407. issn : 0741-3106. doi : 10.1109/LED.2012.2210856 (cf. p. 68).

[122] M. Bocquet, D. Deleruyelle, H. Aziza et al. « Robust Compact Model for Bipolar Oxide-Based Resistive Switching Memories ». In : *IEEE Transactions on Electron Devices* 61.3 (mar. 2014), p. 674–681. issn : 0018-9383. doi : 10.1109/TED.2013.2296793 (cf. p. 68).

[123] J. Noh, M. Jo, C. Y. Kang et al. « Development of a Semiempirical Compact Model for DC/AC Cell Operation of HfO_x-Based ReRAMs ». In : *IEEE Electron Device Letters* 34.9 (sept. 2013), p. 1133–1135. issn : 0741-3106. doi : 10.1109/LED.2013.2271831 (cf. p. 68).

[124] D. Ielmini. « Modeling the Universal Set/Reset Characteristics of Bipolar RRAM by Field- and Temperature-Driven Filament Growth ». In : *IEEE Transactions on Electron Devices* 58.12 (déc. 2011), p. 4309–4317. issn : 0018-9383. doi : 10.1109/TED.2011.2167513 (cf. p. 69, 127).

[125] N. Kyurkchiev et S. Markov. *Sigmoid Functions : some approximation and modeling aspects*. 2015 (cf. p. 70).

[126] Python. *random Generate pseudo-random numbers*. 2018. url : https://docs.python.org/2/library/random.html (visité le 07/04/2018) (cf. p. 70).

[127] M. Matsumoto et T. Nishimura. « Mersenne Twister : A 623-dimensionally Equidistributed Uniform Pseudo-random Number Generator ». In : *ACM Trans. Model. Comput. Simul.* 8.1 (jan. 1998), p. 3–30. issn : 1049-3301. doi : 10.1145/272991.272995. url : http://doi.acm.org/10.1145/272991.272995 (cf. p. 71).

[128] B. Long, Y. Li, S. Mandal et al. « Switching dynamics and charge transport studies of resistive random access memory devices ». In : *Applied Physics Letters* 101.11 (2012), p. 113503. doi : 10.1063/1.4749809. eprint : https://doi.org/10.1063/1.4749809. url : https://doi.org/10.1063/1.4749809 (cf. p. 74, 127).

[129] K.F. Riley, M.P. Hobson et S.J. Bence. *Mathematical Methods for Physics and Engineering : A Comprehensive Guide*. Cambridge University Press, 2006 (cf. p. 75).

[130] W.H. Press, B.P. Flannery, S.A. Teukolsky et al. *Numerical Recipes in C : The Art of Scientific Computing*. New York, NY, USA : Cambridge University Press, 1988. isbn : 0-521-35465-X (cf. p. 77).

[131] X. Lian, X. Cartoixa, E. Miranda et al. « Multi-scale quantum point contact model for filamentary conduction in resistive random access memories devices ». In : 115 (juin 2014), p. 244507–244507 (cf. p. 82, 88, 94).

[132] M. Shirasawa, M. E. Dlamini et Y. Kamakura. « Kinetic Monte Carlo simulation for switching probability of ReRAM ». In : *2016 IEEE International Meeting for Future of Electron Devices, Kansai (IMFEDK)*. Juin 2016, p. 1–1. doi : 10.1109/IMFEDK.2016.7521667 (cf. p. 83).

[133] A. Fantini, D. J. Wouters, R. Degraeve et al. « Intrinsic Switching Behavior in HfO_2 RRAM by Fast Electrical Measurements on Novel 2R Test Structures ». In : *2012 4th IEEE International Memory Workshop*. Mai 2012, p. 1–4. doi : 10.1109/IMW.2012.6213646 (cf. p. 84, 85, 87).

[134] M. Zackriya, H. Kittur et A. Chin. « A Novel Read Scheme for Large Size One Resistor Resistive Random Access Memory Array ». In : *Scientific Reports* 7.42375 (2017) (cf. p. 84).

[135] A. Fantini, D. J. Wouters, R. Degraeve et al. « Intrinsic Switching Behavior in HfO_2 RRAM by Fast Electrical Measurements on Novel 2R Test Structures ». In : *2012 4th IEEE International Memory Workshop*. Mai 2012, p. 1–4. doi : 10.1109/IMW.2012.6213646 (cf. p. 85).

[136] X. Lian, X. Cartoixà, E. Miranda et al. « Multi-scale quantum point contact model for filamentary conduction in resistive random access memories devices ». In : *Journal of Applied Physics* 115.24 (2014), p. 244507. doi : 10.1063/1.4885419. eprint : https://doi.org/10.1063/1.4885419. url : https://doi.org/10.1063/1.4885419 (cf. p. 89, 128).

[137] M. Bocquet, D. Deleruyelle, H. Aziza et al. « Robust Compact Model for Bipolar Oxide-Based Resistive Switching Memories ». In : *IEEE Transactions on Electron Devices* 61.3 (mar. 2014), p. 674–681. issn : 0018-9383. doi : 10.1109/TED.2013.2296793 (cf. p. 89, 127).

[138] D. Ielmini et V. Milo. « Physics based modeling approaches of resistive switching devices for memory and in memory computing applications ». In : *Journal of Computational Electronics* 16.4 (déc. 2017), p. 1121–1143. issn : 1572-8137. doi : 10.1007/s10825-017-1101-9. url : https://doi.org/10.1007/s10825-017-1101-9 (cf. p. 89, 126, 127).

[139] K.H. Hsu, W.W. Ding et M.H. Chiang. « A compact SPICE model for bipolar resistive switching memory ». In : *2013 IEEE International Conference of Electron Devices and Solid-state Circuits*. Juin 2013, p. 1–2. doi : 10.1109/EDSSC.2013.6628127 (cf. p. 89, 127).

[140] T. Tsai, K. Chang, T. Chang et al. « Bipolar Resistive RAM Characteristics Induced by Nickel Incorporated Into Silicon Oxide Dielectrics for IC Applications ». In : *IEEE Electron Device Letters* 33.12 (déc. 2012), p. 1696–1698. issn : 0741-3106. doi : 10.1109/LED.2012.2217933 (cf. p. 95).

[141] C. Lin, C. Wu, C. Wu et al. « Effect of Top Electrode Material on Resistive Switching Properties of ZrO_2 Film Memory Devices ». In : *IEEE Electron Device Letters* 28.5 (mai 2007), p. 366–368. issn : 0741-3106. doi : 10.1109/LED.2007.894652 (cf. p. 95).

[142] R. W. Johnson, A. Hultqvist et S.F. Bent. « A brief review of atomic layer deposition : from fundamentals to applications ». In : *Materials Today* 17.5 (2014), p. 236–246. issn : 1369-7021. doi : https://doi.org/10.1016/j.mattod.2014.04.026. url : http://www.sciencedirect.com/science/article/pii/S1369702114001436 (cf. p. 119, 120).

[143] H. Bae Park, M. Cho, J. Park et al. « Comparison of HfO_2 films grown by atomic layer deposition using $HfCl_4$ and H_2O or O_3 as the oxidant ». In : 94 (sept. 2003), p. 3641–3647 (cf. p. 119).

[144] M. Cho, J. Park, H.B. Park et al. « Chemical interaction between atomic-layer-deposited HfO_2 thin films and the Si substrate ». In : *Applied Physics Letters* 81.2 (2002), p. 334–336. doi : 10.1063/1.1492320. eprint : https://doi.org/10.1063/1.1492320. url : https://doi.org/10.1063/1.1492320 (cf. p. 119).

[145] In : *Handbook of Deposition Technologies for Films and Coatings (Third Edition)*. Sous la dir. de Peter M. Martin. Third Edition. Boston : William Andrew Publishing, 2010, p. ii–. isbn : 978-0-8155-2031-3. doi : https://doi.org/10.1016/B978-0-8155-2031-3.00020-X. url : https://www.sciencedirect.com/science/article/pii/B978081552031300020X (cf. p. 119).

[146] A.S.H. Makhlouf. « Current and advanced coating technologies for industrial applications ». In : *Nanocoatings and Ultra-Thin Films : Technologies and Applications*. Sept. 2011, p. 1–32 (cf. p. 119).

[147] W.D. Westwood. « Sputter Deposition Processes ». In : *MRS Bulletin* 13.12 (1988), p. 46–51. doi : 10.1557/S0883769400063697 (cf. p. 120).

[148] A. Kocak. « Materials science an engineering : Thin Film Preparation,Particle Size and Thickness Analysis Experimental Report ». In : fév. 2018 (cf. p. 120).

[149] K.L. Choy. « Chemical vapour deposition of coatings ». In : *Progress in Materials Science* 48.2 (2003), p. 57–170. issn : 0079-6425. doi : https://doi.org/10.1016/S0079-6425(01)00009-3. url : http://www.sciencedirect.com/science/article/pii/S0079642501000093 (cf. p. 120).

[150] W.M. Moreau. *Semiconductor Lithography : Principles, Practices, and Materials*. Springer Science et Business Media, 2012 (cf. p. 121).

[151] R.C. Jaeger. *Introduction to Microelectronic Fabrication*. Prentice Hall, 2002 (cf. p. 121).

[152] A.P. Nayak, V.J. Logeeswaran et M.S. Islam. « Wet and Dry Etching ». In : *University of California, Davis, California* (2011) (cf. p. 121, 122).

[153] P.V. Zant. *Microchip Fabrication, 5th Ed.* McGraw Hill Professional, 2004 (cf. p. 122).

[154] M. Kulkarni, F. Gao et H. Liang. « Chemical-mechanical polishing (CMP) a controlled tribocorrosion process ». In : *Tribocorrosion of Passive Metals and Coatings*. Woodhead Publishing, 2011. Chap. 18, p. 498–518 (cf. p. 122).

[155] *Chemical-Mechanical Planarization of Semiconductor Materials*. T. 69. Springer series in materials science, 2004 (cf. p. 122).

[156] *Chemical Mechanical Planarization for Microelectronics Applications*. T. 45. Materials Science et Engineering Reports, 2004 (cf. p. 122).

[157] Python. *scipy.stats.normaltest*. 2018. url : https://docs.scipy.org/doc/scipy/reference/generated/scipy.stats.normaltest.html (visité le 07/04/2018) (cf. p. 124).

[158] R.B. D'Agostino. « An Omnibus Test of Normality for Moderate and Large Size Samples ». In : *Biometrika* 58.2 (1971), p. 341–348. issn : 00063444. url : http://www.jstor.org/stable/2334522 (cf. p. 124).

[159] R. D'Agostino et E. S. Pearson. « Tests for departure from normality. Empirical results for the distributions of b_2 and $\sqrt{b_1}$ ». In : *Biometrika* 60.3 (1973), p. 613–622. doi : 10.1093/biomet/60.3.613. eprint : /oup/backfile/content_public/journal/biomet/60/3/10.1093/biomet/60.3.613/2/60-3-613.pdf. url : http://dx.doi.org/10.1093/biomet/60.3.613 (cf. p. 124).

[160] R. Shanmugam et R. Chattamvelli. *Statistics for Scientists and Engineers*. Wiley, 2015 (cf. p. 124).

[161] K. Lejaeghere, G. Bihlmayer, T. Björkman et al. « Reproducibility in density functional theory calculations of solids ». In : *Science* 351.6280 (2016). issn : 0036-8075. doi : 10.1126/science.aad3000. eprint : http://science.sciencemag.org/content/351/6280/aad3000.full.pdf. url : http://science.sciencemag.org/content/351/6280/aad3000 (cf. p. 126).

[162] A. Makarov, V. Sverdlov et S. Selberherr. « Stochastic model of the resistive switching mechanism in bipolar resistive random access memory : Monte Carlo simulations ». In : *Journal of Vacuum Science, Technology B, Nanotechnology and Microelectronics : Materials, Processing, Measurement, and Phenomena* 29.1 (2011), 01AD03. doi : 10.1116/1.3521503. eprint : https://doi.org/10.1116/1.3521503. url : https://doi.org/10.1116/1.3521503 (cf. p. 126).

[163] S. Aldana, P. García-Fernández, A. Rodríguez-Fernández et al. « A 3D kinetic Monte Carlo simulation study of resistive switching processes in Ni/HfO_2/Si - based RRAMs ». In : *Journal of Physics D : Applied Physics* 50.33 (2017), p. 335103. url : http://stacks.iop.org/0022-3727/50/i=33/a=335103 (cf. p. 126).

[164] S. Yu, Y.Yin Chen, X. Guan et al. « A Monte Carlo study of the low resistance state retention of HfO_x based resistive switching memory ». In : 100 (jan. 2012), p. 043507–043507 (cf. p. 126).

[165] M. A. Villena, F. Jiménez-Molinos, J. B. Roldán et al. « An in-depth simulation study of thermal reset transitions in resistive switching memories ». In : *Journal of Applied Physics* 114.14 (2013), p. 144505. doi : 10.1063/1.4824292. eprint : https://doi.org/10.1063/1.4824292. url : https://doi.org/10.1063/1.4824292 (cf. p. 127).

[166] K. Szot, W. Speier, G. Bihlmayer et al. « Switching the electrical resistance of individual dislocations in single-crystalline SrTiO3 ». In : *Nature Materials* 5 (2006). doi : 10.1038/nmat1614 (cf. p. 127).

[167] J. Joshua Yang, Matthew D. Pickett, Xuema Li et al. « Memristive switching mechanism for metal/oxide/metal nanodevices. » In : *Nature nanotechnology* 37 (2008), p. 429–33 (cf. p. 127).

[168] J.H. Hur, M.J. Lee, C.B. Lee et al. « Modeling for bipolar resistive memory switching in transition-metal oxides ». In : *Phys. Rev. B* 82 (15 oct. 2010), p. 155321. doi : 10.1103/PhysRevB.82.155321. url : https://link.aps.org/doi/10.1103/PhysRevB.82.155321 (cf. p. 127).

[169] J. Borghetti, D. B. Strukov, M.D. Pickett et al. « Electrical transport and thermometry of electroformed titanium dioxide memristive switches ». In : *Journal of Applied Physics* 106.12 (2009), p. 124504. doi : 10.1063/1.3264621. eprint : https://doi.org/10.1063/1.3264621. url : https://doi.org/10.1063/1.3264621 (cf. p. 127).

[170] J.G. Simmons. « Electric Tunnel Effect between Dissimilar Electrodes Separated by a Thin Insulating Film ». In : *Journal of Applied Physics* 34.9 (1963), p. 2581–2590. DOI : 10.1063/1.1729774. eprint : https://doi.org/10.1063/1.1729774. URL : https://doi.org/10.1063/1.1729774 (cf. p. 127).

[171] M.D. Pickett, D.B. Strukov, J.L. Borghetti et al. « Switching dynamics in titanium dioxide memristive devices ». In : *Journal of Applied Physics* 106.7 (2009), p. 074508. DOI : 10.1063/1.3236506. eprint : https://doi.org/10.1063/1.3236506. URL : https://doi.org/10.1063/1.3236506 (cf. p. 127).

[172] E. Miranda et J. Suñé. « Analytic modeling of leakage current through multiple breakdown paths in SiO_2 films ». In : *2001 IEEE International Reliability Physics Symposium Proceedings 39th Annual, Cat. No.00CH37167*. 2001, p. 367–379. DOI : 10.1109/RELPHY.2001.922929 (cf. p. 128).

[173] S. Datta. « Preliminary concepts ». In : *Electronic Transport in Mesoscopic Systems*. Cambridge Studies in Semiconductor Physics and Microelectronic Engineering. Cambridge University Press, 1995. DOI : 10.1017/CBO9780511805776.002 (cf. p. 128).

[174] A. M. Song. « Formalism of nonlinear transport in mesoscopic conductors ». In : *Phys. Rev. B* 59 (15 avr. 1999), p. 9806–9809. DOI : 10.1103/PhysRevB.59.9806. URL : https://link.aps.org/doi/10.1103/PhysRevB.59.9806 (cf. p. 129).

[175] S. Long, X. Lian, C. Cagli et al. « Quantum-size effects in hafnium-oxide resistive switching ». In : *Applied Physics Letters* 102.18 (2013), p. 183505. DOI : 10.1063/1.4802265. eprint : https://doi.org/10.1063/1.4802265. URL : https://doi.org/10.1063/1.4802265 (cf. p. 130).

[176] Y.E. Syu, T.C. Chang, J.H. Lou et al. « Atomic-level quantized reaction of HfO_x memristor ». In : *Applied Physics Letters* 102.17 (2013), p. 172903. DOI : 10.1063/1.4802821. eprint : https://doi.org/10.1063/1.4802821. URL : https://doi.org/10.1063/1.4802821 (cf. p. 130).

Index

Activation step : electroforming process, 31
Analysis of the conduction mechanism, 54

Bipolar switching, 33
Bulk-type conduction mechanism, 36

Conduction mechanism of ReRAM, 34
Conduction mechanisms in the model, 74

Device fabrication, 39
Device structure, 40
Different electrical response of the samples electroformed with I_c=5mA and I_c=10mA, 64

Electrical characterization, 41
Electrical characterization of HfO_2-based ReRAM, 46
Electroforming : cell activation, 42

From resistive change materials to ReRAM, 30

Interface-type conduction mechanism, 34
Intrinsic IV switching characteristics, 85
Intrinsic resistive switching parameters, 87

Model calibration, 79
Model for the resistive switching of 1T1R ReRAM cell structure, 89
Model implementation, 75

N-Chain model, 73
Nonpolar switching, 34
Number of conduction channels in LRS, 88

Ohmic conduction, 55
One-Chain model, 69
Overview of memory technologies, 26

Preliminary studies of HfO_2-based ReRAM, 37

ReRAM operation, 31

Set and reset switching simulation, 71
Set and reset voltage study, 47
Simulation results and discussion, 81
Stochastic Nature of ReRAM, 66
Switching modes, 32
Switching probability, 70

Trap assisted tunneling conduction (TAT), 57

Unipolar switching, 32

Notes

ANNEXES

A. Articles

L. Trojman, S. Guitarra, L. M. Procel et al. « Study of the scaling and the temperature for RERAM cells using the QPC model ». In : *IEEE Latin America Transactions* 14.12 (déc. 2016), p. 4693–4698. ISSN : 1548-0992. DOI : 10.1109/TLA.2016.7816999

B. Fabrication techniques used in HfO_2-based ReRAM's

As it was mentioned in section 2.1 some technique have been used to ReRAM fabrication. Due to the importance of the process fabrication on the ReRAM behavior, in this appendix, we will analyze the characteristics of each one.

B.1. Atomic layer deposition (ALD)

This technique was used to deposite the switching layer (HfO_2) of the studied ReRAM devices. ALD is a vapor phase technique to produce thin films, based on sequential self-limiting chemisorption or gas-solid reactions between the precursor and surface [142]. It allows fabrication of high quality thin films that have good uniformity, good conformality, atomic scale thickness control and excellent surface coating regardless the physical geometry.

The commonly used precursor and counter-reactant for ALD of HfO_2 films are the $HfCl_4$ and H_2O, respectively. This is because of the existence of a proper ligand exchange reaction between the two materials at a relatively low temperature (200 - 400 °) without thermal decomposition of the precursors [143].

An ALD process is illustrated in Fig .1. First, the precursor ($HfCl_4$) is pulse into a chamber under vacuum with enough time to allow a full reaction with the substrate. After, the chamber is purged with an inert gas (N_2 of Ar) to remove any unreacted precursor. Then, the counter-reactant (H_2O) is applied and it reacts with precursor. After, the excess of precursor and unreacted molecules of precursors and other sub-products of the process are cleared with a second purge. At this point, one layer of the material is created. This cycle is repeated until achieving the desired film thickness [142].

It has been reported that HfO_2 films remain amorphous when the layer thickness is less than or equal to 5 nm, irrespective of the deposition technique [144].

B.2. Physical vapor deposition (PVD)

This technique has been used to deposite TiN electrodes and Hf capping layer. In the physical vapor deposition (PVD) process, the coating is deposited in vacuum by condensation from a flux of neutral or ionized atoms of metals [99, 145]. In this process, the material goes from a condensed phase to a vapor phase and then back to a thin film condensed phase.

The process begins with evaporation of the material from a solid source by a high energy source. After, the vapor is transported in vacuum towards the substrate. Finally, the condensation onto the substrate generates the coating [146]. The two most common PVD processes are thermal evaporation and sputtering.

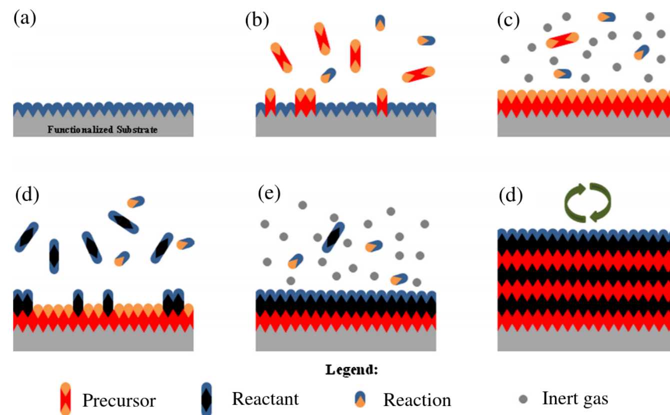

FIGURE .1. – Schematic of the Atomic Layer Deposition (ALD) process. (a) Substrate surface is prepared (b) Precursor A is pulse and reacts with surface (c) Excess precursors and reactions are purged with inert gas (d) Counter-reactant (H_2O) precursor is applied and reacts with surface (e) Second purge (f) The process is repeated until the desired material thickness is achieved [142]

In thermal evaporation, the vaporization of the source material is by heating the material using appropriate methods in vacuum. Meanwhile, in sputtering, a plasma-assisted technique creates a vapor from the source target through bombardment with accelerated gaseous ions (typically Argon) [147].

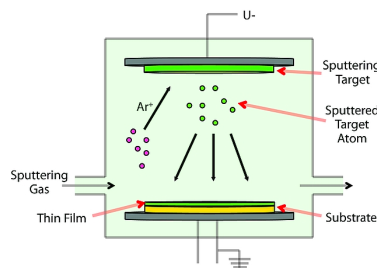

FIGURE .2. – Schematic of the Physical Vapor Deposition (PVD) process[148]

With this technique, the films have high purity and an excellent bonding to the substrate.

B.3. Chemical vapor deposition (CVD)

The SiO_2 hardmask has been deposited by CVD. This thecnique involve the chemical reactions of gaseous reactants on or near the vicinity of a heated substrate surface [149]. CVD is the main processing methods for the deposition of thin films and coatings for has many applications, including semiconductors (Ge, Si) and dielectrics (SiO_2, AlN, Si_3N_4) for microelectronics.

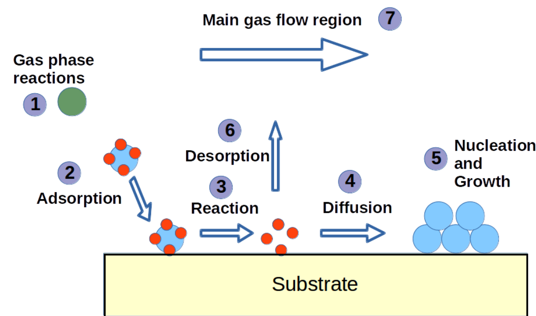

FIGURE .3. – Schematic of the Chemical Vapor Deposition (CVD)

The steps for CVD process are presented in figure .3. The process begins with the evaporation and transport of reagents into the reactor where gas phase reactions occur to produce film precursors (1). Thus, they are transported to the substrate surface where it absorbes (2) and reacts (3) to liberate the ligands and reaction by-products. Then, the metal atoms diffuse to form a stable nucleii (4) and, subsequent nucleation and growth occurs (5). The ligands and by-products are desorbed (6) and transported out of the reactor (7).

B.4. Lithography and dry etch

Lithography and dry etch follow the SiO_2 deposition, as it is shown in figure .4 . Lithography and etching are two steps in the manufacturing of silicon-based semiconductors to create the patterns of the integrated circuit [150, 151].

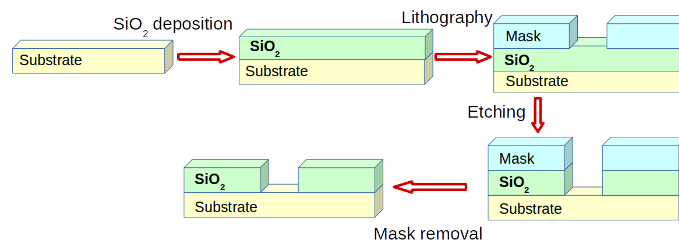

FIGURE .4. – Schematic of lithography and etch

Lithography is the process of drawing a pattern over a previous layer to select specific areas on the wafer and protect them with a resist material that acts as a mask. After, the material without the mask is removed from a substrate surface by etching. This process can be devided into two major types : wet etching, which involves liquid chemicals, and dry etching, which involves plasmas or etchant gases. During ReRAM fabrication dry etching has been used. This method requires high energy kinetic beams of particles that knock out the atoms from the substrate surface [152], as it is shown in figure .5.

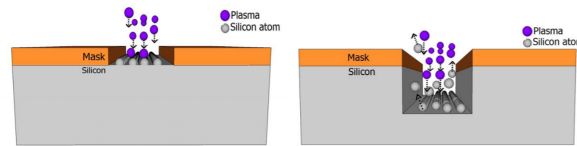

FIGURE .5. – The plasma hits the silicon wafer with high energy to knock-off the Si atoms on the surface. (a) The plasma atoms hitting the surface (b) The silicon atoms being evaporated off from the surface [152]

For SiO_2, the typical plasma etching chemicals is fluorine and the typical gas compounds are CF_4, CHF_3, C_2F_6 and C_3F_8 [153].

B.5. Chemical mechanical planarization (CMP)

The chemical mechanical planarization (CMP) is a process of smoothing and planarization at miniaturized device dimensions, with the combination of chemical reactions and mechanical forces [154].

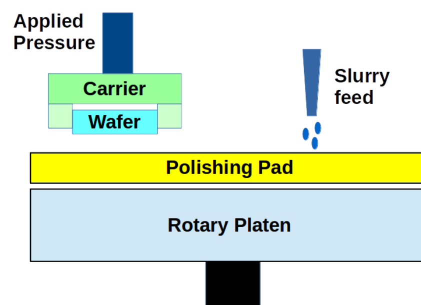

FIGURE .6. – A schematic of CMP process [155]

A diagramm of the process is presented in figure .6. The wafer is mounted horizontally aligned. The carrier provide constant pressure and control it by force sensors. The wafer is pressed against the polishing pad that is sticked to a driver motor capable of providing a constant speed during polishing. During te process, a mixture of abrasive particles and chemical additives (slurry) flows on the center of the pad and it is uniformly distributed on the entire pad surface [155].

The chemical part of the process is the reaction between chemical reagents in slurry and wafer that results in modification of wafer surface. At the same time, the mechanical action is describe by the controlled speed and pressure [156]. CMP technique is important to remove excess material or prepare the material for next processing steps.

B.6. Passivation process

The manufacturing process finish with the passivation process, where Si_3N_4 and SiO_2 are deposited by CVD (see B.3) over the cell to protect it from external agents. This step improves device performance by reducing dark current density and it makes the cells temperature resistance.

C. Normality test for electrical parameters

All the electrical parameters analyzed in chapter 2.5.1 show a wide distribution of values during cycles. In this way, histograms have been plotted to represent the behavior of data. They allow us to identify the most suitable distribution function, as well as the mean value and the dispersion of data.
In this annexe, a normality test has been applied to prove the null hypothesis :

Null hypothesis : *Data comes from a normal distribution.*

A significance level (α) of 1% has been considered in this work. Thus, if p-value $\leq \alpha$, the null hypothesis can be rejected. k and p-value are obtained by using the python function *scipy.stats.normaltest* [157], where k is the test statistics and p-value is defined as a 2-sided chi squared probability for the hypothesis. This test is based on D'Agostino and Pearson's test [158, 159] that combines skewness and kurtosis.
The values of kurtosis and skewness have also been computed. The skewness is a way to measure the lack of symmetry, while the kurtosis is a way to measure wheter the data are heavy-tailed relative to a normal distribution [160].
For each electrical parameter mean-value, standard deviation, skewness, kurtosis, p-value, and the result of the normality test have been included in table. While, in histograms we present the distribution of data with the normal function, is the test is true.

1. Set voltage : V_{set}

Sample	Mean	Std. Dev.	Kurtosis	Skew	p-value	Normal distributed
55nm	0.594	0.082	-0.630	0.111	0.601	True
65nm	0.632	0.082	0.056	-0.043	0.868	True
75nm	0.681	0.133	0.244	0.496	0.105	True
85nm	0.732	0.105	0.559	0.103	0.392	True
105nm	0.706	0.076	0.710	-0.151	0.264	True
135nm	0.697	0.100	-0.104	-0.035	0.986	True
1um	0.473	0.091	0.760	-0.872	0.015	False
3um	0.490	0.073	0.658	-0.099	0.406	True
5um	0.479	0.067	0.570	-0.297	0.310	True

TABLE .1. – Normality test results for V_{set} [V]

2. Reset voltage : V_{reset}

Sample	Mean	Std. Dev.	Kurtosis	Skew	p-value	Normal distributed
55nm	-1.266	0.083	-0.099	-0.463	0.342	True
65nm	-1.251	0.078	-0.365	0.158	0.848	True
75nm	-1.206	0.131	0.983	-0.171	0.007	False
85nm	-1.012	0.097	0.563	-0.464	0.077	True
105nm	-0.962	0.086	0.787	-0.816	0.003	False
135nm	-1.007	0.104	0.024	-0.751	0.004	False
1um	-1.235	0.069	1.778	-1.575	0.000	False
3um	-1.217	0.071	2.990	-1.637	0.000	False
5um	-1.203	0.058	1.833	-0.970	0.002	False

TABLE .2. – Normality test results for V_{reset} [V]

3. I_o in TAT conduction

Sample	Mean	Std. Dev.	Kurtosis	Skew	p-value	Normal distributed
55nm	15.297	6.759	0.865	0.947	0.008	False
65nm	12.319	4.820	1.023	1.081	0.003	False
75nm	7.950	4.407	-0.280	0.775	0.047	True
85nm	2.758	1.181	1.255	0.867	0.001	False
105nm	3.356	1.292	-0.249	0.551	0.118	True
135nm	3.013	1.351	0.084	0.717	0.030	True
1um	131.167	57.838	-0.417	-0.054	0.912	True
3um	132.996	64.364	-0.556	0.125	0.702	True
5um	146.242	62.982	-0.710	-0.257	0.354	True

TABLE .3. – Normality test results for I_o [A]

4. α in TAT conduction

Sample	Mean	Std. Dev.	Kurtosis	Skew	p-value	Normal distributed
55nm	1.559	0.188	-0.329	0.263	0.691	True
65nm	1.638	0.171	1.047	-0.794	0.015	True
75nm	1.774	0.221	1.682	0.864	0.002	False
85nm	2.031	0.188	-0.618	0.195	0.264	True
105nm	1.967	0.145	-0.381	0.192	0.648	True
135nm	2.004	0.181	1.001	0.644	0.012	True
1um	1.470	0.174	2.743	1.345	0.000	False
3um	1.511	0.213	3.459	1.720	0.000	False
5um	1.494	0.194	0.217	1.003	0.013	True

TABLE .4. – Normality test results for α [1/V]

D. Models for resistive switching in ReRAM devices

The objective of this appendix is providing a general review of the models proposed in the literature for the switching behavior of ReRAM devices. They are mainly studied in three different levels : microscopic models, macroscopic models and compact models.

Microscopic models usually start with a quantum mechanical description of dielectric to reproduce the atomic and molecular interactions inside the material [64]. Density functional theory (DFT), molecular dynamics (MD) and Monte Carlo (MC) are common techniques used to study ReRAM devices [47, 161–163]. These models keep track of each cation or anion, and calculate their migration trajectory taking into consideration the sourrounding environment : other particles, electric field, magnetic field, temperature, etc. For this, it includes the solution of Poisson and heat equations [118]. As a result, one can obtain a very detailed physical description and also a good analysis of the the variability of ReRAM response. Unfortunately, the computational cost of these methods is high and long timescales are required. For these reasons, these methods are umpractical if the number of devices is large. Some examples of this kind of models in the HfO_2-based memories are presented in table .5 :

MIM structure	Switching mode	Method	Reference
$TiN/Hf/HfO_x/TiN$	Bipolar	Monte Carlo	Yu et al. [164]
$TiN/HfO_2/Pt$	Bipolar	Monte Carlo	Yu et al. [47]
$Cu/HfO_2/Pt$	Bipolar	Monte Carlo	Pengxiao et al [93]

TABLE .5. – Published works with Monte Carlo simulation in HfO_2-based ReRAM

On the other hand, macroscopic models solve differential equations to reproduce the characteristics of ReRAM [118]. They represent the transport of charge carriers (electron, holes), heat, and ionized defect (oxygen vacancies, cations) with differential equations while consider the electric field, temperature and defect concentration with a continuous description [138]. Several numerical techniques, such as finite element method (FEM) or Runge-Kutta method, have been applied to solve the equations. These methods calculate the I-V response and also reproduce electrical variability and noise. The computational cost in this case is medium to low. However, they are not adequate for studying the microscopic processes. Table .6 presents some macroscopic models reported for the study of HfO_2-based ReRAM.

The third level of simulations is compact modeling approximation. These models calculate electrical behavior by solving equations that describe global characteristics of the device, such as filament diameter, average temperature, voltage,

MIM structure	Switching mode	HRS conduction	Reference
TiN/HfO_x/TiN	Bipolar	-	Bersuket et al. [71]
Au/HfO_2/TiN	Unipolar	QPC	Miranda et al. [48]
IM/HfO_2/IM	Bipolar	Poole-Frenkel	Ielmini et al [124]
TiN/HfO_2/Ti/TiN	Bipolar	Poole-Frenquel	Walczyk et al [4]
Ru/HfO_2/TiO_x/Ru	Bipolar	Poole-Frenkel	Long et al [128]
TiN/HfO_2/Hf/TiN	Bipolar	QPC	Procel et al [84]
Cu/HfO_2/Pt	Bipolar	Poole-Frenkel	Villena et al [165]

TABLE .6. – Macroscopic models for simulation in HfO_2-based ReRAM

among others [138]. Usually, compact models describe the device operation in the context of circuit simulators [118], therefore, they could be an essential tool for industrial applications. Simulations based on compact models uses a lot of approximation, thus they are simple and have low computational cost. Table .7 presents some compact models reported in the literature for the study of HfO_2-based ReRAM.

MIM structure	Switching mode	Reference
TiN/HfO_2/TiN	Bipolar	Larcher et al. [52]
TiN/TiO_x/HfO_x/TiN	Bipolar	Hsu et al. [139]
TiN/HfO_2/Ti	Bipolar	Bocquet et al [137]

TABLE .7. – Compact models simulation in HfO_2-based ReRAM

In this thesis, an equivalent circuit modeling of the conductive filament CF is used to reproduce the switching behavior of HfO_2-based ReRAM. Some works related to the circuit representation are : the local reduction-oxidation model [166], the memristor-rectifier model [167], the Schottky barrier model [168], the tunneling barrier model [169–171], the random circuit breaker (RCB) models for unipolar [63] and bipolar devices [83], among others.

D.1. Quantum Point-Contact model

The quantum point contact (QPC) model was originally developed to explain the soft and hard breakdown of ultra-thin SiO_2 films used as gate insulators in MOS devices [172]. The quantum point response is observed when the size of the conductive filament is thin enough to evidence its atomic size. As pointed out by Datta [173], this occurs if the dimensions of the conductor are smaller than one of these three characteristics lenghts : (1) de-Broglie wavelength of electrons, (2) the mean free path of electrons and (3) the phase-relaxation length. If this occurs, ballistic transport can be realized.

The de Broglie wavelength is related to the kinetic energy of an electron and it is the length scale on which quantum-mechanical effects are important. The mean free path is the average distance that an electron travels before it experiences elastic scattering wich destroys its initial momentum. The phase-relaxation lenght is the average distance that an electron travels before it experiences inelastic scattering due to events like electron-phonon or electron-electron collisions [173].

Nowadays, the QPC theory has also been applied to describe the conduction of high and low resistance states in ReRAM [48, 136]. The model considers the thinnest part of the CF as a quantum point contact (see Fig. .7) and the difference between the two states, HRS or LRS, is attributed to the change of the potential barrier because of the size modulation of this region of the filament.

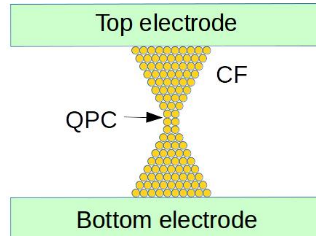

FIGURE .7. – The schematic of the ReRAM cell with a narrow zone inside the conductive filament (CF) considered as a quantum point contact (QPC).

The QPC model assumes that the conduction takes place through a CF which is narrow enough to quantize the energy in two directions perpendicular to the electron transport, thus behaving as a quasi-1D system [97]. The dispersion relation of the electronic subbands could be expressed as :

$$E(k_z, z) = \epsilon_n(z) + \frac{\hbar^2 k_z^2}{2m} \quad (.1)$$

where z and k_z are the coordinates in the longitudinal direction in real-space and k-space, respectively, m is the mass of the electron and $\hbar$ is the reduced Planck

constant [114]. $\epsilon_n(z)$ is the energy associated with the lateral confinement of the subband. If the confinement is in a rectangle shape, then

$$\epsilon_n(z) = \frac{\pi^2\hbar^2}{2m}\left(\frac{n_x^2}{L_x(z)^2} + \frac{n_y^2}{L_y(z)^2}\right) \tag{.2}$$

where $L_x(z)$ and $L_y(z)$ are the dimensions of the constriction and n_x and n_y are integers. This means that the relation between E and k_z (dispersion curve) is formed by discrete parabolic subbands in each z, as shown in figure .8. The number of subbands is just the number of conducting channels N. Φ is the height of the first subband and t_B is the barrier width of the first subband at $E = 0$.

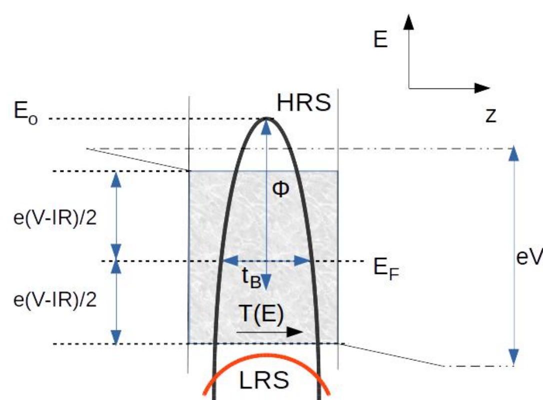

FIGURE .8. – Schematic representation of the energy barrier profile along the constriction where V is the applied external voltage, I is the filament current, R is an external series resistance, E_F is the Fermi level, Φ is the potential height in relation to Fermi level, t_B is the potential thickness at E_F and e is the elementary electron charge. For the HRS, the potential barrier is above the energy window and for LRS, is below. The shaded region is the energy window for the injected electrons [48].

For conduction, the Landauer-Buttiker formalism treats transport as a transmission problem for electrons at the Fermi level [174]. It means that electrons will travel through the potential barrier with a transmission probability T(E). By assuming the Landauer theory in the zero-temperature limit for a parabolic potential barrier, the current in the CF is given by eq. [48] :

$$I = \frac{2e}{h}\int T(E)dE \tag{.3}$$

$$I = \frac{2e}{h}\int_{-e(V-IR)/2}^{e(V-IR)/2} \{1 + \exp[-\alpha(E - \Phi)]\}^{-1}\, dE \tag{.4}$$

where E is the energy of the electrons, R is the series resistance external to the constriction and e is the electron charge. The constant α in equation .4 is a shape parameter related to t_B according to the expression [97] :

$$\alpha = t_B \pi^2 h^{-1} \sqrt{\frac{2m*}{\Phi}} \tag{.5}$$

where m^* is the electron effective mass in the constriction. By integrating .4, an implicit equation for the filament current is obtained :

$$I = \frac{2e}{h} \left\{ e(V - IR) + \frac{1}{\alpha} \ln \left[\frac{1 + \exp\{\alpha[\Phi - e(V - IR)/2]\}}{1 + \exp\{\alpha[\Phi + e(V - IR)/2]\}} \right] \right\} \tag{.6}$$

In ReRAM systems, there are two well-separated conduction modes : HRS and LRS. For HRS, it is assumed that the top of the barrier is above the energy window of the injected electrons (see Fig. .6). This corresponds to tunneling conduction with IR $\ll$ V and equation .6 is reduced to :

$$I_{HRS} \approx \frac{2e}{h} \left\{ eV + \frac{1}{\alpha} ln \left[\frac{1 + exp \alpha[\Phi - eV/2]}{1 + exp \alpha[\Phi + eV/2]} \right] \right\} \tag{.7}$$

In LRS, the top of the barrier is below the energy window of the injected electrons so the potential barrier plays no role (see Fig. .6) and $T(E) \approx 1$. In this case, the current has a linear relationship.

$$I_{LRS} \approx \frac{G_o}{1 + G_0 R} V \tag{.8}$$

where G_o is the quantum conductance unit and is equal to $G_o = \frac{2e^2}{h}$.

This kind of conduction has been applied by some autors [48, 84, 98] to study conduction in HfO_2-based ReRAM. Long et al [175], report that the Pt/HfO_2/Pt unipolar system in HRS has a quantization level of 0.5G_0. Another example is reported by Syu et al [176] in the Ti/HfO_2/TiN bipolar cell with a quantization level of G_0.